Durham E-Theses

Halo Substructure and the Nature of Dark Matter

MARK RICHARD LOVELL

How to cite:

LOVELL, MARK RICHARD (2013) Halo Substructure and the Nature of Dark Matter. Doctoral thesis, Durham University.

Use policy

The full-text may be used and/or reproduced, and given to third parties in any format or medium, without prior permission or charge, for personal research or study, educational, or not-for-profit purposes provided that:

- a full bibliographic reference is made to the original source
- a https://etheses.durham.ac.uk/id/eprint/8461/ is made to the metadata record in Durham E-Theses
- the full-text is not changed in any way

The full-text must not be sold in any format or medium without the formal permission of the copyright holders.

Please consult the full Durham E-Theses policy for further details.

Academic Support Office, The Palatine Centre, Durham University, Stockton Road, Durham, DH1 3LE
e-mail: e-theses.admin@durham.ac.uk Tel: +44 0191 334 6107
https://etheses.durham.ac.uk

Halo Substructure and the Nature of Dark Matter

Mark R. Lovell

Abstract

The ΛCDM paradigm has been very successful at predicting the properties of the large scale (> 10Mpc) Universe, but has recently struggled to explain phenomena observed on small scales, such as the central densities, abundances, and orbital configurations of satellite galaxies. This emergence of tension between observations and theory has coincided with CERN measurements that disfavour the simplest supersymmetric models, which provide some of the most popular cold dark matter candidate particles. One possible solution to some of these problems is that the dark matter may instead be made up of sterile neutrinos: these particles would have masses of 1-10keV and behave as 'warm' dark matter (WDM), with consequences for the formation of galaxies. In this thesis we use high resolution simulations of Milky Way-analogue dark matter haloes to examine the role of filaments on satellite orbits and WDM on satellite abundance and structure. We find in the former case that dark matter filaments can funnel subhaloes into correlated orbits and so ease the tension with observations. We also find that WDM is a possible solution to the problem of satellite galaxy densities, since structure formation is delayed in WDM and thus the centres of haloes form when the density of the Universe is lower. In order to generate the required number of satellite galaxies, we find that the WDM thermal-equivalent particle mass $> 1.6\mathrm{keV}$. In addition to the work on satellite galaxies, we use a series of gas-hydrodynamic simulations of our Milky Way-analogue halo to examine the process of reionisation in WDM. We find that the suppression of small scale structure in the 1.4keV WDM model prevents the simulated L_* galaxy, along with its satellites, from reionising its own local volume quickly enough to satisfy the reionisation redshift constraint set by the recent Planck satellite results, in contrast to CDM.

Halo Substructure and the Nature of Dark Matter

The interface between galaxy formation and dark matter physics

by Mark Richard Lovell

A thesis submitted to the University of Durham
in accordance with the regulations for
admittance to the Degree of Doctor of Philosophy.

Institute for Computational Cosmology
Department of Physics
University of Durham
August 2013

Contents

1 Introduction 1

1.1 Dark Matter, Zwicky and all that 1

1.2 The ΛCDM Model 2

1.3 What's the matter? 3

1.4 Constraining WDM with observations of the early Universe and X-ray decays 6

1.5 The Local Group 7

1.6 Structure of this Thesis 8

2 Orbits of satellite galaxies 9

2.1 Introduction 9

2.2 The simulations 11

2.3 Results 14

2.3.1 Angular momentum distributions of subhaloes 14

2.3.2 The origin of coherent rotation 21

2.4 Conclusions 25

3 Addressing the 'Too Big to Fail' problem with WDM 27

3.1 Introduction 27

3.2 The simulations 30

3.3 Results 36

3.4 Discussion and conclusions 41

4 The properties of warm dark matter haloes 45

4.1 Introduction 45

4.2 The simulations 49
4.2.1 Simulation parameters 49
4.2.2 The structure of the main haloes 54
4.3 Removal of Spurious Haloes 55
4.3.1 Outline of the methods 57
4.3.2 Application 59
4.4 Results 67
4.4.1 The subhalo mass and $V_{\max}$ functions 67
4.4.2 The radial distribution of subhaloes 70
4.4.3 The internal structure of WDM subhaloes 73
4.4.4 The abundance of the most massive subhaloes 81
4.5 Discussion and conclusions 82

5 The epoch of reionisation in warm dark matter 89
5.1 Introduction 89
5.2 The simulations 90
5.3 Results 94
5.4 Discussion and conclusions 97

6 Conclusions 99
6.1 Satellite orbits 99
6.1.1 Future prospects 99
6.2 Satellite galaxy structure and abundance in warm dark matter 100
6.2.1 Future prospects 100
6.3 Reionisation 101
6.3.1 Future prospects 101

A $V_{\max}$ Convergence Study 103
A.1 Convergence study 103

List of Figures

2.1 The distribution of cos $\theta_{\mathrm{H\cdot S}}$ for the six Aquarius haloes at resolution level L2, where $\theta_{\mathrm{H\cdot S}}$ is the angle between the main halo spin and subhalo orbit vectors. The six are separated into two panels according to whether or not they exhibit an antiparallel tail greater than 0.5. *Top panel:* results for Aq-A2 (orange), Aq-D2 (green), and Aq-E2 (light blue). *Bottom panel:* as above, but for Aq-B2 (blue), Aq-C2 (red), and Aq-F2 (purple). In both cases, the dashed line corresponds to an isotropic distribution. 13

2.2 The distribution of cos $\theta_{\mathrm{H\cdot S}}$ for all the resolution levels of Aq-A. Aq-A1 contains 197484 subhaloes (purple), Aq-A2 30177 (orange), Aq-A3 9489 (red), Aq-A4 1411 (green), and Aq-A5 246 (light blue). The error bars denote Poisson uncertainties. 15

2.3 The distribution of cos $\theta_{\mathrm{H\cdot S}}$ for different populations. *Top panel:* comparison of the 1000 most massive subhaloes at $z = 0$ (purple) with the 100 subhaloes that have the most massive progenitors (light blue), and the entire population of Fig. 2.2 (orange). *Bottom panel:* comparison of the cos $\theta_{\mathrm{H\cdot S}}$ distribution for subhaloes with two populations of main halo particles: a sample of 3×10^4 selected to have the same radial distribution as the main halo (blue) and the full population (red). 16

2.4 Mollweide projections of the directions of the angular momentum vectors of all subhaloes in the L2 simulations. The red circle shows the direction of the main halo spin, blue the main halo spin antipole, and green the densest collection of vectors after smoothing. The maps have been rotated such that all three circles lie on the equator, with the main halo spin and its antipole lying 90° either side of the centre and the green circle in between. Thus, a subhalo of $\theta_{\mathrm{H\cdot S}}= 0^{\circ}$ will map to the red circle, and one of $\theta_{\mathrm{H\cdot S}}= 90^{\circ}$ to either the plot boundary or a point on the north-south bisector. 19

2.5 Mollweide projections of the directions of the angular momentum vectors of subhaloes with the largest progenitors in the L2 simulations. Subhaloes with top 100 progenitors are denoted in blue; the subset with the 11 largest progenitors are plotted in purple. 20

2.6 $X - Y$ positions for subhaloes associated with the largest FOF group at $z = 0$ in two projections. Subhaloes with cos $\theta_{\mathrm{H\cdot S}}> 0.9$ are indicated in red and those with cos $\theta_{\mathrm{H\cdot S}}< -0.9$ in blue. All other subhaloes are shown in black. The black circle marks the virial radius, r_{200}. *Left panels (i.e. L):* the X axis points in the direction of the main halo spin, so those subhaloes with orbit vectors parallel and antiparallel to the main halo spin appear as a band parallel to the Y axis. *Right Panel (R):* looking down the X axis, so the main halo is spinning anticlockwise. The red and blue points are plotted in a random order on top of the black. 22

2.7 $X - Y$ comoving positions at $z = 127$ of the centre of mass of the particles that end up in each subhalo at $z = 0$. The coordinates are as in Fig. 2.6, with the main halo spin at $z = 0$ still determining the projections. The final virial radius is indicated in yellow. As stated in the text, the haloes Aq-A2 and Aq-D2 are found to accrete their 'red' and 'blue' subhaloes in the plane of the main halo spin, and so we have added coloured arrows to the A-R and D-R panels to illustrate schematically the accretion paths for the different subhalo populations. The 'blue' subhaloes of Aq-E2 exhibit similar behaviour, and so we have also included arrows to indicate their motion in E-R. 23

2.8 Mollweide projections of the position at which each subhalo enters the main halo. Subhaloes that end up in parallel spin orbits are shown in red, those that end up in antiparallel spin orbits in blue, and those with intermediate orbits in black. The main halo spin points towards the north pole of each projection. 24

3.1 The solid lines show the linear power spectra (from CMBFAST; Seljak and Zaldarriaga, 1996) used for the two simulations. Black is the original, CDM Aq-A spectrum, and red is that of Aq-AW. The vertical dashed line marks the peak of the WDM spectrum peak. The arrow marks the Nyquist frequency of the level 2 simulations. The dashed red curve corresponds to the M2L25 model of (Boyarsky et al., 2009b) which is almost identical to the solid red curve for scales below $k \sim 10$ h/Mpc. 33

3.2 The free streaming comoving distance traveled per log interval of $1 + z$, where z is redshift, for a warm dark matter particle with a fiducial velocity of $24\ \mathrm{m\,s^{-1}}$ at the present day. The dashed vertical line marks the redshift of matter-radiation equality. The dotted vertical line indicates the start redshift of the WDM simulations. 34

3.3 Images of the CDM (left) and WDM (right) level 2 haloes at $z = 0$. Intensity indicates density, and hue velocity dispersion, ranging from blue (low velocity dispersion) to yellow (high velocity dispersion). Each box is 1.5 Mpc on a side. Note the sharp caustics visible at large radii in the WDM image, several of which are also present, although less well defined, in the CDM case. 35

3.4 The correlation between subhalo maximum circular velocity and the radius at which this maximum occurs. Subhaloes lying within 300kpc of the main halo centre are included. The 12 CDM and WDM subhaloes with the most massive progenitors are shown as blue and red filled circles respectively; the remaining subhaloes are shown as empty circles. The shaded area represents the 2σ confidence region for possible hosts of the 9 bright Milky Way dwarf spheroidals determined by Boylan-Kolchin et al. (2011). 37

3.5 Circular velocity curves for the 12 CDM (left) and WDM (right) subhaloes that had the most massive progenitors. The 3 red curves represent subhaloes with the most massive progenitors, which could correspond to those currently hosting counterparts of the Large and Small Magellanic Clouds and the Sagittarius dwarf. The 9 black curves might more fairly be compared with the data for the 9 bright dwarf spheroidal galaxies of the Milky Way considered by Wolf et al. (2010). Deprojected half-light radii and their corresponding half-light masses, as determined by Wolf et al. (2010) from line-of-sight velocity measurements, are used to derive the half-light circular velocities of each dwarf spheroidal. These velocities and radii are shown as coloured points. The legend indicates the colour coding of the different galaxies. 38

3.6 The correlation between subhalo central mass at infall and the redshift of formation, $z_{\rm form}$, defined as the redshift at which the total mass of each proto subhalo first exceeded this value. Central mass is defined within 1 kpc, and CDM and WDM results are shown with blue and red symbols respectively. 40

3.7 The variation with subhalo mass at infall of the ratio of the present day mass to the infall mass contained within 500pc, 1kpc and 2kpc. Data are shown for the 12 subhaloes identified at $z = 0$ which had the most massive progenitors, with CDM in blue and WDM in red. The symbol type denotes the radius interior to which the central mass is being measured and large symbols show the medians of the corresponding distributions. We find no systematic differences between the CDM and WDM subhalo mass ratios. . 41

4.1 The linear theory power spectrum used in the simulations. The black line corresponds to the CDM model, CDM-W7, while the blue, green, orange and red lines correspond to the $m_{2.3}$, $m_{2.0}$, $m_{1.6}$, and $m_{1.4}$ WDM models respectively. The arrows mark, in order of smallest to largest, the Nyquist frequency of our low, medium, and high resolution simulations. 52

4.2 Images of our haloes at redshift $z = 0$. The panels show CDM-W7 (top), $m_{2.3}$, $m_{2.0}$, $m_{1.6}$, and $m_{1.4}$ (left to right, then top to bottom). Image intensity indicates projected squared dark matter density and hue density-weighted mean velocity dispersion (Springel et al., 2008a). Each panel is 1.5Mpc on a side. 53

4.3 Density profiles of the main haloes (including subhaloes) in the simulations normalised by the background matter density. The line colours are as in Fig. 4.1. The profiles are plotted only beyond the 'Power radius' (Power et al., 2003) at which numerical convergence is expected. The bottom panel shows the profiles for the WDM simulations normalized to the profile for the CDM-W7 model. 55

4.4 Radial variation of the logarithmic slope of the density profiles of the main haloes in the simulations. Line colours and plotting range are as in Fig. 4.3. 56

4.5 A region of a WDM simulation performed at two different resolutions. The particle mass for the high resolution simulation (*right*) is 29 times smaller than that of the low resolution case (*left*). Only particles in bound structures at this snapshot are shown. Particles are coloured according to the halo to which they belong. The number of particles plotted in each panel is equal to the number of bound-structure particles in the low resolution simulation; we have applied random sampling in the high resolution case. 57

4.6 The particles of Fig. 4.5 traced back to their positions in the initial conditions. The low resolution simulation is shown in the top panel and the high resolution simulation in the bottom panel. Note the highly flattened configurations of spurious haloes. 59

4.7 Mean subhalo sphericities as a function of M_{Max} for the high resolution CDM-W7 (black) and the $m_{1.4}$ (red) runs. The region between the upper and lower 99 percentiles of the CDM distribution is shown in grey; the same region for the $m_{1.4}$ simulation is delineated by the red dotted lines. . 60

4.8 R as a function of $M_{\rm Max}$ for CDM and WDM LRS subhaloes matched to HRS counterparts (those that fail the sphericity cut are still included). The black dots denote CDM subhaloes, blue $m_{2.3}$, green $m_{2.0}$, orange $m_{1.6}$, and red $m_{1.4}$ (the same as Fig. 4.1. 63

4.9 Dot plots of s and $M_{\rm Max}$ for subhaloes in the four different WDM models at low resolution. Blue points correspond to $R \geq 0.94$ and red points to $R < 0.94$. The horizontal, dashed line is $s_{\rm cut}$ and the vertical line is $M_{\rm min}$. All subhaloes are within r_{200b} of the main subhalo centre at redshift zero. . 65

4.10 Dot plots of s and $M_{\rm Max}$ for subhaloes in the four different WDM models at high resolution. The horizontal, dashed line is $s_{\rm cut}$ and the vertical line is $M_{\rm min}$. All subhaloes are within r_{200b} of the main subhalo centre at redshift zero. 66

4.11 Cumulative subhalo mass, $M_{\rm sub}$, (*top panel*) and $V_{\rm max}$ (*bottom panel*) functions of subhaloes within $r < r_{200b}$ of the main halo centre in the high resolution simulations at $z = 0$. Solid lines correspond to genuine subhaloes and dashed lines to spurious subhaloes. The black line shows results for CDM-W7 and the colours lines for the WDM models, as in Fig. 4.1. The black cross in the lower panel indicates the expected number of satellites of $V_{\rm max} > 5.7$ kms^{-1} as derived in the text. 71

4.12 The radial distribution of subhaloes. *Top:* the spherically averaged number density of $M_{\rm sub} > 10^8 {\rm M}_\odot$ subhaloes normalised to the mean overdensity at r_{200b} for our four WDM and one CDM models. The dotted line indicates the CDM main halo density profile from Fig. 4.3, renormalised to pass through the locus of radial distribution points at 250kpc. *Bottom:* the number fraction of subhaloes per logarithmic interval in radius, on a linear-log plot. The area under the curves is proportional to subhalo number, so this plot shows that subhaloes are preferentially found in the outer parts of the halo. The black line corresponds to the CDM model, CDM-W7, while the blue, green, orange and red lines correspond to the $m_{2.3}$, $m_{2.0}$, $m_{1.6}$, and $m_{1.4}$ WDM models respectively. 72

4.13 Cumulative mass fraction in substructures as a function of radius. The black line corresponds to the CDM model, CDM-W7, while the blue, green, orange and red lines correspond to the $m_{2.3}$, $m_{2.0}$, $m_{1.6}$, and $m_{1.4}$ WDM models respectively. 73

4.14 Spherically averaged radial density profiles for subhaloes matched between the high (level 2), intermediate (level 3), and low (level 4) resolution versions of the $m_{1.4}$ simulation. Blue corresponds to high, red to intermediate, and green to low resolution. The density profiles are shown by thick lines down to the smallest radius at which they satisfy the convergence criterion of Power et al. (2003), and are continued by thin lines down to a radius equal to twice the softening length. In the legend, d_L is the distance of the low resolution subhalo from the main halo centre, M_L is the subhalo mass, and M_L/M_H is the ratio between the masses of the low and high resolution counterparts. 75

4.15 Ratio of the intermediate (level 3; red) and low (level 4; green) resolution density profiles of the $m_{1.4}$ subhaloes shown in Fig. 4.14 to the density profile of their high resolution (level 2) counterparts. The blue dashed line indicates the convergence radius for the high resolution subhaloes. . . 76

4.16 Median value of the goodness of fit statistic, Q, for Einasto (blue dots) and NFW (red dots) fits to all subhaloes of $M_{\rm sub} > 10^9 {\rm M}_\odot$, as a function of the WDM particle mass, $m_{\rm WDM}$. In the Einasto fits, we have fixed $\alpha_{\rm ein} = 0.18$. The error bars indicate the upper and lower quartiles of the distribution. The Einasto data points are slightly offset in $m_{\rm WDM}$ for clarity. 78

4.17 Spherically averaged radial density profiles of subhaloes in simulations of different WDM particle mass. The subhaloes have been matched across simulations on the basis of their position and mass. However, it should be noted that in some cases the matches are uncertain. The different colours correspond to different WDM particle masses: red, orange, green and blue to 1.4, 1.6, 2 and 2.3 keV respectively, while black corresponds to the CDM case. In the legend, $d_{1.4}$ is the distance of the subhalo from the main halo centre in the $m_{\rm WDM} = 1.4$keV, $M_{1.4}$ is the mass of the subhalo also in this case, and $M_{1,4}/M_{\rm CDM}$ is the ratio of this mass to that of the CDM counterpart. As in Fig. 4.14 the density profiles are shown by thick lines down to the smallest radius at which they satisfy the convergence criterion of Power et al. (2003), and are continued by thin lines down to a radius equal to twice the softening length 79

4.18 Ratio of the density profiles of matched subhaloes in simulations of different WDM particle mass relative to the mass of the CDM counterpart. The colours are as in Fig. 4.17 as is the use of thick and thin lines. 80

4.19 Central masses of field haloes (left) and subhaloes within r_{200b} (right), evaluated within radii of 2 kpc (crosses) and 300pc (circles) as a function of total mass. Different colours correspond to different simulations: black for CDM-W7, blue, green, orange and red for models $m_{2.3}$, $m_{2.0}$, $m_{1.6}$, and $m_{1.4}$ respectively. 83

4.20 $M_{\rm halo}$ vs. $V_{\rm max}$ for field haloes. The black dots show the data for the CDM-W7 simulation and the black line represents the mean relation. The colour dots show data for the WDM simulations: blue, green, orange and red for models $m_{2.3}$, $m_{2.0}$, $m_{1.6}$, and $m_{1.4}$ respectively. The mean relation is shown only for the $m_{2.3}$ WDM model in which the number of subhaloes is largest and thus the least noisy. 84

4.21 $V_{\rm max}$ vs. $r_{\rm max}$ for independent haloes (top) and subhaloes (bottom). The black dots show the data for the CDM-W7 simulation and the black line represents the mean relation in the case. The dotted line corresponds to a ΛCDM simulation using the WMAP1 cosmological parameters. The colour dots show data for the WDM simulations: blue, green, orange and red for models $m_{2.3}$, $m_{2.0}$, $m_{1.6}$, and $m_{1.4}$ respectively. The mean relation is shown only for the $m_{2.3}$ WDM model in which the number of subhaloes is largest and thus the least noisy. The solid lines of the top panel are reproduced in the bottom panel as dashed lines. 85

5.1 Gas temperature maps of the IGM at redshift 6 for the four simulations (*left to right, top to bottom:* CN, WN, CW, WW). Intensity indicates squared gas density projected along the line of sight (S) and hue gas temperature: blue through green to red corresponds to cold through to hot gas on a logarithmic scale as shown inthe two-dimensional colour table. Each panel is 3Mpc (comoving) on each side, and is centred on the centre-of-mass of the high resolution region. 93

5.2 Star-Formation rate in the high resolution region as a function of lookback time for the four different models. CDM models are indicated in black and WDM in red; no-winds models in dotted lines and winds models in solid lines. Redshift is indicated along the top x-axis. 94

5.3 The ratio of the cumulative number of Lyman-α photons to gas produced as a function of redshift. CDM models are indicated in black and WDM in red; no-winds models in dotted lines and winds models in solid lines. Redshift is indicated along the top x-axis. The vertical dashed blue line indicates the Planck+WMAP polarisation preferred value of $z_{\rm re} = 11.1$ and the shaded green region the 1σ errors on that measurement (Planck Collaboration et al., 2013a). The horizontal blue dashed line marks the threshold for reionisation if $f_{\rm esc} = 1$ and the dotted line the same quantity for $f_{\rm esc} = 0.1$. The top panel assumes a Salpeter IMF, and the bottom a Chabrier. 96

List of Tables

2.1 Selected parameters of the Aquarius simulations used in this Chapter. The simulation name encodes the halo label (Aq-A, B, and so on) and the numerical resolution level (1 to 5, hereafter L1, L2, L3, L4, L5). $m_{\rm p}$ is the particle mass, r_{200} the radius of the sphere of density 200 times the critical density, M_{200} the halo mass within r_{200}, $n_{\rm s}$ the number of subhaloes within the main halo, λ the spin parameter as determined by Boylan-Kolchin et al. (2010), and q, p the halo shape axis ratios b/a and c/b respectively (Vera-Ciro et al., in preparation). The axes are defined as $a \geq b \geq c$ for ellipsoids determined using the method of Allgood et al. (2006). Values with * or † superscripts were calculated for haloes at resolution levels L4 or L3 respectively. As the smallest subhaloes determined by SUBFIND contain 20 particles, the minimum subhalo mass in each simulation is $20m_{\rm p}$. 12

3.1 Basic parameters of the simulations analysed in this Chapter. The top two simulations are taken from the Aquarius sample of CDM dark matter haloes published in Springel et al. (2008a). The simulations are of a single halo, Aq-A, at different numerical resolutions. The bottom three are warm dark matter counterparts to the CDM simulations, as described in the main text. The second to fifth columns give the particle mass ($m_{\rm p}$), the radius of the sphere of density 200 times the critical density (r_{200}), the halo mass within r_{200} (M_{200}) and the number of subhaloes within the main halo ($N_{\rm s}$). The smallest subhaloes, determined by SUBFIND, contain 20 particles. 30

4.1 Parameters of the simulations. The parameter α determines the power spectrum cutoff (Eqn. 4.2); m_{WDM} is the thermal relic mass corresponding to each value of α; and M_{th} is the cutoff mass scale defined using a top hat filter as described in the text. The final column contains the particle masses that, when combined with the $\nu = 1.12$ transfer function of Viel et al. (2005), give the best approximation to our $\nu = 1$ transfer functions. . 52

4.2 Properties of the main friends-of-friends halo in each high resolution simulation. The radii r_{200} and r_{200b} enclose regions within which the mean density is 200 times the critical and background density respectively. The masses M_{200} and M_{200b} are those contained within these radii. We also reproduce data from the original Aquarius Aq-A2 halo. 54

5.1 Parameters of the central galaxies and their haloes generated in each simulation. r_{200} is defined as the radius enclosing the spherical overdensity 200 times the critical density of the Universe, M_{200} is the mass within that radius, and M_{stellar} the stellar mass of the galaxy as defined in the text. . . 92

Declaration

The work described in this thesis was undertaken between 2009 and 2013 while the author was a research student under the supervision of Dr. Adrian Jenkins and Prof. Carlos S. Frenk at the Institute for Computational Cosmology in the Department of Physics at the University of Durham. This work has not been submitted for any other degree at the University of Durham or any other university.

Parts of this work have appeared in the following papers:

- Lovell, Mark R. et al., 2013, arXiv e-prints – Chapter 4
- Lovell, Mark R. et al., 2012, MNRAS, **420**, 2318 – Chapter 3
- Lovell, Mark R.; Eke, Vincent R.; Frenk, Carlos S.; Jenkins, Adrian., 2011, MNRAS, **413** , 3013 – Chapter 2

All figures were produced by the author, except the following:

- Figure 3.2: produced by A. Jenkins

Details of where simulations were run, and by whom, is provided below:

- Aquarius Project: carried out by the Virgo Consortium at the Leibniz Computing Centre, Garching, Germany, at the Computing Centre of the Max-Planck-Society in Garching, at the Institute for Computational Cosmology in Durham, and on the STELLA supercomputer of the LOFAR experiment at the University of Groningen.
- Warm dark matter and SPH simulations: carried out by the Virgo Consortium at the Supercomputer Center of the Chinese Academy of Science, and the Cosmology Machine supercomputer at the Institute for Computational Cosmology, Durham

The copyright of this thesis rests with the author. No quotation from it should be published without his prior written consent and information derived from it should be acknowledged.

Acknowledgements

I would like to start by thanking my family, that is Mum, Dad, Nicholas and Grandma for all the love they have shown me over so many years. I didn't get to see them often, until Mum got Facetime anyway!

I have felt really fortunate to have had a large church family in the form of King's Church Durham these last five and a half years. Much though I would like to name everybody one by one, I would like to single out anyone who has every been in my church house group: Edith Light, Iris Prizeman, Melody Briggs, Theresa & Pete Phillips, Yan Wong (AKA cooking consultant!), Abi Stewart, Shanti & Sunil Thumati, Sarah Tripp, Nicola Bates, Mad Coburn, Hazel White, Wes Hill, Chris & Hannah Juby, Dereck & Evelyn Paddon, Mark & Becca Dobie, and Josh Bargh: thank you all for being part of this journey and putting up with my Wednesday evening histrionics. And that is not forgetting Tim Wiles, who along with Robert Bettles forms the Welsh Vanguard of the church. Cariad gymraeg i bawb!

Hopefully my three housemates whilst I have been studying for my PhD – Fraser Riddell, Ed Spencer, and Ian Blatcher – have enjoyed the shared meal times and the excitement of leaks in the ceiling, failed heating, and other acts of Drama. Thank you for being there in the evenings when I needed someone to talk to and didn't fancy cooking!

Within the Physics department, I want to thank first of all my supervisors: Adrian Jenkins, Carlos Frenk, and Vince Eke, along with my collaborators Liang Gao and Tom Theuns for their input. I am grateful to our external collaborators, Alexey Boyarsky and Oleg Ruchayskiy, who inspired the work on sterile neutrinos. No coffee was used in the making of this thesis, however industrial quantities of tea were consumed every day at 11am and 4pm and so my thanks go to Lynne Wall – our Senior Dehydration Elimination Specialist – for her telepathic qualities and tea-dispensing acumen. For helping me get off the ground with running GADGET and the like, Andrew Cooper and Owen Parry made my life a heck of a lot easier and I was really greatful for all the hours they spent digging through my code. I would also like to thank my PhD examiners, Richard Bower and Martin Haehnelt, for a careful reading of this manuscript and their suggested corrections.

It is a truth universally acknowledged, that if John Helly and Lydia Heck didn't exist

the entire ICC would collapse around our ears in a firestorm of segfaults and broken cluster nodes. I therefore want to put on record my thanks to both of them for all their hard work in supporting me along with the rest of the researchers here.

I would also like to thank everyone who has come down to tea breaks, had lunch in the Bransden room, attended astro-ph lunch and student journal club, and been there for me when I've been a mess: Michelle Furlong, Rachel Kennedy, Nico Tejos, Violeta Gonzalez, Lilian Jiang, Michael Hogan, and Chris Harrison come to mind, whilst so many others have been there at just the right time on other occasions. A special thank you goes to Tamsyn McNaught-Roberts for proof-reading this text.

Last but not least, I have felt that the last four years have actually been a shared journey for four us who started at the same year group, who have each had our own very different trials and difficulties and joys which we have suffered and shared. The other three are Daniel Farrow, Rachael Livermore, and Alice Danielson. I will miss you.

Chapter 1

Introduction

1.1 Dark Matter, Zwicky and all that

The first clues that visible matter could not account for the behaviour of the Universe on all scales can be traced back to dynamical analyses of the Coma cluster in the 1930s (Zwicky, 1933). A naive study of a galaxy cluster would suggest that it is dominated by stars. If this were the case, the stellar and total masses should be very similar. One can infer the amount of mass that is present in stars quite simply by measuring the amount of starlight and assume a stellar synthesis population model, and obtain dynamical mass from the Doppler shifts of each galaxy provided the system is in virial equilibrium. The Doppler shifts – and thus velocities measured – suggested something very surprising. The velocities were so high that the member galaxies would be unbound from the cluster if all the mass were in the stars. Zwicky therefore proposed that an unseen form of matter – "dunkle Materie" (dark matter) – was also present in the cluster, its gravity binding all the galaxies together.

Further evidence emerged in the 1970s and 1980s that the motions of stars around the Milky Way and other disc galaxies were incompatible with the observed matter distribution (e.g. Bosma, 1978). The spiral galaxies are supported against gravitational collapse by rotation, so the orbital velocity $V_{\rm c}$ as a function of radius r is related to the mass enclosed within r, $M(<r)$, under the assumption of spherical symmetry by the equation:

$$V_c{}^2 = GM(<r)/r, \tag{1.1}$$

where G is the universal gravitational constant. The stellar light (and therefore stellar mass) is concentrated towards the galaxy's central bulge, so $M(r \gg r_{\rm bulge})$ should be roughly constant and therefore we expect $V_{\rm c}(r) \propto r^{-1/2}$. However, observations revealed $V_{\rm c}(r) \approx$ constant, suggesting there was far more mass in the outskirts of the galaxy than is observed. This discrepancy between the observed and dynamic masses is now seen in the rotation curves of all spiral galaxies and low surface brightness (LSB) galaxies, and also in the velocity dispersions of the dwarf spheroidal galaxies that orbit the Milky Way, making a convincing case that all of these systems possess undetected mass.

The next piece of evidence was found once again in studies of clusters. Einstein's theory of general relativity had predicted that the trajectory of a light ray could be altered by presence of matter, in such a way that the size of the deflection is related to the amount of mass. It follows that the matter distribution in a nearby galaxy could bend the light from a much more distant galaxy, an effect known as 'gravitational lensing'. If one can analyse the way that light bends around a cluster, it is then possible to establish that cluster's mass profile. It became possible in the early 1990s to observe these lensing effects, and in so doing measure cluster mass profiles: the results were again consistent with a much higher mass content than would be expected from the stellar component (e.g. Tyson et al., 1990). Much of the mass has since be identified as hot, X-ray emitting gas, but this is not sufficient to account for the observed kinematics and lensing (Briel et al., 1992; White et al., 1993). Either our understanding of general relativity is not correct on these scales, or there must be more mass present than one can see.

1.2 The ΛCDM Model

Given the evidence presented in the previous section, it had become the standard paradigm to consider the dynamics of galaxies and clusters to be dominated by dark matter. However, to claim to have a complete understanding of cosmology it was necessary to see whether this dark matter could, in conjunction with the known baryonic matter, be consistent with the expansion history of the Universe: excessive amounts of extra, gravitating matter would have a profound effect on how structures collapsed and evolved. Guth (1981) proposed that some inflationary process very early in the history of the Universe had forced the density of the Universe to be close to its critical value for recollapse. Simulations run by e.g. Davis et al. (1985), however, showed that the best fits between observations and simulation predictions were attained if $\Omega = 0.2$. Later redshift surveys such as Saunders et al. (1991) found that the observed distribution of galaxies on large scales exacerbated this tension. A combination of cluster modelling and primordial element abundance measurements also required a small Ω (White et al., 1993). It was apparent that something very important was missing from the model.

A paradigm shift in the field arrived in 1998. Observations of type Ia supernova showed that the expansion of the Universe was accelerating rather than decelerating (Riess et al., 1998; Perlmutter et al., 1999) and that therefore the low redshift Universe matter-energy density was dominated not by dark matter but instead the mysterious 'dark energy' as suggested by Efstathiou et al. (1990). This result enabled astronomers to pin down the amount of mass in the Universe more precisely – having reallocated much of the mass-energy budget to dark energy – and could say with confidence that the matter density is about 30 per cent of the critical density (matter density parameter $\Omega_m = 0.3$). Later work based on galaxy clustering (Cole et al., 2005) and cosmic-microwave background measurements (e.g. Spergel et al., 2003; Planck Collaboration et al., 2013b) has refined this picture, such that the existence of dark matter is largely accepted within the community. However, its identity remains very much unknown. So...

1.3 What's the matter?

The most basic requirement for dark matter is that it interact very weakly, if at all, with baryonic matter. Throughout the 1990s the dominant paradigm was that the dark matter be non-baryonic (undiscovered particles, neutrinos but see following paragraph). This option had the freedom to satisfy this criterion very simply at the price of having to invoke a particle not known to exist, should the neutrino turn out to be an unviable candidate. To save adding a new particle to the standard model, other researchers proposed that dark, baryonic objects such as brown dwarfs and black holes may instead constitute the dark matter. They would reside in the haloes of galaxies in large quantities, and were referred to as massive compact halo objects (MACHOs). This view was immediately challenged by measurements of primoridal element abundance ratios that set the baryon density parameter Ω_b to be less than Ω_m; nevertheless attempts were still made to detect MACHOs via gravitational microlensing (Alcock et al., 2000). These studies found that no more than 20 per cent of the Milky Way halo could be made up of MACHOs, thus it became increasingly untenable that baryons could constitute the dark matter.

The first attempts to devise and test non-baryonic dark matter models took place in the late 1970s and early 1980s. Three different classes of model were proposed, and classified by the velocities of the particles. The first arose from theories considering the neutrino of the standard model, which had the attraction that it was known to exist, and interacted very weakly with other standard model particles. Within the standard model, the neutrino is set to be massless: therefore in any extension to the standard model that could allow the neutrino to be a dark matter candidate, its mass would have to be very small, much smaller than that of the electron. It would therefore freeze out of the primordial plasma relatively late, so late that it would still be relativistic at matter-radiation equality. It would be able to free-stream out of all but the largest gravitational potentials seeded by quantum fluctuations, and would therefore erase perturbations that correspond to scales smaller than clusters (Szalay and Marx, 1976; White et al., 1983). A particle of this sort is known as hot dark matter (HDM).

Alternative theories relied on particles not contained within the standard model. These included supersymmetric extensions to the standard model in which each standard model particle has a supersymmetric partner: a mass eigenstate of these supersymmetric particles – known as a neutralino – could then act as a dark matter candidate. It would have a mass at least of the order of a GeV, and therefore freeze out of the thermal plasma at much earlier redshifts than would the neutrino, such that it would soon become non-relativistic and unable to free-stream out of any gravitational potential smaller than that of an Earth mass. This sort of dark matter candidate would be cold dark matter (CDM).

These two theories made very different predictions for the distribution of galaxies in the local universe. HDM erases structure on all scales bigger than that even of galaxies, in which case the luminous structures observed would be formed by fragmentation of the few structures large enough to collapse, most often cluster-mass haloes: this scenario is known as ‘top-down’ galaxy formation and produces a distribution of galaxies that is highly clustered. On the other hand, CDM forms dark matter haloes on scales much smaller than those of galaxies. These haloes can then merge together to form progressively large structures, up to the range of galaxies and clusters. This process is known as the ‘bottom-up’ scenario, and galaxies would be much less clustered distributed than is the case in HDM. Studies performed by the likes of Davis et al. (1985) compared simulations of these two models with galaxy surveys, and found that the true galaxy distribution was much more akin to that predicted by CDM than by HDM. They therefore concluded that CDM is the dominant matter component in the Universe. Ironically, the neutrino has since been found to have a mass (see Gonzalez-Garcia and Maltoni, 2008, and references therein) and therefore we know HDM to exist whilst the dominant CDM particle has yet to be identified!

A third model of dark matter has only more recently begun to be considered fully. Davis et al. (1985) acknowledged that it is possible for the dark matter to be neither cold nor hot but instead a model with characteristics of both – warm – for which HDM-style free-streaming would occur but on scales of the smallest galaxies, so galaxy formation would still take place hierarchically. It seemed highly unlikely back in the early 1980s that any new particle candidate would have this property. By the mid 1990s, however, extensions to the standard model that seek to explain neutrino masses had predicted the existence of a 'sterile' neutrino (Dodelson and Widrow, 1994) with these free-streaming properties. This early theory failed because a model that contains just one sterile neutrino is unable to endow only one active neutrino with mass rather than all three, however other researchers continued to explore the possibilities of sterile neutrinos. In particular, the neutrino minimal standard model (νMSM; Asaka and Shaposhnikov, 2005), predicted the existence of not one but a triplet of sterile neutrinos. These particles would experience neutrino flavour oscillations with the active neutrinos, and would interact with baryonic matter via gravity alone. The lightest sterile neutrino of the triplet would be stable within the lifetime of the Universe and thus a dark matter candidate. Intriguingly, the model also predicts that they may be produced by two different channels: a 'non-resonant' and a 'resonant'. The latter of these would produce a lightest sterile neutrino with very small free-streaming velocity similar to those of CDM candidates, however the former will have a velocity drawn from a much broader distribution such that it would constitute WDM. It will exhibit free-streaming on scales around that of dwarf galaxies, such that the smallest galaxies form by monolithic collapse and all larger galaxies are built hierarchically. The aim of this thesis is to develop and perform tests to distinguish between WDM and CDM.

1.4 Constraining WDM with observations of the early Universe and X-ray decays

As stated in the previous section, the first WDM cosmologies were proposed with the suggested existence of the sterile neutrino (Dodelson and Widrow, 1994). Perhaps the first attempt to test WDM in a cosmological simulation was that of Colombi et al. (1996), who simulated HDM, CDM, and WDM models: however this work took the matter density parameter $\Omega_{\rm m} = 1$ and thus the absence of dark energy from the model prevented it from matching observations. Bode et al. (2001) were the first to address this issue in the $\Omega_{\rm m} = 0.3$ era, and inspired further interest in the subject. They found that the WDM matter power spectrum could be related simply to the mass the dark matter particle would have if it were a thermal relic ($m_{\rm p}$). It is this mass (but see also Viel et al., 2005) that subsequent authors have used when characterising their models. An unexpected result of Bode et al. (2001) was that filaments were found to fragment into regular patterns. These fragments coalesced into small haloes, so many that they were more numerous than the haloes that formed just above the mass cutoff. It was later shown that these haloes are actually spurious, resolution dependent phenomena (Wang and White, 2007). These objects have provided a considerable challenge to attempts to count the true number of haloes generated in WDM models, and we present a solution for this problem in Chapter 4.

Multiple avenues have since been explored to further test and constrain WDM models. The lack of small scale power early in the history of the Universe would likely have a profound impact on the properties of the Lyman-α forest. Hydrodynamical simulations of the high redshift Universe have been run compared with the absorption features found in QSO sightlines, with a view to measure the likely effect of WDM on the high-redshift gas distribution (Viel et al., 2005, 2006; Seljak et al., 2006; Boyarsky et al., 2009a; Viel et al., 2013a). These studies have placed a lower limits in the region of 1.5-2.5keV on the particle mass (assuming a thermal relic particle) although uncertaintites remain in the ability to simulate accurately the inter-galactic medium (IGM) at these high redshifts.

A related field of study is that of reionisation. The lack of small scale power delays the onset of structure formation, therefore the epoch of reionisation would occur later (Barkana et al., 2001). One probe of the epoch of reionisation may be obtained from the CMB. The WMAP year-1 data (Kogut et al., 2003; Spergel et al., 2003) determined the 'instantaneous redshift of reionisation' to be $z_{\rm re} \sim 20$, and therefore stated they had ruled out WDM in reference to Barkana et al. (2001). Further analysis of the WMAP data, however, revised $z_{\rm re}$ down to ~ 11 and thus relieved much of the tension on the model: the most recent Planck+WMAP polarisation constraint is $z_{\rm re} = 11.1 \pm 1.1$ (Planck Collaboration et al., 2013a). The potential for star-formation in WDM filaments could alter the way that reionisation proceeds in WDM models (Gao and Theuns, 2007), and this possibility makes this field one that is ripe for further examination.

For some particle physics models, an upper constraint on the particle mass can be obtained by X-ray decay measurements. Whilst a CDM candidate could be detected by its annihilation into γ-rays (e.g. Springel et al., 2008b), a particle such as a sterile neutrino could be detected by its decay into X-rays (Abazajian et al., 2001; Boyarsky et al., 2009c). The sterile neutrino rest mass m_s is related to the half-life, such that a more massive particle would decay more readily and have a greater luminosity. A similar correlation is seen with the sterile neutrino mixing angle – the parameter that determines how readily the sterile neutrion can oscillate into another neutrino flavour, denoted by θ – so X-ray observations of objects such as M31 and dwarf spheroidal (dSph) galaxies can place constraints in the $m_s - \theta$ plane (Boyarsky et al., 2009c,b).

1.5 The Local Group

Much of the effort to constrain the properties of dark matter has been centered around the large scale Universe, such as gravitational clustering and the CMB. We are now also entering an era of near-field cosmology, where efforts are being made to understand dark matter using the properties of local galaxies, in particular those of the Local Group. This term is used to refer collectively to our own Milky Way galaxy, M31, M33, and their associated satellite galaxies. The Milky Way and M31 are both thought to be embedded in dark matter haloes of mass $\sim 10^{12}\rm{M}_{\odot}$, whilst the satellites live in smaller 'subhaloes' that are orbiting within the larger 'main haloes' of the two largest galaxies. We assume in this work that each of the satellites has its own subhalo, and so a study of the properties of simulation dark matter subhaloes should map to the properties of the satellite galaxies; we also assume that these properties are not heavily influenced by baryonic physics (but see di Cintio et al., 2011; Brooks and Zolotov, 2012; Parry et al., 2012; Garrison-Kimmel et al., 2013).

One conspicuous property of the dSph galaxies is that their velocity dispersions are very high for their stellar densities. Some of the least luminous dSphs have luminosities similar to those of globular clusters, however the velocity dispersions of these systems suggest mass-to-light ratios as high as 4000 (Walker et al., 2009, 2010; Wolf et al., 2010). It therefore appears that these dSphs are amongst the most dark matter-dominated objects in the Universe, and are thus an ideal 'laboratory' in which to study dark matter physics. Upon the assumption that every dark matter subhalo large enough to retain a gas reservoir and thus form stars will host a dSph, these galaxies offer a number of exciting constraints on the properties of dark matter.

In this study, we consider three properties of dSphs to test our dark matter models: their spatial distribution, densities, and abundances. With regard to the first of these, it is suggested that the satellites of both the Milky Way and M31 have correlated orbits (Metz et al., 2009; Ibata et al., 2013), and are perhaps even rotationally supported, so any theory of dark matter should be able to explain the observed distribution of satellites. The second point relates to the extreme mass to light ratios mentioned earlier: we require that the simulated subhalo densities are consistent with the satellites' velocity dispersions. Thirdly, we also require that our models are able to reproduce at least as many subhaloes as there are satellites observed (Klypin et al., 1999; Moore et al., 1999; Boylan-Kolchin et al., 2011). All three of these points will be addressed in this thesis.

1.6 Structure of this Thesis

This thesis is structured as follows. In Chapter 2 we present work on the orbits of satellite galaxies around analogues of the Milky Way dark matter halo. Chapter 3 examines the effect of WDM on the central densities of substructures, and is expanded in Chapter 4 with the introduction of a more up-to-date set of cosmological parameters and a study on the number of satellites. We apply gas hydrodynamics to WDM with a view to examining reionisation in WDM in Chapter 5 and draw conclusions in Chapter 6.

Chapter 2

Orbits of satellite galaxies

2.1 Introduction

It has been known for several decades that the 11 'classical' satellites of the Milky Way define a thin plane around the Galaxy (Lynden-Bell, 1976). Some of the faint satellites recently discovered in the Sloan Digital Sky Survey (SDSS; York, 2000; Willman et al., 2005a,b; Sakamoto and Hasegawa, 2006; Zucker et al., 2006a,b; Irwin et al., 2007; Walsh et al., 2007; Belokurov et al., 2008) also appear to have an anisotropic distribution reminiscent of that of the classical 11 (Metz et al., 2009). The presence of such a 'disc-of-satellites' suggests a common plane of rotation in the Milky Way. Measurements of proper motions, which are now possible for some of the satellites, can be used to constrain the nature of any systemic rotation (Metz et al., 2008; Lux et al., 2010).

In tandem with these observational developments, advances in computational cosmology now make it possible to simulate galactic haloes with sufficient resolution to probe the properties of satellites and investigate the origin of their flattened configuration. N-body simulations from cold dark matter (CDM) initial conditions show that a large number of accreted haloes survive to the present, making up a population of 'subhaloes' of the 'main halo,' some of which could host the satellites.

The observations, however, suggest a complex formation history. First, the number of satellites identified so far is much smaller than the number of dark subhaloes in the simulations, giving rise to the so-called 'missing satellite problem' (Moore et al., 1999; Klypin et al., 1999). Secondly, the thin ring around the sky delineated by the classical satellites contrasts with the distribution of subhaloes in the simulations which is triaxial (Libeskind et al., 2005; Zentner et al., 2005). Thirdly, the inferred angular momentum vectors of the majority of the classical satellites in the Milky Way point towards a patch on the sky of diameter no greater than 30°, which has led Metz et al. (2008, 2009) to argue that the observed satellites cannot have formed in cold dark matter subhaloes. In contrast to the Milky Way, NGC 5084 appears to have a population of satellites orbiting in the opposite sense to the galaxy (Carignan et al., 1997).

The combination of 'missing satellites', an anisotropic distribution and coherent orbits is sometimes viewed as a challenge to the CDM model (e.g. Moore et al., 1999; Metz et al., 2008). However, a number of studies using semi-analytic modelling and hydrodynamic simulations have shown that a relatively small satellite population is a natural outcome of galaxy formation in the CDM cosmology (e.g Kauffmann et al., 1993; Bullock et al., 2000; Benson et al., 2002; Somerville, 2002; Koposov et al., 2009; Muñoz et al., 2009; Busha et al., 2010a; Cooper et al., 2010; Li et al., 2010; Macciò et al., 2010; Wadepuhl and Springel, 2010). The simulations show that satellites form only in a small fraction of subhaloes which turn out to be those that had the most massive progenitors at the time of accretion (Libeskind et al., 2005). Furthermore, disc-like subhalo configurations are seen to form in ΛCDM cosmological simulations (Kang et al., 2005; Zentner et al., 2005; Libeskind et al., 2007, 2009). Such systems appear to be related to the preferential accretion of haloes along the filaments of the cosmic web. Haloes tend to fall along the central spines of filaments, so that the range of trajectories, and thus orbits, that they acquire when they enter a halo is restricted (Libeskind et al., 2009).

Shaw et al. (2006), Warnick and Knebe (2006) and Libeskind et al. (2009) confirmed the conclusion of Libeskind et al. (2005) that satellite accretion is a highly anisotropic process and found in their simulations a significant population of subhaloes that co-rotated with the spin of their hosts. However, Shaw et al. (2006) simulated galaxy cluster haloes, not galactic haloes; Warnick and Knebe (2006) also focused on cluster haloes except for one example of a galaxy halo which, however, had only moderate resolution (a minimum subhalo mass of $m_{\rm min} = 5.7 \times 10^7 {\rm M}_\odot$). The largest sample of galaxy halo simulations so far is that of Libeskind et al. (2009). They analysed 436 haloes but were only able to resolve subhaloes of mass $m_{\rm min} \geq 2.76 \times 10^9 {\rm M}_\odot$.

In this study, we analyse the state-of-the-art, high resolution simulations of six galactic haloes of mass $\sim 1 \times 10^{12} {\rm M}_\odot$ of the Aquarius project (Springel et al., 2008a). These simulations resolve subhaloes of mass exceeding $\sim 10^5 {\rm M}_\odot$. We calculate the angular momentum of subhaloes, and use the results to interpret the Milky Way data. The Chapter is organised as follows. In Section 2.2 we briefly describe the Aquarius project and the analysis performed for this Chapter. The results follow in Section 2.3 and our conclusions in Section 2.4.

2.2 The simulations

The Aquarius project is a set of dark matter simulations containing haloes similar in size and environment to those of the Milky Way; each one has been run from $z = 127$ to $z = 0$. There are six different haloes (Aq-A - Aq-F), each of which has been resimulated at least two levels of resolution (L1, the highest, down to L5, the lowest). They were performed using the GADGET-3 code (Springel et al., 2008a). In all cases, the resimulations at different resolutions show remarkable convergence in the positions and internal properties of subhaloes. This project has already yielded several interesting results, including a study of the near-universality of halo density profiles (Springel et al., 2008a; Navarro et al., 2010), predictions for the γ-ray signal from annihilating dark matter in the galactic halo (Springel et al., 2008b) and for direct dark matter detection experiments (Vogelsberger et al., 2009). A summary of key parameter values for each simulation is given in Table 3.1.

It is important for this study to establish that the sample of six Aquarius haloes can be considered at least approximately representative of the population of Milky-Way mass haloes as a whole. The Aquarius haloes are all drawn from the same parent cosmological simulation, and it is possible to address this issue directly for several properties. The spins, concentrations and formation histories of the Aquarius haloes are compared to the parent population in Boylan-Kolchin et al. (2010). Broadly speaking, the properties of the Aquarius haloes span the expected range for the population as a whole. We give the values of the halo spin, concentration and formation redshift, defined as the redshift when half the halo mass is assembled, in Table 3.1. Also in the table we list the shape axis ratios for the haloes, approximating them as ellipsoids. The axis ratios are taken from Vera-Ciro et al. (in preparation) and calculated for ellipsoids which are determined by applying the iterative method of Allgood et al. (2006) to the haloes with the substructure removed (actually to the 'main halo', defined below). The six haloes show a range of

Name	m_{p} [$\mathrm{M}_\odot$]	r_{200} [kpc]	M_{200} [$\mathrm{M}_\odot$]	n_{s}	λ	c^*_{NFW}	z_{form}	q	p
Aq-A1	1.712×10^3	245.76	2.523×10^{12}	197484	-	16.11	1.93	-	-
Aq-A2	1.370×10^4	245.88	2.524×10^{12}	30177	0.027	16.19	1.93	0.866	0.687
Aq-A3	4.911×10^4	245.64	2.524×10^{12}	9489	-	16.35	1.93	0.862	0.688
Aq-A4	3.929×10^5	245.70	2.524×10^{12}	1411	-	16.21	1.93	0.844	0.700
Aq-A5	3.143×10^6	246.37	2.541×10^{12}	246	-	16.04	1.93	0.830	0.685
Aq-B2	6.447×10^3	187.70	1.045×10^{12}	31050	0.022	9.72	1.39	0.820*	0.839*
Aq-C2	1.399×10^4	242.82	2.248×10^{12}	24628	0.020	15.21	2.23	0.711*	0.770*
Aq-D2	1.397×10^4	242.85	2.519×10^{12}	36006	0.012	9.37	1.51	0.846*	0.901*
Aq-E2	9.593×10^3	212.28	1.548×10^{12}	30372	0.017	8.26	2.26	0.898*	0.674*
Aq-F2	6.776×10^3	209.21	1.517×10^{12}	35041	0.050	9.82	0.55	0.700†	0.866†

Table 2.1: Selected parameters of the Aquarius simulations used in this Chapter. The simulation name encodes the halo label (Aq-A, B, and so on) and the numerical resolution level (1 to 5, hereafter L1, L2, L3, L4, L5). m_{p} is the particle mass, r_{200} the radius of the sphere of density 200 times the critical density, M_{200} the halo mass within r_{200}, n_{s} the number of subhaloes within the main halo, λ the spin parameter as determined by Boylan-Kolchin et al. (2010), and q, p the halo shape axis ratios b/a and c/b respectively (Vera-Ciro et al., in preparation). The axes are defined as $a \geq b \geq c$ for ellipsoids determined using the method of Allgood et al. (2006). Values with * or † superscripts were calculated for haloes at resolution levels L4 or L3 respectively. As the smallest subhaloes determined by SUBFIND contain 20 particles, the minimum subhalo mass in each simulation is $20m_{\mathrm{p}}$.

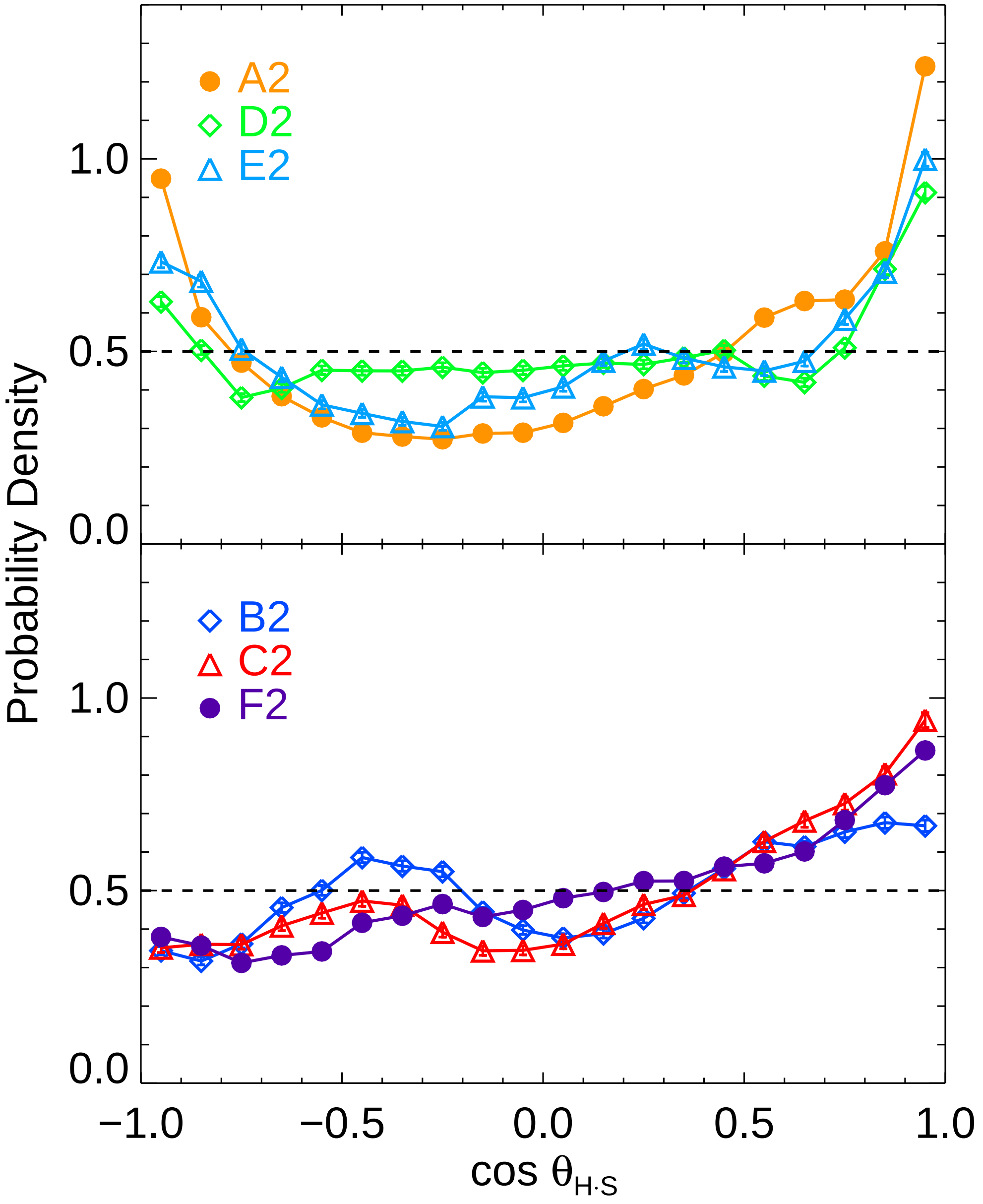

Figure 2.1: The distribution of cos $\theta_{\rm H\cdot S}$ for the six Aquarius haloes at resolution level L2, where $\theta_{\rm H\cdot S}$ is the angle between the main halo spin and subhalo orbit vectors. The six are separated into two panels according to whether or not they exhibit an antiparallel tail greater than 0.5. *Top panel:* results for Aq-A2 (orange), Aq-D2 (green), and Aq-E2 (light blue). *Bottom panel:* as above, but for Aq-B2 (blue), Aq-C2 (red), and Aq-F2 (purple). In both cases, the dashed line corresponds to an isotropic distribution.

shapes and are typical for ΛCDM haloes (Allgood et al., 2006; Bett et al., 2007).

The halo membership of each particle is determined using the friends-of-friends (FOF) algorithm (Davis et al., 1985). The particles in each FOF group are, in turn, assigned to self-bound structures using the SUBFIND code (Springel et al., 2001a). We call the largest of these self-bound substructures the main halo, and the remainder we call subhaloes. A small proportion (<1 per cent) of the particles within the FOF group are found to form a 'fuzz' that is not gravitationally bound to any other object; they are not considered any further.

Our primary aim is to determine the orientations of dark matter subhalo orbits in the Aquarius simulations and compare the results with data for galactic satellites. We calculate the 'main halo spin', defined as the sum of the angular momenta of all main halo particles about their centre-of-mass. For each subhalo, we calculate the 'subhalo orbital spin', defined as the vector associated with the angular momentum of each subhalo about the centre of the main halo. We then calculate the cosine of the angle, $\theta_{\mathrm{H \cdot S}}$, between the main halo spin vector and the subhalo orbit vector for every subhalo associated with that main halo. These subhaloes are tracked back to the initial conditions in order to investigate the origin of the patterns that we find.

2.3 Results

We first describe our calculation of the angular momentum distributions of various populations and then investigate their origin.

2.3.1 Angular momentum distributions of subhaloes

We compute cos $\theta_{\mathrm{H \cdot S}}$ for each of the six L2 haloes at $z = 0$ as described above, and plot the results in Fig. 2.1 as a probability density; an isotropic distribution of angular momenta in this plot corresponds to a horizontal line at 0.5.

All the haloes show a statistically significant bias for subhalo orbits to be aligned (parallel) to the rotation of the parent main halo, as found by Shaw et al. (2006) and Warnick and Knebe (2006). The average fraction of corotating subhaloes in the Aquarius haloes is 57 per cent, with a narrow range between 54 per cent and 61 per cent. This is consistent with the average of 59 per cent quoted by Warnick and Knebe (2006). This

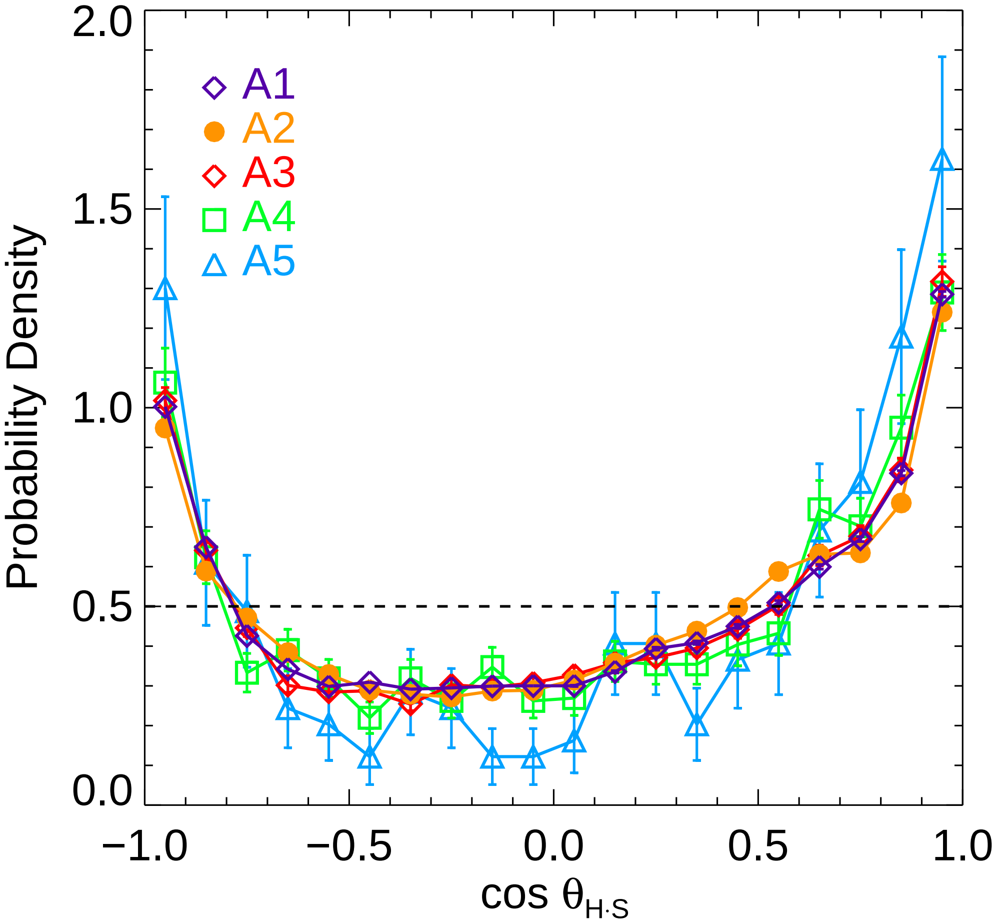

Figure 2.2: The distribution of cos $\theta_{\rm H\cdot S}$ for all the resolution levels of Aq-A. Aq-A1 contains 197484 subhaloes (purple), Aq-A2 30177 (orange), Aq-A3 9489 (red), Aq-A4 1411 (green), and Aq-A5 246 (light blue). The error bars denote Poisson uncertainties.

result is a natural outcome of tidal torque theory (Hoyle, 1951; White, 1984) when the primordial dark matter protohaloes exert torques on one another, inducing net spins as they condense.

We also find significant numbers of nearly *anti*-parallel orbits in three of our haloes. Specifically, haloes Aq-A2, Aq-D2, and Aq-E2 show a significant proportion of subhalo orbits in the -1.0 <cos $\theta_{\rm H\cdot S}$ < -0.9 bin (9.5 per cent, 6.3 per cent, and 7.3 per cent respectively where 5 per cent would be expected for a random distribution - the Poisson errors on our L2 measurements are negligible), whilst Aq-B2, Aq-C2, and Aq-F2 do not. We have separated the haloes into two panels according to this property. We find an

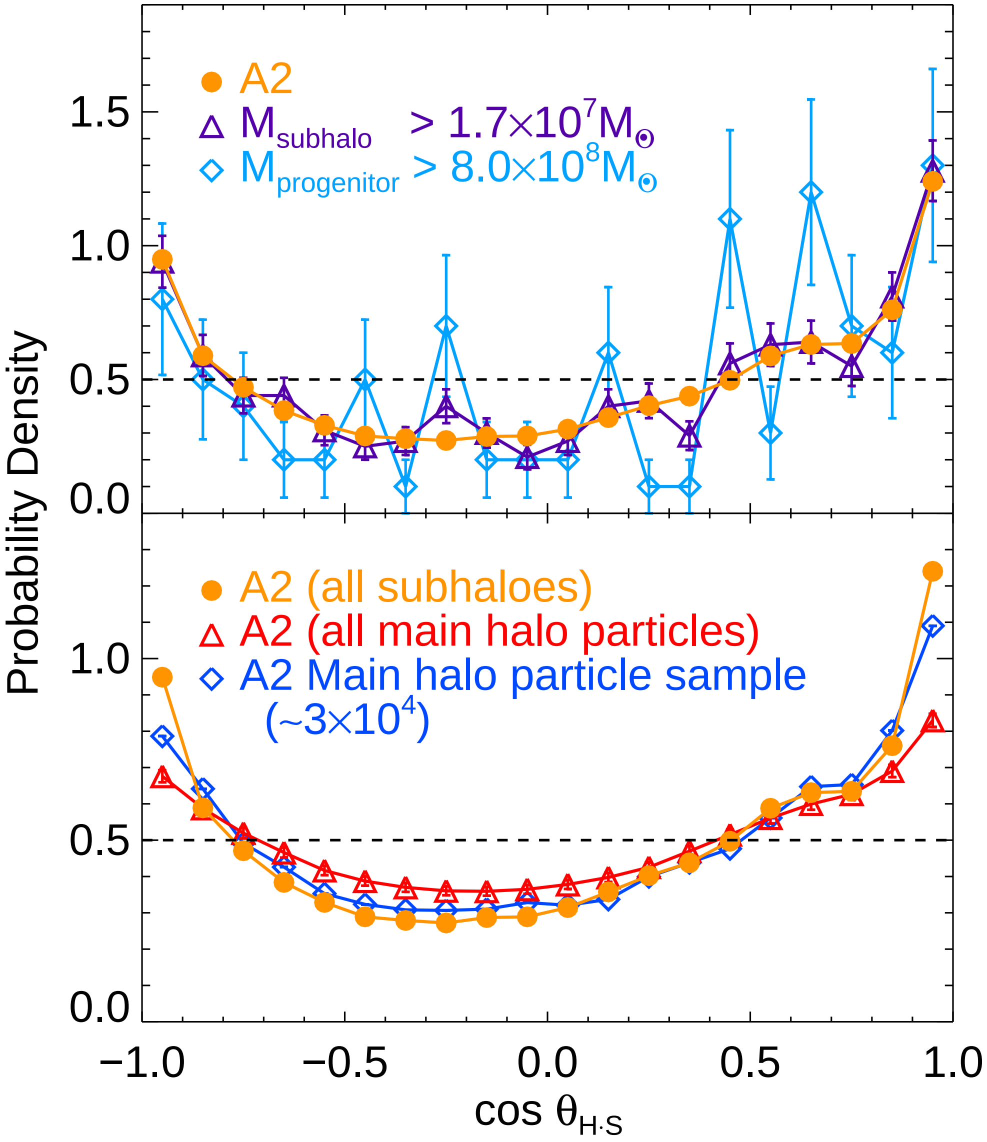

Figure 2.3: The distribution of cos $\theta_{\mathrm{H\cdot S}}$ for different populations. *Top panel:* comparison of the 1000 most massive subhaloes at $z = 0$ (purple) with the 100 subhaloes that have the most massive progenitors (light blue), and the entire population of Fig. 2.2 (orange). *Bottom panel:* comparison of the cos $\theta_{\mathrm{H\cdot S}}$ distribution for subhaloes with two populations of main halo particles: a sample of 3×10^4 selected to have the same radial distribution as the main halo (blue) and the full population (red).

antiparallel excess in three out of six of our haloes, whereas Warnick and Knebe (2006) only have one such halo out of their sample of nine. Adopting the same binning as Warnick and Knebe (2006) does not change our result. With such small halo samples it is unclear whether this particular result is consistent or inconsistent between the two studies.

To test if our results are robust to changes in resolution, we repeat this calculation for the five different resolution levels of the Aq-A halo (Fig. 2.2). We see that Aq-A1 together with Aq-A3, Aq-A4, and Aq-A5 has an angular momentum distribution broadly of the same form as Aq-A2, with increasing noise as the resolution decreases because of the smaller number of subhaloes. Each resolution level is dominated by a different subhalo mass; the minimum subhalo mass in Aq-A5 is $\sim 10^7 \mathrm{M}_{\odot}$, while in Aq-A1 it is three orders of magnitude smaller. We find a similar degree of convergence with numerical resolution for haloes Aq-B through to Aq-F.

In Fig. 2.3 we probe the orientation of the angular momentum vector of different populations. In the top panel, we compare the distribution for the 1000 largest subhaloes at the final redshift (particle number > 1222, equivalent to subhalo mass of $1.7 \times 10^7 \mathrm{M}_{\odot}$) with that the 100 subhaloes present at $z = 0$ that had the most massive progenitors and that of the entire halo population. The most massive progenitor is defined as the SUBFIND halo in the merger tree that contained the largest number of particles over the entire history of the simulation. This mass is very close to the mass that the subhalo had at the time it fell into the main halo. It is these subhaloes that are most likely to host satellite galaxies, according to Libeskind et al. (2009). Of the subhaloes that had the 100 largest progenitors, all bar 6 are among the top 1000 most massive subhaloes at redshift zero. The distributions of cos $\theta_{\mathrm{H \cdot S}}$ for all three populations of subhaloes are consistent within the errors.

To establish whether the angular momentum orientation of the subhalo population is special, in the lower panel of Fig. 2.3 we compare subhaloes in Aq-A2 with particles from the main halo. We create a special sample of halo particles with the same radial distribution as the subhaloes. This is made by first defining a set of about 30 radial bins between the halo centre and the virial radius. The halo subsample is produced by first noting how many subhaloes lie in a particular bin, and then randomly selecting the same number of halo particles from the that same bin. This is always possible as the number of halo particles in any bin exceeds the corresponding number of subhaloes. We compare this particle sample's distribution of cos $\theta_{\mathrm{H\cdot S}}$ with that for the Aq-A2 subhaloes and for the entire set of main halo particles. The three distributions are statistically inconsistent with each other. The subhalo population has a larger fraction of aligned and antialigned members, with the radially selected subsample being intermediate between the subhaloes and the halo particles as a whole. Although even the latter has a non-uniform distribution of angular momenta cosines, it is significantly flatter than that of other two populations. This suggests that the accretion mechanism that supplies subhaloes (of all masses) is somewhat different from the mechanism by which halo particles are accreted, or that the evolution of subhaloes differs from that of halo particles.

To investigate the orientation of the orbital spins in more detail, we plot the angular momentum vectors of each subhalo on an all-sky Mollweide projection, one for each halo at resolution L2. Each map displayed here was divided into ~ 45000 pixels, with angular width $\sim 1^{\circ}$, and smoothed with a Gaussian beam of FWHM 10° using Healpix routines (Górski et al., 2005). We identify the pixel with the highest density after smoothing, and call this the 'densest point vector'. The pre-smoothing maps for all six L2 haloes are displayed in Fig 2.4. The main halo spin vector is marked in red, its antipole in blue, and the densest point vector in green.

Aq-A2 exhibits the cleanest structure of all the haloes, with strong clustering around the pole and antipole, joined by two strands. Aq-B2 is, in contrast, characterised by irregular structures concentrated around regions distant from the main halo spin poles. All of the other haloes exhibit clustering around the main halo spin, with other, local, features apparent. The densest point vector position is always closer to the main halo spin than to its antipole. One may think of Figs. 2.1 to 2.3 as an integration around lines of equal angle from the red and blue circles. As noted above, we are particularly interested in those subhaloes that are most likely to host satellites, and so we repeat this plot for the 100 subhaloes with largest progenitors in Fig. 2.5.

As expected from Fig. 2.3, the 100 subhaloes with the largest progenitors trace the underlying structure of subhaloes in the map traced in Fig. 2.4. A few of them lie in regions where there are few subhaloes of any mass, and so we might expect to find satellite galaxies spatially removed from the disc-of-satellites for at least some portions of their orbits. The majority, however, lie within underlying structures. The subhaloes

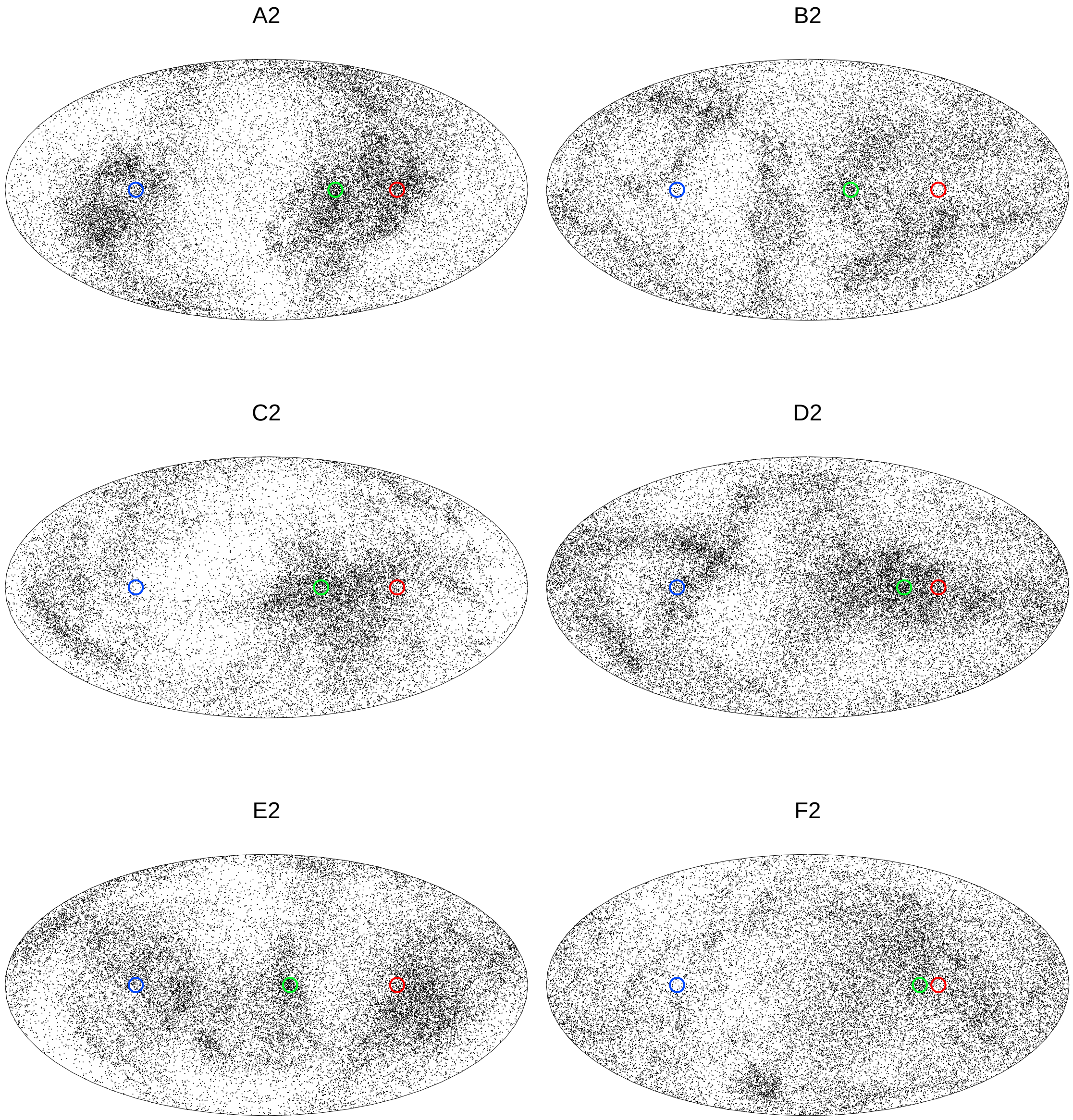

Figure 2.4: Mollweide projections of the directions of the angular momentum vectors of all subhaloes in the L2 simulations. The red circle shows the direction of the main halo spin, blue the main halo spin antipole, and green the densest collection of vectors after smoothing. The maps have been rotated such that all three circles lie on the equator, with the main halo spin and its antipole lying 90° either side of the centre and the green circle in between. Thus, a subhalo of $\theta_{\mathrm{H\cdot S}} = 0^\circ$ will map to the red circle, and one of $\theta_{\mathrm{H\cdot S}} = 90^\circ$ to either the plot boundary or a point on the north-south bisector.

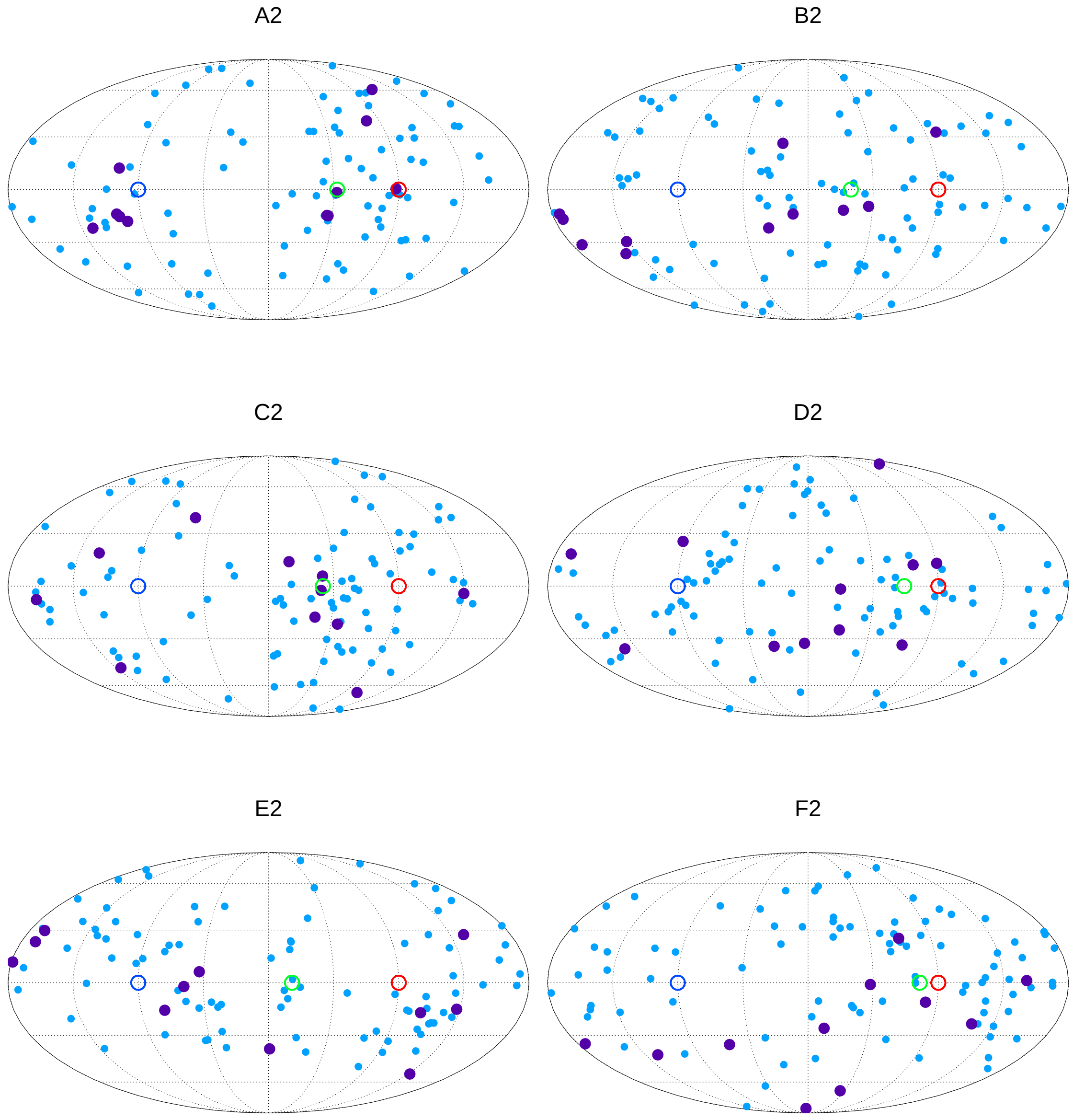

Figure 2.5: Mollweide projections of the directions of the angular momentum vectors of subhaloes with the largest progenitors in the L2 simulations. Subhaloes with top 100 progenitors are denoted in blue; the subset with the 11 largest progenitors are plotted in purple.

with the top 11 progenitors cluster in the same way as the rest of the top 100. Thus, we conclude that observed satellite galaxies should also exhibit coherent motion.

2.3.2 The origin of coherent rotation

The importance of filamentary accretion can be appreciated by examining the positions of the subhaloes at different snapshots in the simulation. In Fig. 2.6 we plot the positions of all the subhaloes present at $z = 0$, relative to the centre of the main halo in two projections. On the left, the main halo angular momentum vector points along the positive X-axis, so that the subhalo populations that have cos $\theta_{\mathrm{H \cdot S}} > 0.9$ (red) and cos $\theta_{\mathrm{H \cdot S}} < -0.9$ (blue) appear as an edge-on thick disc. On the right, the angular momentum vector points out of the plane of the page.

In Fig. 2.7 we investigate the origins of the different populations of subhaloes by plotting their positions in the initial conditions. No subhaloes have condensed at this early time, so we define the 'position' of each subhalo as the centre-of-mass of all the particles that will be members of that subhalo at redshift zero. Plotting the position of the most-bound particle rather than the centre-of-mass makes no difference to the appearance of the plot, and the plotting procedure followed is exactly the same as that used for Fig. 2.6.

All of the haloes that have an excess of near-antiparallel subhaloes in Fig. 2.1 show a delineation in the positions of the different subhalo populations. There is also a degree of segregation in Aq-C2, however we find no clear delineation for haloes Aq-B2 and Aq-F2. We can observe how these segregated initial positions evolve into the orbital configurations at the final time by examining snapshots of intermediate redshift. In the cases of haloes Aq-A and Aq-D, we find that, independent of resolution, the motion of interest of these delineated subhaloes occurs within the plane of the main halo spin (the panels A-R and D-R). This enables us to describe this motion simply with the schematic arrows shown in these panels in Fig. 2.7. In both of these haloes the near-parallel and near-antiparallel populations collapse to form filaments in their segregated regions. Crucially these filaments are not straight, and the subhaloes follow curved paths into the main halo as shown by their same-colour arrows. 'Red' (near-parallel) subhaloes will therefore enter the virial radius with an anti-clockwise orbit around the plot centre, whereas the 'blue' will adopt a clockwise orbit. In Aq-D the 'red' and 'blue' filaments are separate

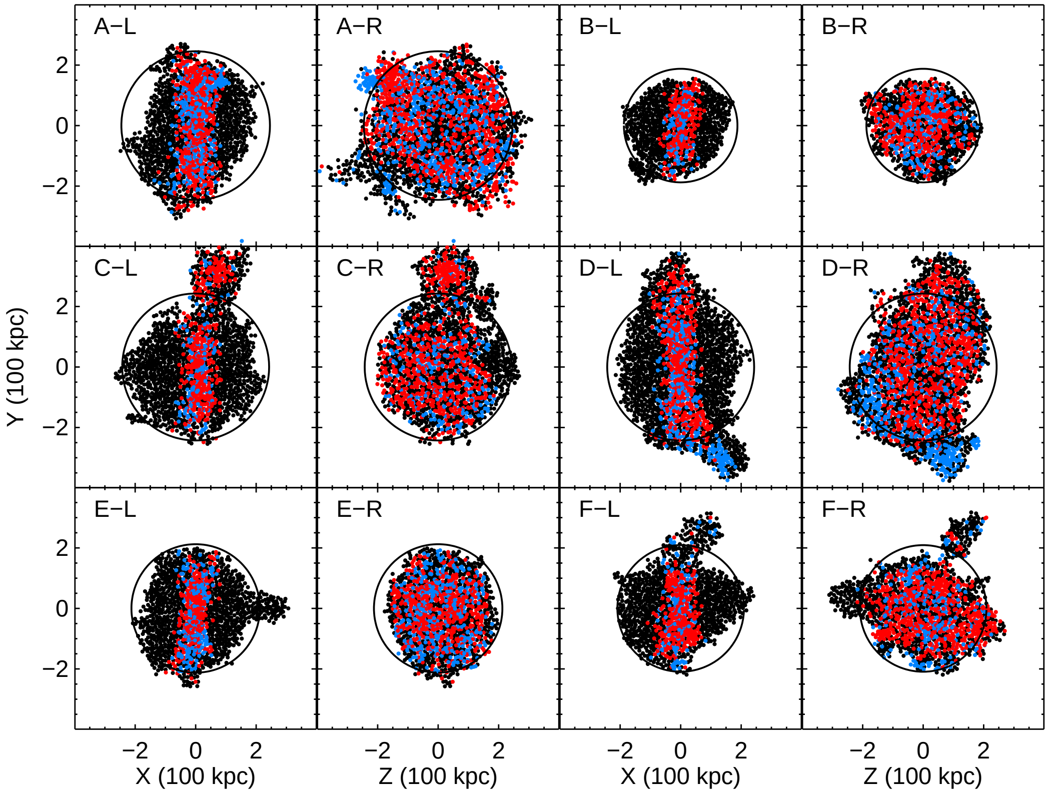

Figure 2.6: $X - Y$ positions for subhaloes associated with the largest FOF group at $z = 0$ in two projections. Subhaloes with cos $\theta_{\rm H\cdot S} > 0.9$ are indicated in red and those with cos $\theta_{\rm H\cdot S} < -0.9$ in blue. All other subhaloes are shown in black. The black circle marks the virial radius, r_{200}. *Left panels (i.e. L):* the X axis points in the direction of the main halo spin, so those subhaloes with orbit vectors parallel and antiparallel to the main halo spin appear as a band parallel to the Y axis. *Right Panel (R):* looking down the X axis, so the main halo is spinning anticlockwise. The red and blue points are plotted in a random order on top of the black.

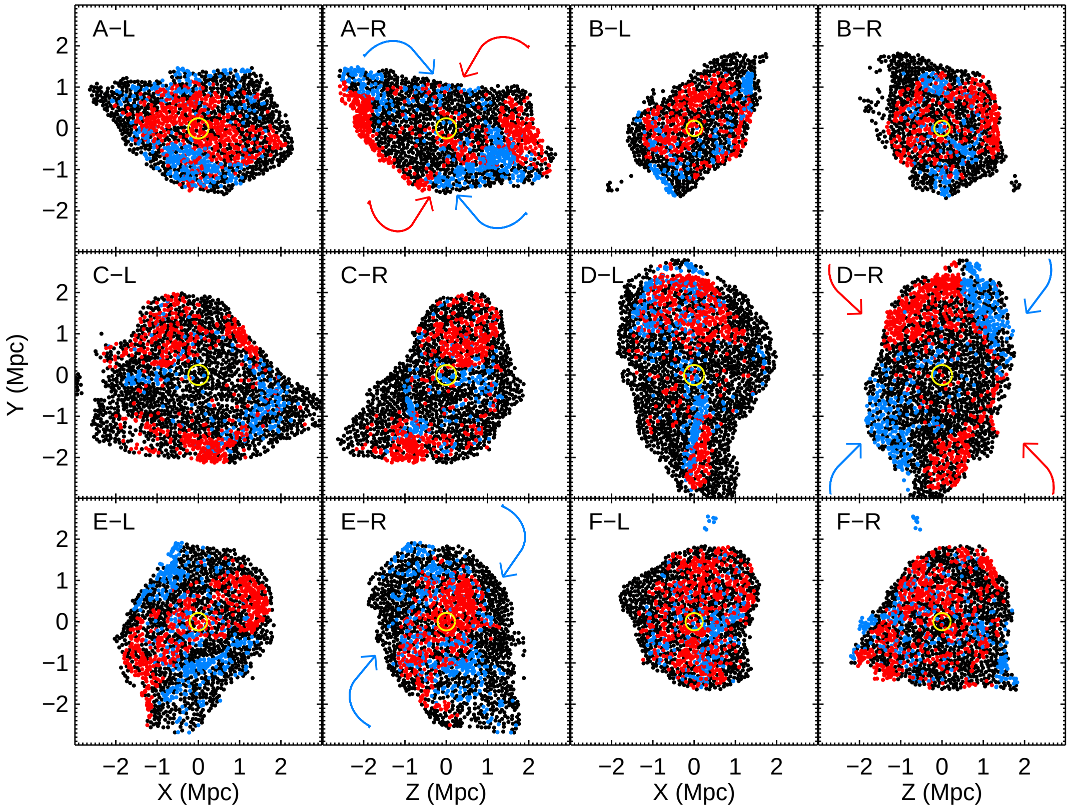

Figure 2.7: $X - Y$ comoving positions at $z = 127$ of the centre of mass of the particles that end up in each subhalo at $z = 0$. The coordinates are as in Fig. 2.6, with the main halo spin at $z = 0$ still determining the projections. The final virial radius is indicated in yellow. As stated in the text, the haloes Aq-A2 and Aq-D2 are found to accrete their 'red' and 'blue' subhaloes in the plane of the main halo spin, and so we have added coloured arrows to the A-R and D-R panels to illustrate schematically the accretion paths for the different subhalo populations. The 'blue' subhaloes of Aq-E2 exhibit similar behaviour, and so we have also included arrows to indicate their motion in E-R.

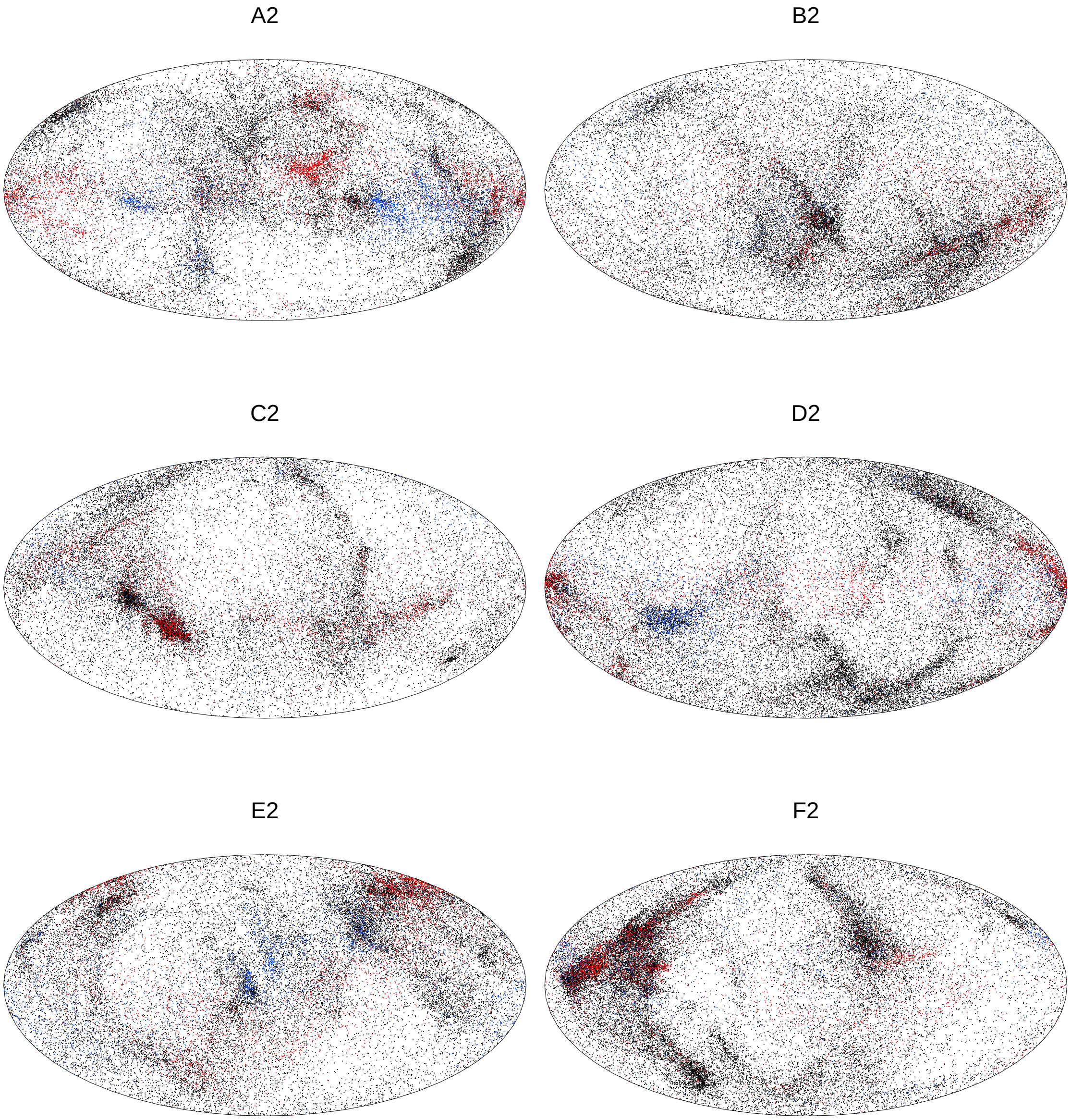

Figure 2.8: Mollweide projections of the position at which each subhalo enters the main halo. Subhaloes that end up in parallel spin orbits are shown in red, those that end up in antiparallel spin orbits in blue, and those with intermediate orbits in black. The main halo spin points towards the north pole of each projection.

entities, but in Aq-A they lie very close together and give the appearance of one filament fed at each end by two 'strands'. One of these strands then supplies the near-parallel subhaloes and the other the near-antiparallel.

Aq-E near-antiparallel subhaloes are also accreted through a pair of curved filaments approximately in the plane of the final main halo spin, and so we illustrate the motion of these subhaloes with arrows in Fig. 2.7 panel E-R. By contrast, the accretion of the red subhaloes is more complex and involves motion at a significant angle to the plane of the main halo spin, and for this reason we do not draw the corresponding red arrows. In Aq-C some of the 'red' subhaloes do accrete in a filament, but a large proportion end up in the large lump visible at the top of Fig. 2.6 panels C-L and C-R. No coherent inflow pattern is apparent for the small population of 'blue' subhaloes.

We can describe the accretion geometry further by determining where each subhalo enters the main halo. We find the redshift at which each subhalo attains its highest mass (taken to indicate the time when it falls into the virial radius of the main halo) and thus determine its infall position relative to the main halo centre. The results are plotted in Fig. 2.8, which is oriented such that the main halo spin points towards the north pole of each projection. We can see that, independent of resolution, the subhalo populations that end up in parallel and antiparallel spin orbits in Aq-A, Aq-D, and Aq-E originate from preferential directions as expected from our visual examination. A majority of subhaloes in Aq-D and Aq-A accrete close to the equator, also as expected, whilst Aq-E acquires a significant proportion of its parallel orbit subhaloes from a patch of sky close to the main halo pole. Any demarcation for haloes Aq-B, Aq-C, and Aq-F is less clear, suggesting that filaments played a lesser role in their accretion history.

2.4 Conclusions

In this Chapter we have characterized the distribution of subhalo orbits in the Aquarius simulations of CDM galactic haloes and attempted to explain the mechanisms that give rise to them. We find that the complex accretion patterns that build up a halo result in different configurations of subhalo orbits, none of which is close to isotropic. Some are structured in a symmetric way (Aq-A) relative to the spin poles, while others show no strong pattern (Aq-B). In all six haloes we find a large subhalo population that has coherent rotation aligned with the spin of the main halo, in agreement with the results of Libeskind et al. (2009). In three cases there is, in addition, a subhalo population that counter-rotates relative to the main halo. We trace this rather unexpected arrangement back to the filamentary nature of subhalo accretion. If galaxies tend to rotate in the same direction as their parent halo (Bailin et al., 2005; Bailin and Steinmetz, 2005; Bett et al., 2010), our results show that it is possible to generate populations of retrograde satellites. Such a population of retrograde satellites appears to be present in NGC 5084 (Carignan et al., 1997) whereas a population of prograde satellites appears to be present in the Milky Way (Metz et al., 2008); Hwang and Park (2010) find equal proportions of prograde and retrograde satellites across a sample of 215 systems.

Halo Aq-A has a particularly concise formation history. This halo forms from a filament that collapses at early times and is fed by two strands at either end. A large fraction of the subhaloes that survive to the present pass though these strands, and are propelled into either a prograde or retrograde orbit depending on the strand in which they originated. Aq-D has a similar formation history and outcome, whereas Aq-E shows that it is possible to end up with a similar orbital arrangement by a different, more complex path. Coherent rotation is exhibited by the entire population of subhaloes, not just those with the most massive progenitors which according, for example, to Libeskind et al. (2005) are the most likely to host visible satellites.

Our analysis has implications for the expected bulk kinematics of satellite galaxies which may be probed in future galaxy surveys. We expect a variety of orbital configurations reflecting the variety of halo formation histories. Quasi-planar distributions of coherently rotating satellites should be commonplace, most rotating in the same direction as the halo (and, by implication, the main galaxy) but some in the opposite direction as found by Hwang and Park (2010).

Chapter 3

Addressing the 'Too Big to Fail' problem with WDM

3.1 Introduction

Measurements of temperature anisotropies in the microwave background radiation (e.g. Komatsu et al., 2011), of galaxy clustering on large scales (e.g. Cole et al., 2005), and of the currently accelerated expansion of the Universe (e.g Clocchiatti et al., 2006; Guy et al., 2010) have confirmed the "Lambda cold dark matter" (ΛCDM) model, first explored theoretically 25 years ago (Davis et al., 1985), as the standard model of cosmogony. These observations probe a large range of scales, from ~ 1Gpc to ~ 10Mpc. On smaller scales, where the distribution of dark matter is strongly nonlinear, observational tests of the model are more complicated because of the complexity added by galaxy formation processes. However, it is precisely on these scales that the nature of the dark matter may be most clearly manifest. For example, if the dark matter is made of warm, rather than cold particles, free streaming in the early universe would have erased primordial fluctuations below a scale that depends on the mass of the dark matter particle but could be of order $10^9 - 10^{10}\mathrm{M}_\odot$. These mass scales correspond to dwarf galaxies and so, in principle, the abundance and properties of dwarf galaxies could encode information about the nature of the dark matter.

The validity of the ΛCDM model on galactic and subgalactic scales has been a subject of debate for many years. Initially Klypin et al. (1999) and Moore et al. (1999) pointed out a large discrepancy between the number of dark matter substructures, or subhaloes, that survive inside a galactic halo and the number of satellites that are observed around the Milky Way. This so-called "satellite problem" is often interpreted as indicating that the model requires most of the subhaloes to contain no visible satellite. This aspect of the problem, however, is readily solved by invoking the known physics of galaxy formation, particularly early reionization of the intergalactic medium and supernovae feedback, which inevitably inhibit the formation of stars in small mass haloes. Detailed models that reconcile theory and observations in this way date back to the early 2000s (Bullock et al., 2000; Benson et al., 2002; Somerville, 2002).

The paucity of observed bright satellites, however, is only one aspect of the satellite problem. As already emphasized by Klypin et al. (1999) and Moore et al. (1999), there is a problem not only with the abundance of satellites, but also with their distribution of circular velocities. In a halo like that of the Milky Way, the ΛCDM model predicts the existence of several subhaloes with maximum circular velocities, $V_{\rm max}$[1], in excess of ~ 40 kms^{-1} . Using the high-resolution simulations of galactic haloes of the Aquarius project (Springel et al., 2008a), Strigari et al. (2010) have recently demonstrated that it is possible to find ΛCDM subhaloes that accurately match the observed stellar kinematics of the five well-studied satellites of the Milky Way. The best fits, however, invariably have $V_{\rm max}\lesssim 40$ kms^{-1} . (The Strigari et al. sample excludes the LMC and SMC which reside in more massive haloes, and Sagittarius which is currently being disrupted.)

The discrepancy between the predicted and inferred distributions of $V_{\rm max}$ values has recently been highlighted by Boylan-Kolchin et al. (2011). Using also the Aquarius haloes, as well as the Via Lactea simulations (Madau et al., 2008), they show explicitly that the simulated haloes typically contain a few subhaloes which are too massive and too dense (as indicated by their value of $V_{\rm max}/r_{\rm max}$) to host any of the observed satellites. If such objects existed in the Milky Way, they would have to be empty of stars despite their mass. This seems very unlikely so, unless the Milky Way is atypical, there is an apparent discrepancy between model and observations.

That the Milky Way is not typical of isolated galaxies of similar luminosity and colour has recently been established from SDSS data. Liu et al. (2011) have shown that only 3.5% of such galaxies have 2 satellites as bright as the Magellanic Clouds, while Guo et al. (2011) have shown that the luminosity function of the bright ($M_V < -14$) Milky Way satellites has about twice the amplitude of the mean for similar galaxies (see also Lares et al., 2011). While these measurements show that the Milky Way is not an average galaxy, it is not at present possible to compare the distribution of $V_{\rm max}$ of its satellites with that of similar galaxies directly. However, an indirect probe of this distribution can be constructed by combining N-body simulations with a subhalo abundance matching procedure (Busha et al., 2010b).

---

[1] The circular velocity is given by $V = (GM(<r)/r)^{1/2}$, where M is the mass enclosed within radius r and G is the universal gravitational constant; the value of r at which the maximum of this function, $V_{\rm max}$, occurs is denoted by $r_{\rm max}$

In this Chapter we explore whether an alternative hypothesis for the nature of the dark matter, a warm rather than a cold particle, can provide a better match to the inferred distribution of satellite circular velocities or masses. Specifically, we test a model in which the dark matter is one of the particles predicted by the "neutrino minimal standard model (νMSM)" of Asaka and Shaposhnikov (2005) and Boyarsky et al. (2009c). In this model there is a triplet of sterile neutrinos, the lightest of which could become non-relativistic at a redshift of $\sim 10^6$, have a mass of $\sim 2{\rm keV}$, and behave as warm dark matter (WDM). This model is consistent with astrophysical and particle physics data, including constraints on neutrino masses from the Lyman-α forest (Boyarsky et al., 2009a).

To investigate this WDM model we have resimulated one of the Aquarius N-body haloes (Aq-A) with the power spectrum suppressed at small scales, as expected in the WDM case. N-body simulations of galactic and cluster WDM haloes were first carried out in the early 2000s (Colín et al., 2000; Bode et al., 2001; Knebe et al., 2002). These studies found that fewer subhaloes form than in the CDM case and that these tend to be less concentrated than their CDM counterparts. Qualitatively, we find similar results but the conclusions of these early simulations are difficult to interpret because, as we shall see later, the sharp cutoff in the power spectrum gives rise to the formation of a large number of artificial haloes that are purely numerical in origin (Wang and White, 2007). More recently, Macciò et al. (2010) carried out new simulations of WDM models and found that the luminosity function of satellites can be reproduced in these models just as well as it can in the CDM case.

Our simulations have orders of magnitude higher resolution than previous ones, enough to investigate reliably the inner structure of the galactic subhaloes that are potential hosts of the dwarf satellites. Furthermore, we carry out convergence tests of our results and develop a method for distinguishing genuine WDM haloes from the spuri-

Name	$m_{\rm p}$ [M$_\odot$]	r_{200} [kpc]	M_{200} [M$_\odot$]	$N_{\rm s}$
Aq-A2	1.370×10^4	245.88	1.842×10^{12}	30177
Aq-A3	4.911×10^4	245.64	1.836×10^{12}	9489
Aq-AW2	1.370×10^4	242.87	1.775×10^{12}	689
Aq-AW3	4.911×10^4	242.98	1.778×10^{12}	338
Aq-AW4	3.929×10^5	242.90	1.776×10^{12}	126

Table 3.1: Basic parameters of the simulations analysed in this Chapter. The top two simulations are taken from the Aquarius sample of CDM dark matter haloes published in Springel et al. (2008a). The simulations are of a single halo, Aq-A, at different numerical resolutions. The bottom three are warm dark matter counterparts to the CDM simulations, as described in the main text. The second to fifth columns give the particle mass ($m_{\rm p}$), the radius of the sphere of density 200 times the critical density (r_{200}), the halo mass within r_{200} (M_{200}) and the number of subhaloes within the main halo ($N_{\rm s}$). The smallest subhaloes, determined by SUBFIND, contain 20 particles.

ous objects that inevitably form in simulations of this kind. We describe our simulations in Section 3.2, present our results in Section 3.3, and conclude in Section 3.4.

3.2 The simulations

To compare the properties of subhaloes in Milky Way mass haloes in CDM and WDM universes, we have assembled a sample of five high resolution simulations of galactic mass haloes. All the simulations have the same basic cosmological parameters: in units of the critical density, a total matter density, $\Omega_m = 0.25$ and a cosmological constant, $\Omega_\Lambda = 0.75$. The linear power spectrum has a spectral index $n_s = 1$ and is normalised to give $\sigma_8 = 0.9$, with $H_0 = 100h\mathrm{kms}^{-1}\mathrm{Mpc}^{-1} = 73\mathrm{kms}^{-1}\mathrm{Mpc}^{-1}$ (Springel et al., 2008a). [2]

We have taken two simulations from the Aquarius project described in Springel et al.

---

[2] Although this set of parameters is discrepant at about the 3σ level with the latest constraints from microwave background and large-scale structure data (Komatsu et al., 2011), particularly with the values of σ_8 and n_s, the differences are not important for our purposes. For example, Boylan-Kolchin et al. (2011) show that the structure of Aquarius subhaloes is statistically similar to that of subhaloes in the Via Lactea simulations which assume a value of $\sigma_8 = 0.74$, lower than that of Komatsu et al. (2011), and a spectral index of 0.95.

(2008a), both of the same halo, Aq-A, but of different resolution, corresponding to levels 2 and 3 in the notation of Springel et al. (2008a). The higher resolution, level 2, simulation has more than a hundred million particles within r_{200}, the radius of a sphere about the halo centre, encompassing a mean density of 200 times the critical density. The level 3 simulation has 3.6 times fewer particles. In both cases, the mass of the halo within r_{200} is about $1.8 \times 10^{12}\,M_{\odot}$, which is consistent with the estimated mass of the Milky Way (Li and White, 2008; Xue et al., 2008; Gnedin et al., 2010). The basic properties of these haloes are given at the top of Table 3.1. Substructures were identified using the SUBFIND algorithm (Springel et al., 2001b) to find gravitationally bound subhaloes within them.

We created three WDM counterparts to the CDM haloes by running new simulations using the same code and numerical parameters as Springel et al. (2008a) but with WDM initial conditions. The WDM initial conditions were created keeping the same phases and the same unperturbed particle positions as in the CDM case, but using a WDM matter power spectrum instead to scale the amplitudes of the fluctuations. The linear matter power spectrum for both the CDM and WDM simulations is shown in Fig. 3.1 with solid lines adopting an arbitrary normalisation at large scales.

The warm dark matter power spectrum has a strong cut off at high wavenumbers due to the free streaming of the warm dark matter particles. In an unperturbed universe at the present day the typical velocities of warm dark matter particles are only a few tens of metres per second. This implies that the particles ceased to be relativistic after a redshift of $z \sim 10^7$, well before the end of the radiation-dominated era, as suggested by the word 'warm'. Fig. 3.2 illustrates the free streaming of a typical warm dark matter particle over cosmic time. The area under the curve is the comoving distance traveled. It is evident that the warm dark matter particle travels the greatest comoving distance during the radiation-dominated era after it has become nonrelativistic (Bode et al., 2001). Over the duration of the N-body simulation, which starts at $z = 127$, a particle typically travels a distance of around $14\,\mathrm{kpc}$, which is small compared to the total distance from early times of $400\,\mathrm{kpc}$. For comparison, the mean interparticle separation for the high resolution region in our highest resolution simulation is $7.4\,\mathrm{kpc}$, similar to the free-streaming distance traveled by the particles after $z = 127$. This means that the effects of streaming during the simulation are small, and only affect scales that are barely resolved in our simulations. For this reason we chose to set the particle velocities in the same way as in the CDM case, where the particle velocity is a function of the unperturbed comoving position of a particle and is determined solely by the matter fluctuations.

The WDM matter power spectrum we assume has a shape characteristic of a "thermal relic" (Bode et al., 2001) with a mass of ~ 1.4keV (the most extreme model used in Chapter 4). However, our WDM matter power spectrum is also an excellent fit for scales below $k \sim 10$ h/Mpc to the matter power spectrum of the M2L25 model of Boyarsky et al. (2009b), which is shown as a dashed line in Fig. 3.1. At $k = 10$ h/Mpc the power in both WDM curves is a factor three below that of CDM and falls away very rapidly beyond here in both models. The M2L25 model corresponds to a *resonantly produced* $\sim 2\mathrm{keV}$ sterile neutrino with a highly non-equilibrium spectrum of primordial velocities. The model is only just consistent with astrophysical constraints (Boyarsky et al., 2009a) and so maximizes the differences between the substructures in the cold and warm dark matter haloes, both in their internal structure and in their abundance.

For wavenumbers below the peak at $4.5h\mathrm{Mpc}^{-1}$ the linear warm dark matter power spectrum is well approximated by the product of the linear cold dark matter power spectrum times the square of the Fourier transform of a spherical top-hat filter of unit amplitude and radius $320\ \mathrm{kpc}$, or equivalently, containing a mass of $5 \times 10^{9}\mathrm{M}_{\odot}$ at the mean density.

Images of the CDM and WDM haloes are shown in Fig. 3.3. As shown in Table 3.1, the mass of the main halo in the WDM simulation is very similar to that of the CDM halo, just a few per cent lighter. However, the number of substructures in the WDM case is much lower, reflecting the fact that the small scale power in these simulations is greatly reduced. Some of the largest subhaloes can be matched by eye in the images of the two simulations.

Springel et al. (2008a) showed that it is possible to make precise matches between substructures at different resolutions for the Aq-A halo, allowing the numerical convergence of properties of substructures to be checked for individual substructures. For this Chapter, we have found matches between subhaloes in the Aq-AW2, Aq-AW3, and Aq-AW4 simulations. We make these matches at the epoch when the subhaloes first have a mass which is more than half the mass they have at the time when they first infall into the main halo (which is very close to the maximum mass they ever attain). At this epoch it is relatively easy to match the largest substructures in these three simulations as the

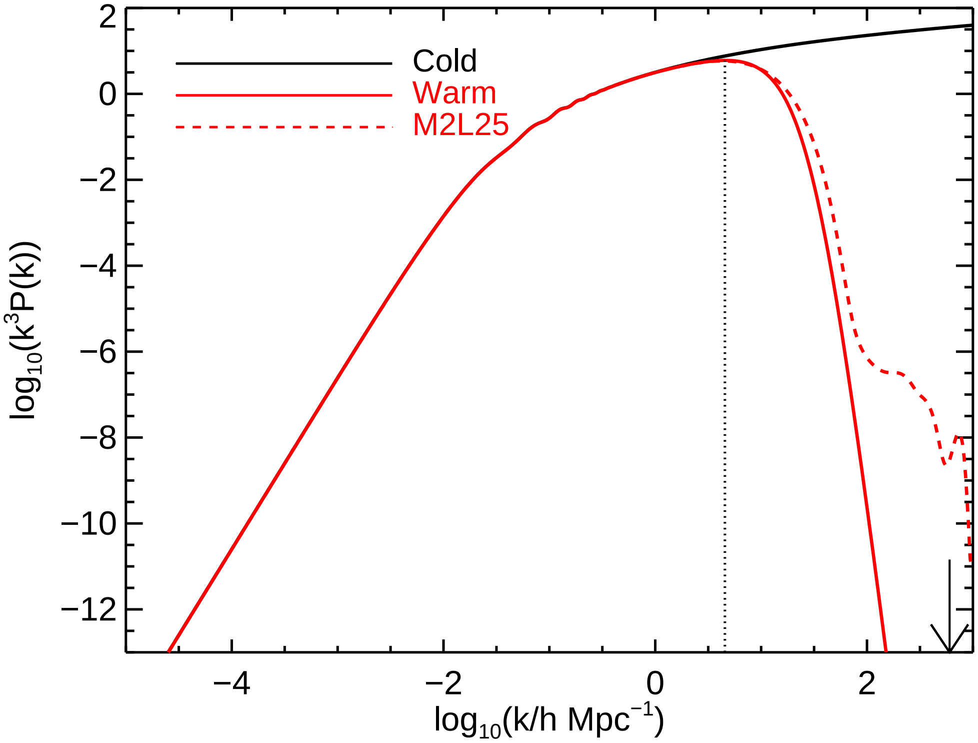

Figure 3.1: The solid lines show the linear power spectra (from CMBFAST; Seljak and Zaldarriaga, 1996) used for the two simulations. Black is the original, CDM Aq-A spectrum, and red is that of Aq-AW. The vertical dashed line marks the peak of the WDM spectrum peak. The arrow marks the Nyquist frequency of the level 2 simulations. The dashed red curve corresponds to the M2L25 model of (Boyarsky et al., 2009b) which is almost identical to the solid red curve for scales below $k \sim 10$ h/Mpc.

corresponding objects have very similar positions, velocities and masses.

The number of subhaloes that can be matched between the two WDM simulations is much smaller than that between the corresponding CDM simulations, and is also a much smaller fraction of the total number of subhaloes identified by SUBFIND. The majority of substructures identified in the WDM simulations form through fragmentation of the sharply delineated filaments characteristic of WDM simulations and do not have counterparts in the simulations of different resolution. The same phenomenon is seen in hot dark matter simulations and is numerical in origin, occurring along the filaments on a scale matching the interparticle separation (Wang and White, 2007). This artificial fragmentation is apparent in Fig. 3.3.

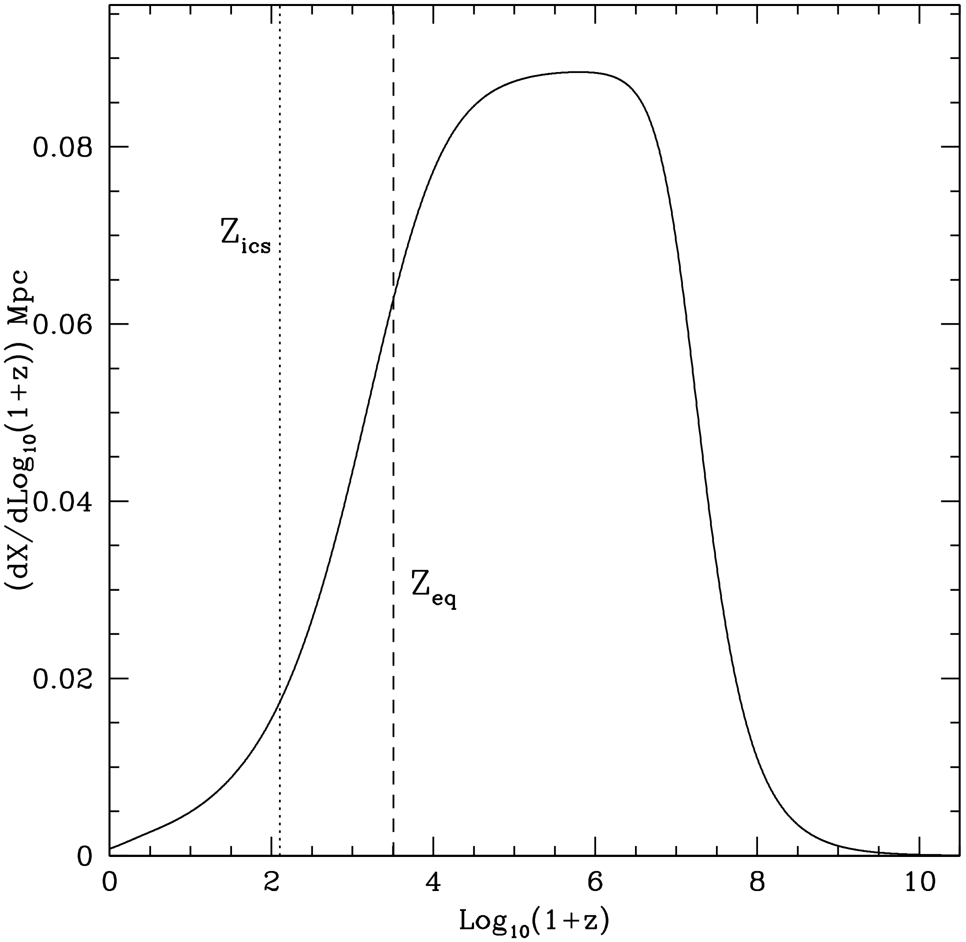

Figure 3.2: The free streaming comoving distance traveled per log interval of $1+z$, where z is redshift, for a warm dark matter particle with a fiducial velocity of $24\ \mathrm{m\ s^{-1}}$ at the present day. The dashed vertical line marks the redshift of matter-radiation equality. The dotted vertical line indicates the start redshift of the WDM simulations.

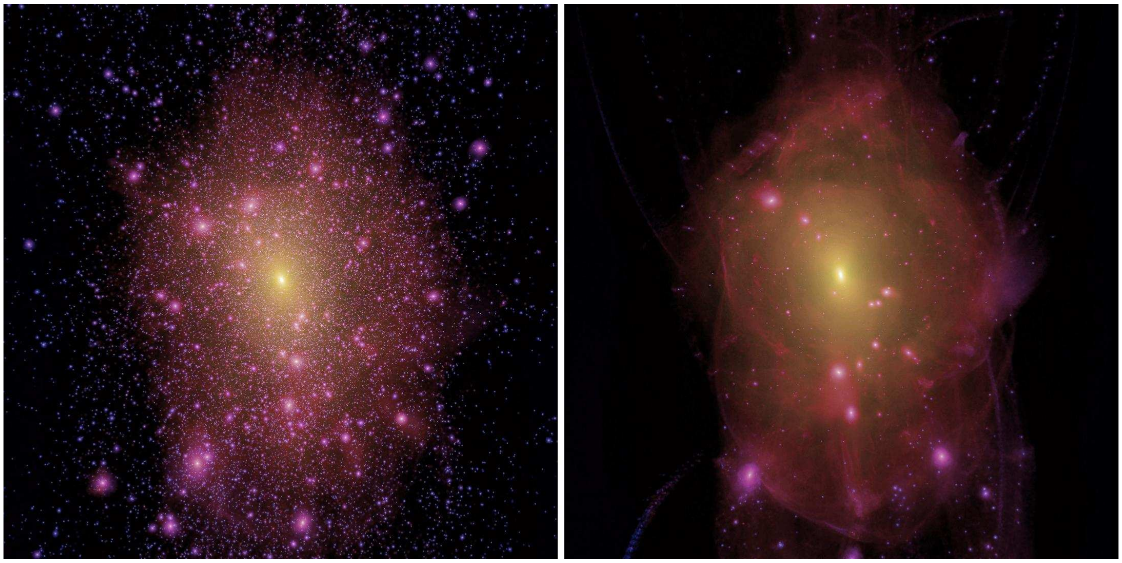

Figure 3.3: Images of the CDM (left) and WDM (right) level 2 haloes at $z = 0$. Intensity indicates density, and hue velocity dispersion, ranging from blue (low velocity dispersion) to yellow (high velocity dispersion). Each box is 1.5 Mpc on a side. Note the sharp caustics visible at large radii in the WDM image, several of which are also present, although less well defined, in the CDM case.

We will present a detailed description of subhalo matching in Chapter 4 but, in essence, we have found that matching subhaloes works best when comparing the Lagrangian regions of the initial conditions from which the subhaloes form, rather than the subhaloes themselves. We use a sample of the particles present in a subhalo at the epoch when it had half of the mass at infall to define the Lagrangian region from which it formed. We have devised a quantitative measure of how well the Lagrangian regions of the substructures overlap between the simulations of different resolution, and select as genuine only those subhaloes with strong matches between all three resolutions. We find that these criteria identify a sample of fifteen relatively massive subhaloes with mass at infall greater than $2 \times 10^9 M_{\odot}$, together with a few more subhaloes with infall mass below $10^9\mathrm{M}_{\odot}$. This sample of fifteen subhaloes includes all of the subhaloes with infall masses greater $10^9\mathrm{M}_{\odot}$.

We have also found that the shapes of the Lagrangian regions of spurious haloes in our WDM simulations are typically very aspherical. We have therefore devised a second measure based on sphericity as an independent way to reject spurious haloes. All fifteen of the massive subhaloes identified by the first criterion pass our shape test, but all but one subhalo with an infall mass below $10^9 \mathrm{M}_\odot$ are excluded. For the purposes of this Chapter we need only the 12 most massive subhaloes at infall to make comparisons with the Milky Way satellites.

For both our WDM and CDM catalogues, we select a sample made up of the 12 most massive subhaloes at infall found today within 300 kpc of the main halo centre. In the Aq-AW2 simulation these subhaloes are resolved with between about 2 and 0.23 million particles at their maximum mass. We use the particle nearest the centre of the gravitational potential to define the centre of each subhalo and hence determine the values of $V_{\max}$ and $r_{\max}$ defined in Section 1.

3.3 Results

In this section, we study the central masses of the substructures found within 300 kpc of the centres of the CDM and WDM Milky Way-like haloes. These results are compared with the masses within the half-light radii, inferred by Walker et al. (2009, 2010) and Wolf et al. (2010) from kinematic measurements, for the 9 bright ($L_V > 10^5 L_\odot$) Milky Way dwarf spheroidal galaxies.

Following the study by Boylan-Kolchin et al. (2011), in Fig. 3.4 we plot the correlation between $V_{\max}$ and $r_{\max}$ for the subhaloes in Aq-AW2 and Aq-A2 that lie within 300kpc of the centre of the main halo. Only those WDM subhaloes selected using our matching scheme are included, whereas all Aq-A2 subhaloes are shown. The CDM subhaloes are a subset of those shown in Fig. 2 of Boylan-Kolchin et al. (2011), and show $V_{\max}$ values that are typically ~ 50 per cent larger than those of WDM haloes with a similar $r_{\max}$. By assuming that the mass density in the subhaloes containing the observed dwarf spheroidals follows an NFW profile (Navarro et al., 1996c, 1997), Boylan-Kolchin et al. (2011) found the locus of possible $(r_{\max}, V_{\max})$ pairs that are consistent with the observed half-light radii and their enclosed masses. This is represented by the shaded region in Fig. 3.4. As Boylan-Kolchin et al. (2011) observed with their larger sample, several of the largest CDM subhaloes have higher maximum circular velocities than appears to be the case for the Milky Way bright dwarf spheroidals. By contrast, the largest WDM subhaloes are consistent with the Milky Way data.

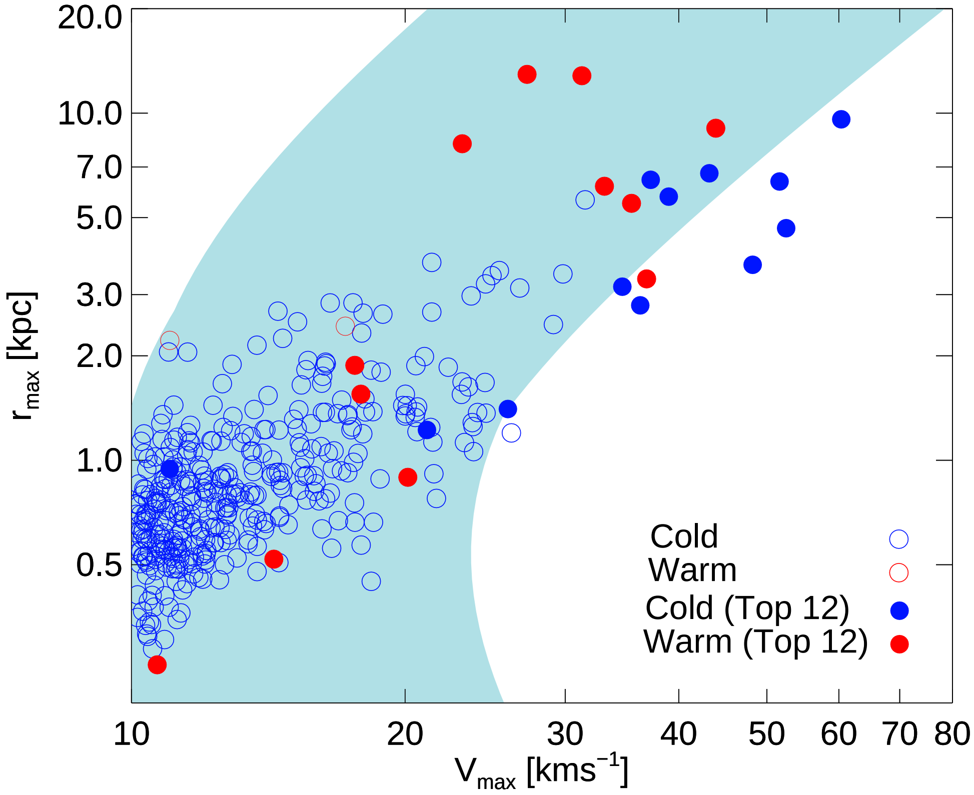

Figure 3.4: The correlation between subhalo maximum circular velocity and the radius at which this maximum occurs. Subhaloes lying within 300kpc of the main halo centre are included. The 12 CDM and WDM subhaloes with the most massive progenitors are shown as blue and red filled circles respectively; the remaining subhaloes are shown as empty circles. The shaded area represents the 2σ confidence region for possible hosts of the 9 bright Milky Way dwarf spheroidals determined by Boylan-Kolchin et al. (2011).

Rather than assuming a functional form for the mass density profile in the observed subhaloes, a more direct approach is to compare the observed masses within the half-light radii of the dwarf spheroidals with the masses within the same radii in the simulated subhaloes. To provide a fair comparison we must choose the simulated subhaloes that are most likely to correspond to those that host the 9 bright dwarf spheroidals in the Milky Way. As stripping of subhaloes preferentially removes dark matter relative to the more centrally concentrated stellar component, we choose to associate final satellite luminosity with the maximum progenitor mass for each surviving subhalo. This is essentially the mass of the object as it falls into the main halo. The smallest subhalo in each of our samples has an infall mass of $3.2 \times 10^9 \mathrm{M}_\odot$ in the WDM case, and $6.0 \times 10^9 \mathrm{M}_\odot$ in

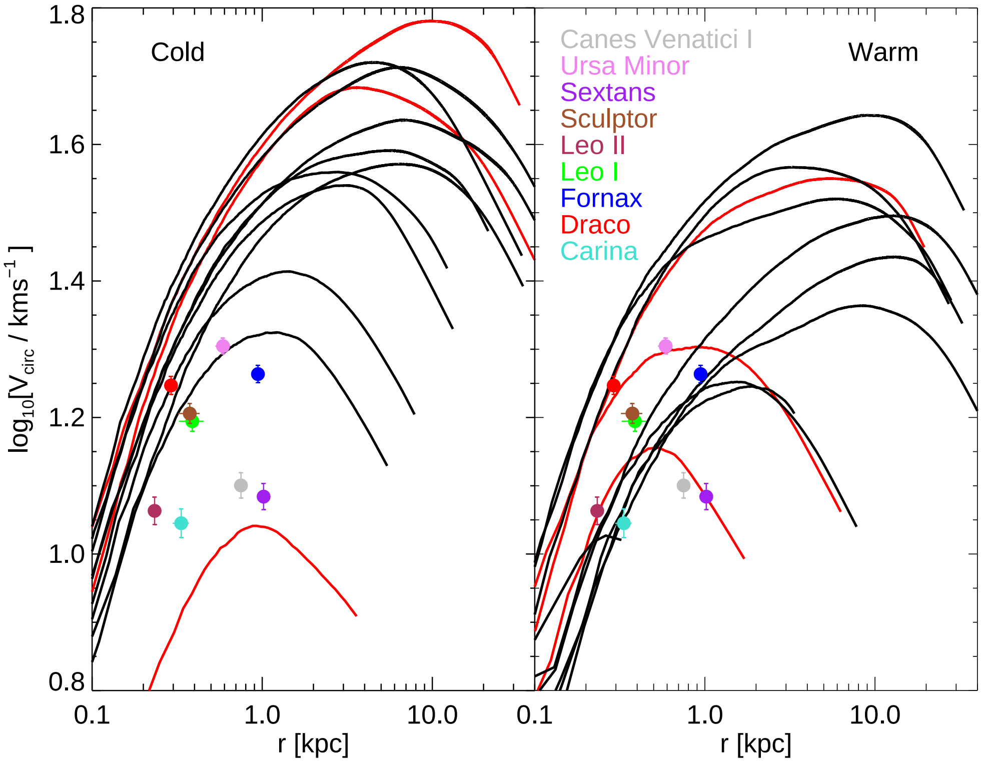

Figure 3.5: Circular velocity curves for the 12 CDM (left) and WDM (right) subhaloes that had the most massive progenitors. The 3 red curves represent subhaloes with the most massive progenitors, which could correspond to those currently hosting counterparts of the Large and Small Magellanic Clouds and the Sagittarius dwarf. The 9 black curves might more fairly be compared with the data for the 9 bright dwarf spheroidal galaxies of the Milky Way considered by Wolf et al. (2010). Deprojected half-light radii and their corresponding half-light masses, as determined by Wolf et al. (2010) from line-of-sight velocity measurements, are used to derive the half-light circular velocities of each dwarf spheroidal. These velocities and radii are shown as coloured points. The legend indicates the colour coding of the different galaxies.

the CDM case.

The Large and Small Magellanic Clouds and the Sagittarius dwarf are all more luminous than the 9 dwarf spheroidals considered by Boylan-Kolchin et al. (2011) and by us. As noted above, the Milky Way is exceptional in hosting galaxies as bright as the Magellanic Clouds, while Sagittarius is in the process of being disrupted so its current mass is difficult to estimate. Boylan-Kolchin et al. hypothesize that these three galaxies all have values of $V_{\rm max} > 60{\rm kms}^{-1}$ at infall and exclude simulated subhaloes that have these values at infall as well as $V_{\rm max} > 40{\rm kms}^{-1}$ at the present day from their analysis. In what follows, we retain all subhaloes but, where appropriate, we highlight those that might host large satellites akin to the Magellanic Clouds and Sagittarius.

The circular velocity curves at $z = 0$ for the 12 subhaloes which had the most massive progenitors at infall are shown in Fig. 3.5 for both WDM and CDM. The circular velocities within the half-light radius of the 9 satellites measured by Wolf et al. (2010) are also plotted as symbols. Leo-II has the smallest half-light radius, $\sim$ 200pc. To compare the satellite data with the simulations we must first check the convergence of the simulated subhalo masses within at least this radius. We find that the median of the ratio of the mass within 200pc in the Aq-W2 and Aq-W3 simulations is $W2/W3 \sim 1.22$, i.e., the mass within 200pc in the Aq-W2 simulation has converged to better than $\sim 22\%$.

As can be inferred from Fig. 3.5, the WDM subhaloes have similar central masses to the observed satellite galaxies, while the CDM subhaloes are almost all too massive at the corresponding radii. The CDM subhaloes have central masses that are typically 2-3 times larger than the Milky Way satellites. There is one CDM subhalo that lies at lower masses than all 9 dwarf spheroidals, but this had one of the three most massive progenitors and has been almost completely destroyed by tidal forces.

Fig. 3.4 and 3.5 show that the WDM subhaloes are less centrally concentrated than those in the corresponding CDM halo. Concentrations typically reflect the epoch at which the halo formed (Navarro et al., 1996c, 1997; Eke et al., 2001). To investigate systematic differences in the formation epoch of the WDM and CDM subhaloes in our sample, we must choose a suitable definition of formation time. Since we are considering only the central mass, and we do not wish to introduce scatter in any correlation by using subhaloes that may have been stripped, we define the formation time as the first time at which the total progenitor mass exceeds the mass within 1 kpc at infall. The correlation of this redshift with the mass within 1 kpc at infall is shown in Fig. 3.6 for the 12 most massive WDM and CDM progenitors that survive to $z = 0$ as distinct subhaloes. Evidently, the proto subhaloes that form later, which are generally WDM not CDM ones, have the lowest central masses. The mean difference between the top 12 WDM and CDM proto-subhalo masses within 1 kpc is approximately a factor 2.

Because of their later formation time, the infalling WDM subhaloes already have

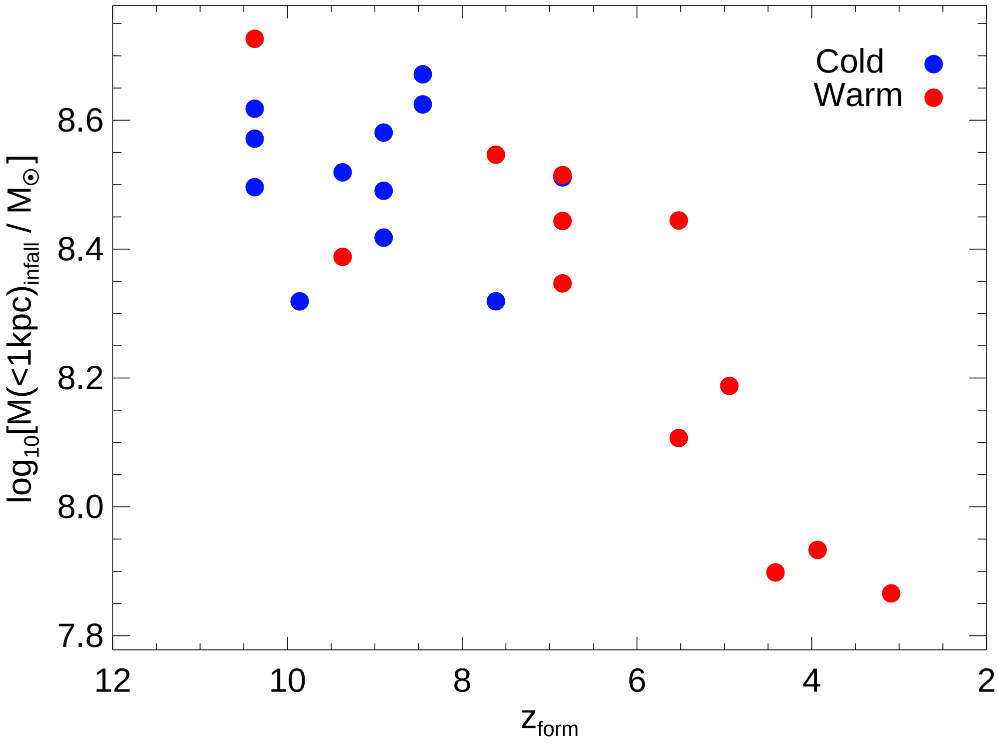

Figure 3.6: The correlation between subhalo central mass at infall and the redshift of formation, z_{form}, defined as the redshift at which the total mass of each proto subhalo first exceeded this value. Central mass is defined within 1 kpc, and CDM and WDM results are shown with blue and red symbols respectively.

lower central masses than those falling into the corresponding CDM haloes. As their mass is less centrally concentrated, the WDM subhaloes are more susceptible to stripping. While this is most important in the outer regions of the subhaloes, the mass profiles in Fig. 3.5 show that the inner regions of some of the subhaloes have also endured significant depletion since infall. Fig. 3.7 shows, for both WDM and CDM subhaloes, the ratio, $M_{z=0}(<r)/M_{\mathrm{infall}}$, of the present day mass contained within $r = 0.5$, 1 and 2 kpc to the mass at infall, as a function of the central mass at infall at the chosen radius. On average, the median mass at infall for WDM is lower by ~ 0.15 dex than the corresponding mass for CDM. One subhalo gains mass between infall and $z = 0$ because it accretes another subhalo. While there is a large scatter among the different subhaloes, with some having lost the majority of their central mass since infall, no significant systematic difference between WDM and CDM subhaloes is apparent. This implies that

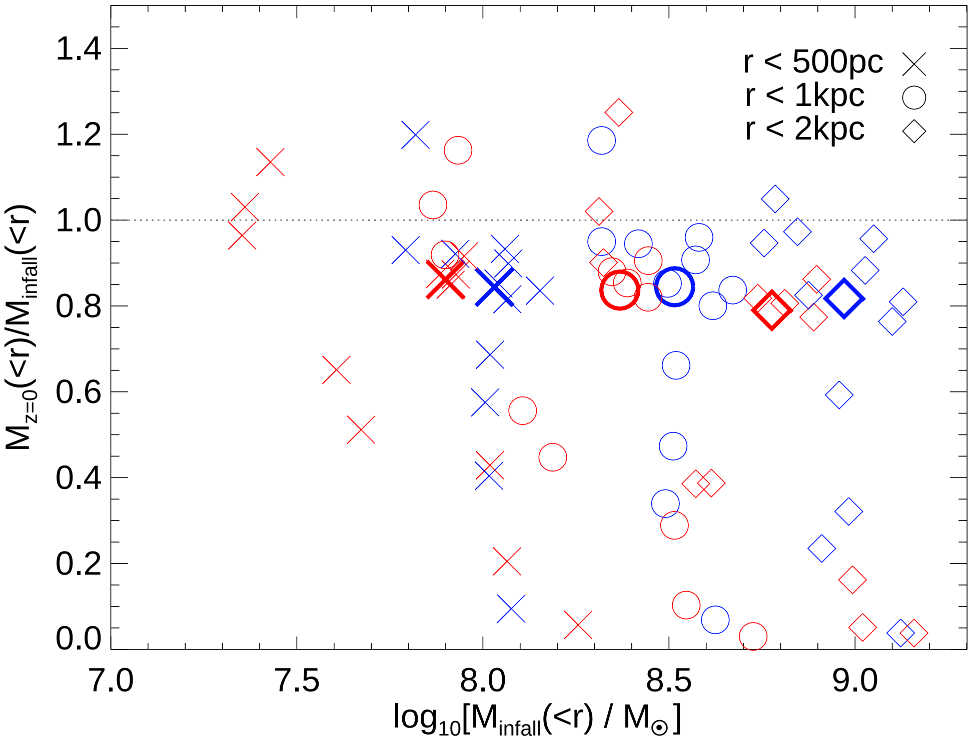

Figure 3.7: The variation with subhalo mass at infall of the ratio of the present day mass to the infall mass contained within 500pc, 1kpc and 2kpc. Data are shown for the 12 subhaloes identified at $z = 0$ which had the most massive progenitors, with CDM in blue and WDM in red. The symbol type denotes the radius interior to which the central mass is being measured and large symbols show the medians of the corresponding distributions. We find no systematic differences between the CDM and WDM subhalo mass ratios.

the reason why the WDM subhaloes provide a better fit to the half-light masses of the 9 Milky Way dwarf spheroidals studied by Wolf et al. (2010) is not excess stripping but the later formation time, and correspondingly typical lower concentration, of the WDM proto subhaloes compared to their CDM counterparts.

3.4 Discussion and conclusions

The properties of the satellite galaxies of the Milky Way have posed a longstanding puzzle for cold dark matter theories of galaxy formation. Two aspects of this puzzle have reportedly been separately and independently solved. One is the luminosity function of the satellites. The basic idea - the suppression of galaxy formation in small haloes by a combination of feedback effects produced by the reionization of gas at high redshift and supernova heating - was suggested by Dekel and Silk (1986) and Kauffmann et al. (1993) and explored thoroughly in the early 2000s (Bullock et al., 2000; Benson et al., 2002; Somerville, 2002) and has been revisited many times since then (see Font and et al., 2011, and references therein for the most recent discussion). The other aspect concerns the dynamical state of the satellites. Strigari et al. (2010) have shown that there exist subhaloes in the Aquarius cold dark matter simulations that fit the stellar spectroscopic data for the well-studied satellites extremely well.

There is a third aspect to the puzzle, however, that has not yet been fully addressed and this is whether the cold dark matter models that account for the satellite luminosity function also account for the satellites' internal dynamics. In other words, do the models assign the correct luminosities to subhaloes with the correct dynamics? At face value, the answer seems to be 'no'. This is already evident in the analysis of Strigari et al. (2010) in which the best fit dynamical models imply velocity dispersions (or equivalently $V_{\rm max}$ values) for the brightest dwarf spheroidals that are smaller than the velocity dispersions of the largest subhaloes. It is this discrepancy that has recently been highlighted by Boylan-Kolchin et al. (2011).

In this Chapter, we have compared a high resolution N-body simulation of one of the Aquarius galactic haloes with a warm dark matter counterpart. The initial conditions for both had the same phases and the same unperturbed particle positions. For the warm dark matter simulation we chose a form of the power spectrum corresponding to one of the models discussed by Asaka and Shaposhnikov (2005) and Boyarsky et al. (2009c), in which the dark matter is a sterile neutrino with mass $\sim 2{\rm keV}$, just consistent with various astrophysical constraints (Boyarsky et al., 2009a). The suppression of the power spectrum at masses below $\sim 10^{10}{\rm M}_{\odot}$ delays the formation of the haloes that will end up hosting the satellites and, as we have shown, this lowers their concentration compared to that of the corresponding cold dark matter haloes. This is enough to reconcile the dynamics of the subhaloes with the data.

While a warm dark matter model naturally produces haloes that are less concentrated than their cold dark matter counterparts, this is only one possible solution to the puzzle. Other forms of dark matter such as "meta-cold dark matter" resulting from the decay of cold thermal relics could produce a similar outcome (Strigari et al., 2007). Also, it must be borne in mind that the values of $V_{\rm max}$ for Milky Way satellites are not directly measured but inferred by making assumptions about their dynamical state. If some of these assumptions are unrealistic, this could lead to an underestimate of the values of $V_{\rm max}$ (e.g. Stoehr et al., 2002). Another possibility is that the satellite population of the Milky Way is not typical of the average to which the model predictions apply. It has recently been shown by Liu et al. (2011), Guo et al. (2011) and Lares et al. (2011) that the bright end of the Milky Way satellite luminosity function is different from the average. Finally, we cannot exclude the possibility that baryonic processes occurring during the formation of satellite galaxies in the CDM cosmogony might have lowered the concentration of haloes, for example, in the manner suggested by Navarro et al. (1996a). Recent simulations (Read and Gilmore, 2005; Mashchenko et al., 2008; Governato et al., 2010) suggest that these processes could be important although it remains to be seen if they are enough to reconcile the CDM model with the dynamics of the Milky Way satellites.

Chapter 4

The properties of warm dark matter haloes

4.1 Introduction

The identity of the dark matter remains one of the central unsolved problems in cosmology. Various lines of evidence, for example, data on the cosmic microwave background radiation, indicate that the dark matter is made up of non-baryonic elementary particles (e.g. Larson et al., 2011), but exactly which kind (or kinds) of particle are involved is not yet known. For the past thirty years or so attention has focused on cold dark matter (CDM) (see Frenk and White, 2012, for a review), for which there are well-motivated candidates from particle physics, for example, the lightest supersymmetric particle or neutralino (Ellis et al., 1984), or the axion (Preskill et al., 1983). Cold dark matter particles have negligible thermal velocities during the era of structure formation.

More recently, particle candidates that have appreciable thermal velocities at early times, and thus behave as warm, rather than cold, dark matter have received renewed attention. The best-known example is a sterile neutrino which, if it occurs as a triplet, could explain observed neutrino oscillation rates and baryogenesis (e.g. Asaka and Shaposhnikov, 2005). This model is known as the neutrino minimal standard model (νMSM; Boyarsky et al., 2009c,b). Warm particles are relativistic when they decouple from the primordial plasma and become non-relativistic during the radiation-dominated era. This causes the particles to free stream out of small perturbations, giving rise to a cutoff in the linear matter power spectrum and an associated suppression of structure formation on small scales. When the particles collect at the centres of dark matter haloes, their non-negligible thermal velocities reduce their phase-space density compared to the CDM case and this can result in the formation of a 'core' in the density profile whose size varies inversely with the velocity dispersion of the halo (Hogan and Dalcanton, 2000). However, recent analytical and numerical work (Macciò et al., 2012; Shao et al., 2013; Macciò et al., 2013) has shown that the resulting cores are astrophysically uninteresting being, in particular, significantly smaller than the cores claimed to be present in dwarf satellites of the Milky Way (e.g. Gilmore et al., 2007; de Vega and Sanchez, 2010).

On comoving scales much larger than the free-streaming cutoff, the formation of structure procedes in very similar ways whether the dark matter is cold or warm and so current astronomical observations on those scales (larger than $\sim$ 1Mpc) cannot distinguish between these two very different types of dark matter particles. Successes of the CDM paradigm, such as the remarkable agreement of its predictions (in a universe dominated by a constant vacuum energy, Λ) with observations of temperature fluctuations in the cosmic microwave background radiation (e.g. Komatsu et al., 2011) and the clustering of galaxies (e.g. Cole et al., 2005), carry over, for the most part, to a warm dark matter (WDM) model. To distinguish between these two types of dark matter using astrophysical considerations it is necessary to resort to observations on the scale of the Local Group.

Over the past decade, surveys such as SDSS (York, 2000), PAndAS (Ibata et al., 2007) and Pan-STARRS (Kaiser et al., 2010) have begun to probe the local universe in detail. A number of new dwarf spheroidal (dSph) satellite galaxies have been discovered around the Milky Way and M31 (e.g. Willman et al., 2005b; Walsh et al., 2007; Martin et al., 2009; Bell et al., 2011; Martin et al., 2013). Follow-up studies of stellar kinematics have been used to investigate their dynamics and mass content (Walker et al., 2009, 2010; Wolf et al., 2010; Tollerud et al., 2012). These data indicate that some dSphs have mass-to-light ratios of around 100, and are thus systems in which the properties of dark matter may be most directly accessible. Analyses of the number and structure of dSphs should therefore provide strong constraints on the nature of the dark matter.

The luminosity function of satellites in the Local Group has now been determined to quite faint magnitudes (Koposov et al., 2008; Tollerud et al., 2008), confirming that there are far fewer satellites around galaxies like the Milky Way than there are subhaloes in cosmological N-body simulations from CDM initial conditions (Diemand et al., 2005; Springel et al., 2005). This discrepancy is not new and can be readily explained by the physics of galaxy formation because feedback processes are very efficient at suppressing the formation of galaxies in small haloes (Bullock et al., 2000; Benson et al., 2002; Somerville, 2002). Recent hydrodynamic simulations have confirmed this conclusion originally deduced from semi-analytical models of galaxy formation (Okamoto et al., 2010; Wadepuhl and Springel, 2011).

Kinematical studies of the bright Milky Way satellites can constrain the internal structure of their dark matter subhaloes. Gilmore et al. (2007) argued that the data support the view that dSphs have central cores, in apparent contradiction with the results of N-body simulations which show that CDM haloes and their subhaloes have central cusps (Navarro et al., 1996c, 1997; Springel et al., 2005). Strigari et al. (2010) explicitly showed that it is always possible to find CDM subhaloes formed in the Aquarius high resolution simulations of galactic haloes (Springel et al., 2008a) that are consistent with these data, however the subhaloes that best fit the kinematical data for the bright satellites turn out *not* to be the most massive ones, as would naturally be expected for these bright satellites. This surprising result was explored in detail in the Aquarius simulations by Boylan-Kolchin et al. (2011, 2012), who dubbed it the "too big to fail" problem; it was also found in gasdynamic simulations of Aquarius haloes by Parry et al. (2012). The discrepancy has attracted a great deal of attention because it could potentially rule out the existence of cold dark matter. Possibly related problems include the paucity of galaxies in voids (Tikhonov et al., 2009), and the local HI velocity width function (Zavala et al., 2008; Papastergis et al., 2011) (but see Sawala et al., 2012).

A number of solutions to the "too big to fail" problem have now been proposed. Within the CDM context, perhaps the simplest is that the virial mass of the Milky Way halo is smaller than the average mass, $M_{200} \sim 1.4 \times 10^{12}\mathrm{M}_{\odot}$, of the Aquarius haloes (Vera-Ciro et al., 2012; Wang et al., 2012). A somewhat more uncertain possibility is that the central density of CDM subhaloes may have been reduced by the kind of explosive baryonic processes proposed by Navarro et al. (1996b) which appear to occur in some recent hydrodynamic simulations (Pontzen and Governato, 2012; Brooks and Zolotov, 2012; Parry et al., 2012; Zolotov et al., 2012) but not in others (di Cintio et al., 2011) which assume different prescriptions for physics that are not resolved in the simulations. In particular, the work of Pontzen and Governato (2012) suggests that the periodic expulsion of gas non-adiabatically by intense supernova feedback events may not only reduce the central density but even create a cored density profile: however, the feasiblity of this mechanism is still a matter of debate (Garrison-Kimmel et al., 2013).

More radical solutions to the "too big to fail" problem require abandoning cold dark matter altogether. Vogelsberger et al. (2012) show that simulations with a new class of "self-interacting" dark matter could solve the problem. However, a solution is also possible with more conventional assumptions. In particular, Lovell et al. (2012) show that simulations with WDM produce very good agreement with the dSph kinematical data. The absence of small scale power in the initial fluctuation field causes structure to form later than in the CDM case. Haloes of a given mass thus collapse when the mean density of the universe is smaller and, as a result, end up with lower central densities (Avila-Reese et al., 2001). However, the WDM model they assumed was 'too warm', in the sense that it assumed too low a particle mass (and thus too large a cut-off scale in the initial power spectrum) and produced only 18 dark matter subhaloes within 300 kpc of the main halo centre whereas observations suggest the actual number of satellites may be over an order of magnitude greater (Tollerud et al., 2008).

The results of Lovell et al. (2012) and related results by Macciò et al. (2012); Shao et al. (2013); Macciò et al. (2013) raise the question of whether it is possible to find a range of WDM particle masses that lead to 'warm enough' models that match satellite central densities but which are also 'cold enough' to generate the observed number of satellite galaxies (Polisensky and Ricotti, 2011; Kamada et al., 2013). In this work we examine both the number and structure of satellite galaxies in simulations as a function of the WDM particle mass.

The first requirement is to be able to count accurately the number of dark matter haloes formed in WDM cosmologies. The first simulations of WDM models (Bode et al., 2001) showed the halo mass function to be suppressed as expected, but also found that at least 90 per cent of haloes, depending on the choice of power spectrum cutoff, formed from the fragmentation of filaments and had masses below the smoothing scale. Wang and White (2007) examined this effect in hot dark matter (HDM) simulations (which assume a much larger power spectrum cutoff scale than in WDM) and showed that the fragmentation of filaments depends on the resolution of the simulation, thus concluding that most of the haloes in the Bode et al. (2001) simulations were due to a numerical artifact.

In this Chapter we introduce a series of methods for identifying spurious haloes in simulations, and then use our cleaned halo sample to examine the distribution and structure of WDM haloes as a function of the power spectrum cutoff. The Chapter is organised as follows. In Section 4.2 we present our simulation set and in Section 4.3 we describe our algorithm for removing spurious subhaloes. We then present our results in Section 4.4, and draw conclusions in Section 4.5.

4.2 The simulations

We begin by describing the details of our simulations, the procedure for generating initial conidtions and a general overview.

4.2.1 Simulation parameters

Our N-body simulation suite is based upon that of the Aquarius Project (Springel et al., 2008a), a set of six (Aq-A through to Aq-F) galactic dark matter haloes simulated at varying resolution (levels 1-5, where level 1 corresponds to the highest resolution). The Aquarius simulations assumed cosmological parameter values derived from the WMAP year 1 data. These have now been superseded and in this Chapter we use the cosmological parameter values derived from the WMAP year 7 data (Komatsu et al., 2011): matter density, $\Omega_m = 0.272$; dark energy density, $\Omega_\Lambda = 0.728$; Hubble parameter, $h = 0.704$; spectral index, $n_s = 0.967$; and power spectrum normalization $\sigma_8 = 0.81$.

Our main set of simulations follows the formation of four WDM galactic haloes with different effective warm dark matter particle masses. The initial phases in the fluctuation spectrum are identical to those of the original CDM Aq-A halo but the transfer function is that appropriate to WDM as described below. In addition, we resimulated the level-2 Aq-A halo using the WMAP year-7 cosmology. For all five haloes (one CDM and four WDM), we ran simulations at different resolution. Our "high resolution" suite corresponds to level-2 in the original Aquarius notation; it has particle mass of $1.55 \times 10^4 \mathrm{M}_\odot$, and gravitational softening length of $\epsilon = 68.1\mathrm{pc}$. All haloes were also run at "low resolution" (level-4), with particle mass of $4.43 \times 10^5 \mathrm{M}_\odot$ and gravitational softening of $\epsilon = 355.1\mathrm{pc}$. Finally, we ran an intermediate resolution version (level 3) of the warm dark matter models with the lightest and heaviest dark matter particles, with particle mass $5.54 \times 10^4 \mathrm{M}_\odot$ and $\epsilon = 125.0\mathrm{pc}$, in order to facilitate convergence studies. All haloes were simulated from $z = 127$ to $z = 0$ using the GADGET3 N-body code (Springel et al., 2008a).

To set up the initial conditions for the WDM runs we employed the transfer function, $T(k)$, defined as

$$P_{\rm WDM}(k) = T^2(k) P_{\rm CDM}(k). \tag{4.1}$$

where $P(k)$ denotes the power spectrum as a function of comoving wavenumber k. We adopted the fitting formula for $T(k)$ given by Bode et al. (2001):

$$T(k) = (1 + (\alpha k)^{2\nu})^{-5/\nu}, \tag{4.2}$$

where ν and α are constants. Bode et al. (2001) and Viel et al. (2005) find that ν can take values between 1 and 1.2 depending on the fitting procedure; we adopted $\nu = 1$ for simplicity. The position of the cutoff in the power spectrum is determined by the parameter α, such that higher values of α correspond to cutoffs at larger length scales. In principle, the initial conditions for WDM simulations should include thermal velocities for the particles (Colín et al., 2008; Macciò et al., 2012; Shao et al., 2013). However, at the resolution of our simulations, the appropriate velocities would have a negligible effect (Lovell et al., 2012) and are therefore not included.

For our four WDM models we adopted values of α of $0.0199h^{-1}{\rm Mpc}$, $0.0236h^{-1}{\rm Mpc}$, $0.0297h^{-1}{\rm Mpc}$, and $0.0340h^{-1}{\rm Mpc}$ respectively. The last of these corresponds to the original WDM simulation presented in Lovell et al. (2012) which, however, assumed the WMAP year-1 cosmological parameters. That model was originally chosen as a thermal relic approximation to the M2L25 model of Boyarsky et al. (2009b), the $\nu{\rm MSM}$ parameter combination that has the largest effective free-streaming length that is still consistent with bounds from the Lyman-α forest (but see also Viel et al., 2013b).

Viel et al. (2005) related α to a generic thermal relic warm dark matter particle mass, $m_{\rm WDM}$, using the formula:

$$\alpha = \frac{0.049}{h{\rm Mpc}^{-1}} \left(\frac{m_{\rm WDM}}{1{\rm keV}}\right)^{-1.11} \left(\frac{\Omega_{\rm WDM}}{0.25}\right)^{0.11} \left(\frac{h}{0.7}\right)^{1.22}, \tag{4.3}$$

where $\Omega_{\rm WDM}$ is the WDM contribution to the density parameter. This differs slightly from the equivalent equation presented in Bode et al. (2001), however the difference in the masses for a given α is only of order a few per cent. We list the thermal relic masses for each of our models in Table 4.1, and use these masses as labels for the models, namely $m_{2.3}$, $m_{2.0}$, $m_{1.6}$, and $m_{1.4}$; we denote the CDM simulation with WMAP year-7 parameters as CDM-W7. A transfer function with $\nu = 1$ has an amplitude slightly lower than that of the $\nu = 1.12$ case around the cut off scale, and so the masses we quote are not directly comparable to those in works such as Viel et al. (2005, 2008). We therefore determine which particle mass combined with a $\nu = 1.12$ transfer function gives the best approximation to our $\nu = 1$ transfer function for the scales at which $T^2(k) > 0.5$, and quote these results in Table 4.1. We also give the cutoff mass scale for each simulation, which we define as the mass within a top hat filter which, when convolved with the CDM power spectrum, results in a function that peaks at the same value of k as the WDM power spectrum.

The linear theory power spectra used to set up the initial conditions are plotted in Fig. 4.1. By construction, the peak of the power spectrum moves to higher k as α decreases (and the particle mass increases). For all WDM models the initial power spectrum peaks at a value of k smaller than the Nyquist frequency of the particle load in the simulation. This will lead to the formation of spurious halo as mentioned in the introduction.

Self-bound haloes were identified using the SUBFIND algorithm (Springel et al., 2001b); they are required to contain at least 20 particles. The largest SUBFIND group is the galactic halo itself, to which we will refer as the 'main halo'. Smaller haloes that reside within the main halo are known as 'subhaloes', whereas those that are outside the main halo are 'independent haloes'. Most of the subhaloes will have experienced gravitational stripping whilst most of the independent haloes will have not.

A first view of the simulations is presented in Fig. 4.2. The smooth component of the main haloes is very similar in all five models: in all cases, the haloes are similarly centrally concentrated and elongated. The main difference is in the abundance of subhaloes. The myriad small subhaloes evident in CDM-W7 are mostly absent in the WDM models. For these, the number of subhaloes decreases as α increases (and the WDM particle mass decreases).

The apparent similarity of the main haloes displayed in Fig. 4.2 is quantified in Table 4.2 which lists the masses and radii of the largest friends-of-friends halo in each simulation. The table gives their masses enclosed within radii of mean density 200 times

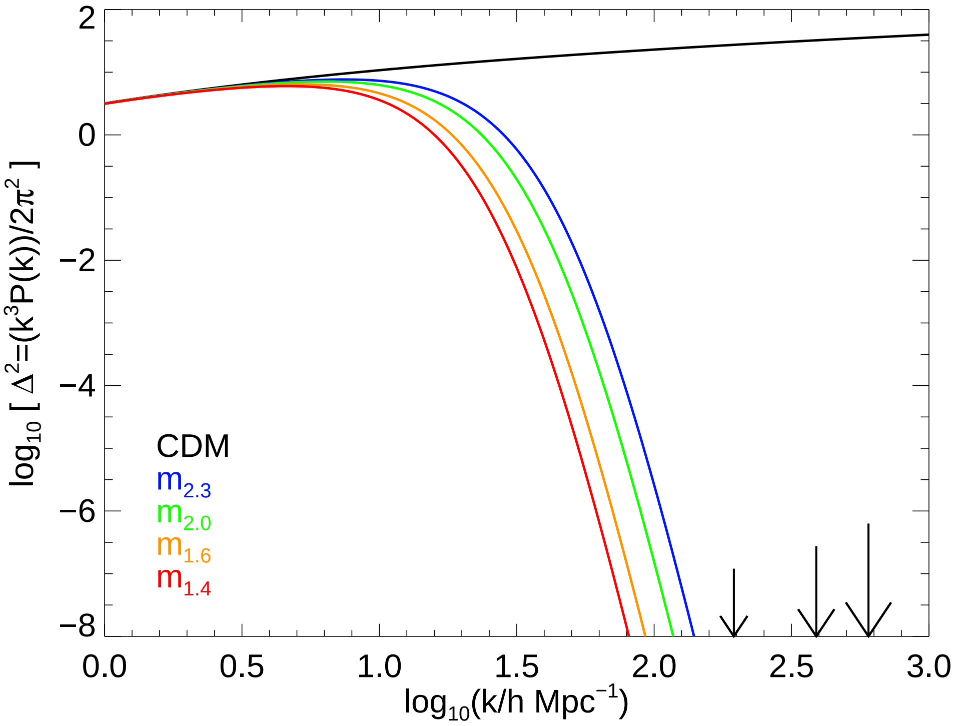

Figure 4.1: The linear theory power spectrum used in the simulations. The black line corresponds to the CDM model, CDM-W7, while the blue, green, orange and red lines correspond to the $m_{2.3}$, $m_{2.0}$, $m_{1.6}$, and $m_{1.4}$ WDM models respectively. The arrows mark, in order of smallest to largest, the Nyquist frequency of our low, medium, and high resolution simulations.

Simulation	m_{WDM}[keV]	$\alpha[h^{-1}\mathrm{Mpc}]$	$M_{\mathrm{th}}[\mathrm{M}_\odot]$	$m_{\mathrm{WDM}}(\nu = 1.12)$[keV]
CDM-W7	–	0.0	–	–
$m_{2.3}$	2.284	0.01987	1.4×10^9	1.770
$m_{2.0}$	1.959	0.02357	1.8×10^9	1.555
$m_{1.6}$	1.591	0.02969	3.5×10^9	1.265
$m_{1.4}$	1.408	0.03399	5.3×10^9	1.106

Table 4.1: Parameters of the simulations. The parameter α determines the power spectrum cutoff (Eqn. 4.2); m_{WDM} is the thermal relic mass corresponding to each value of α; and M_{th} is the cutoff mass scale defined using a top hat filter as described in the text. The final column contains the particle masses that, when combined with the $\nu = 1.12$ transfer function of Viel et al. (2005), give the best approximation to our $\nu = 1$ transfer functions.

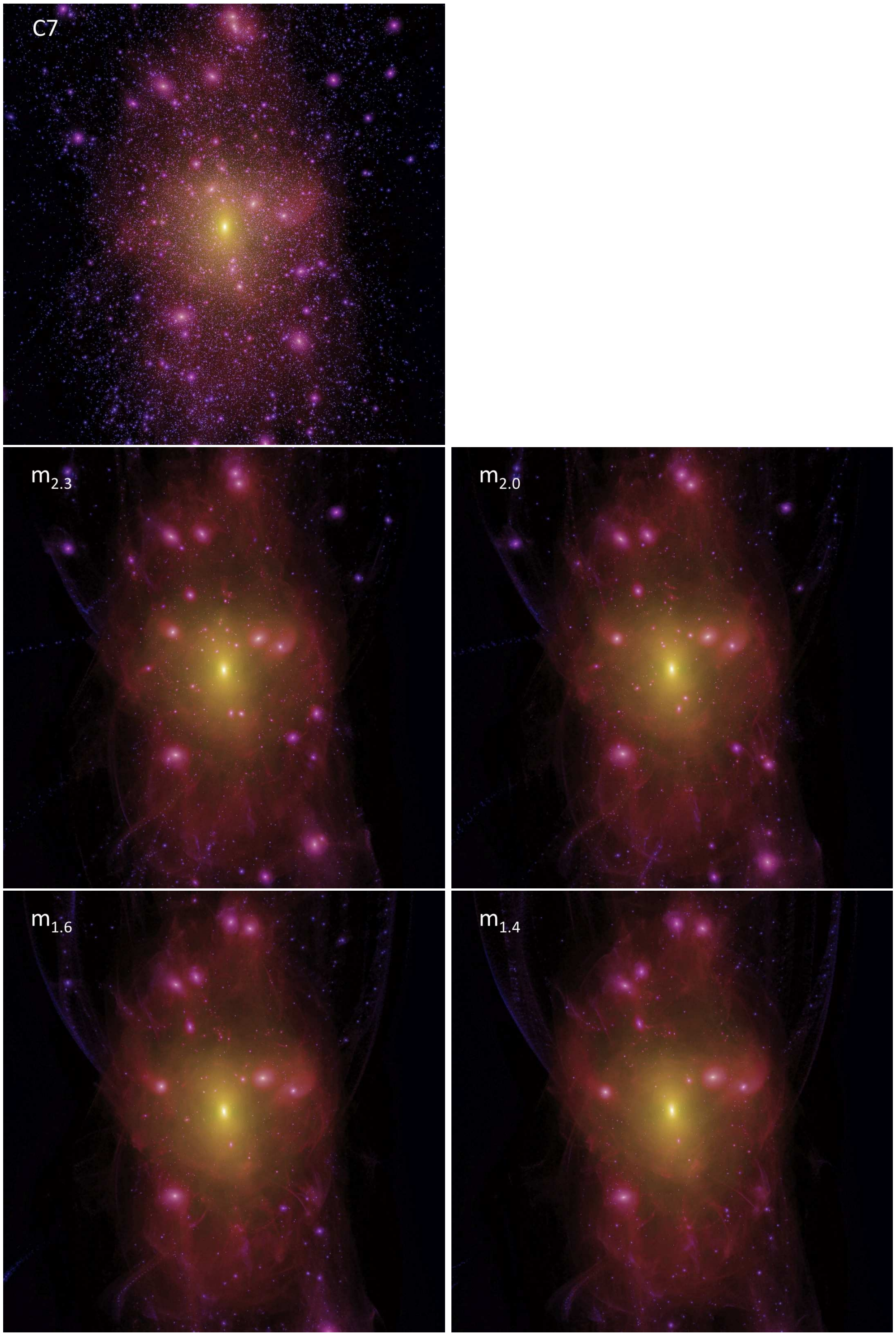

Figure 4.2: Images of our haloes at redshift $z = 0$. The panels show CDM-W7 (top), $m_{2.3}$, $m_{2.0}$, $m_{1.6}$, and $m_{1.4}$ (left to right, then top to bottom). Image intensity indicates projected squared dark matter density and hue density-weighted mean velocity dispersion (Springel et al., 2008a). Each panel is 1.5Mpc on a side.

Simulation	$M_{200}[\mathrm{M}_{\odot}]$	$r_{200}[\mathrm{kpc}]$	$M_{200b}[\mathrm{M}_{\odot}]$	$r_{200b}[\mathrm{kpc}]$
CDM-W7	1.94×10^{12}	256.1	2.53×10^{12}	432.1
$m_{2.3}$	1.87×10^{12}	253.4	2.52×10^{12}	431.4
$m_{2.0}$	1.84×10^{12}	251.7	2.51×10^{12}	430.8
$m_{1.6}$	1.80×10^{12}	250.1	2.49×10^{12}	429.9
$m_{1.4}$	1.80×10^{12}	249.8	2.48×10^{12}	429.0
Aq-A2	1.84×10^{12}	245.9	2.52×10^{12}	433.5

Table 4.2: Properties of the main friends-of-friends halo in each high resolution simulation. The radii r_{200} and r_{200b} enclose regions within which the mean density is 200 times the critical and background density respectively. The masses M_{200} and M_{200b} are those contained within these radii. We also reproduce data from the original Aquarius Aq-A2 halo.

the critical density (M_{200}) and 200 times the background density (M_{200b}). There is a slight trend of decreasing mass with increasing α, but the maximum change is only 7 per cent for M_{200} and 2 per cent for M_{200b}. The change in cosmological parameters also makes only a small difference: M_{200} is 5 per cent higher for CDM-W7 than for the original Aquarius halo with WMAP year 1 parameters.

4.2.2 The structure of the main haloes

The density profiles of the main haloes (including substructures) in our high resolution simulations are plotted in Fig. 4.3. There is good agreement amongst all the haloes at radii (10-100) kpc, with the five profiles agreeing to better than 10 per cent. At larger radii, systematic differences between CDM-W7 and the WDM models begin to appear and these become increasingly pronounced for the warmer models. These differences are due to slight variations in the position of large substructures in the outer parts. There are also small differences at much smaller radii ($< 10\mathrm{kpc}$) which are are not systematic and are thus likely due to stochastic variations in the inner regions.

The radial variation of the logarithmic slope of the density profile of each halo is plotted in Fig. 4.4. In all cases the slope at the innermost point plotted approaches the NFW asymptotic value of -1 but there is no evidence that the slope is converging. There is a slight tendency in the inner parts, $r < 4\mathrm{kpc}$, for the slope in the WDM models to

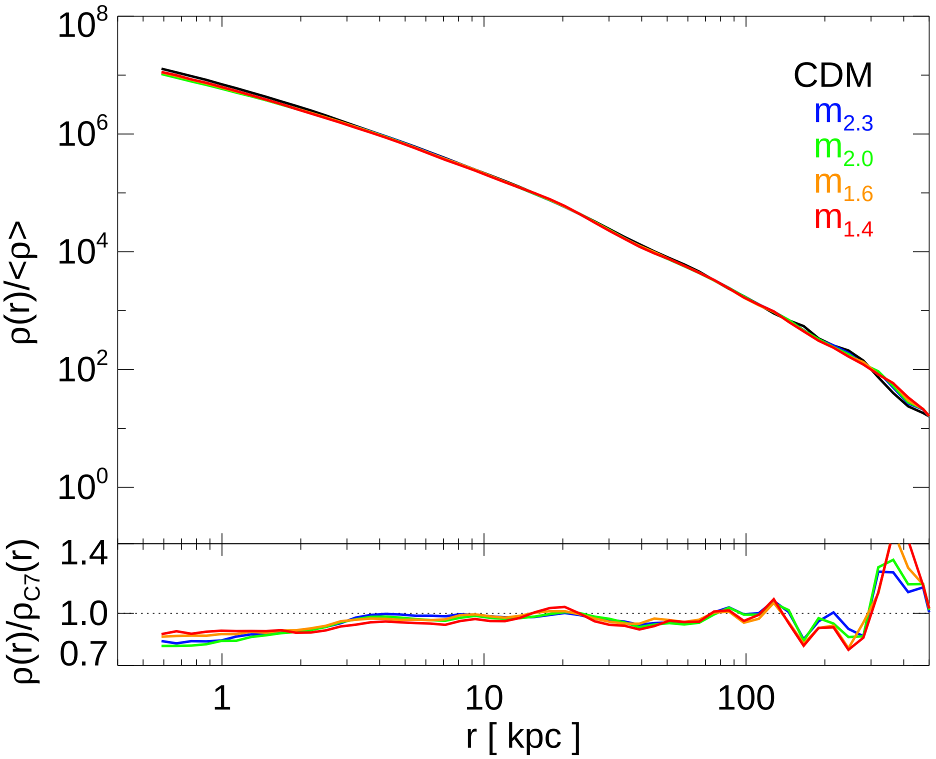

Figure 4.3: Density profiles of the main haloes (including subhaloes) in the simulations normalised by the background matter density. The line colours are as in Fig. 4.1. The profiles are plotted only beyond the 'Power radius' (Power et al., 2003) at which numerical convergence is expected. The bottom panel shows the profiles for the WDM simulations normalized to the profile for the CDM-W7 model.

be shallower than in the CDM model, but there is no obvious trend with α, possibly because of stochastic effects in the inner regions. Thus, apart from minor differences, the structure of these $\sim 10^{12}\mathrm{M}_{\odot}$ haloes varies little with power spectrum cut off, as expected for systems of mass $\gg M_{\rm th}$.

4.3 Removal of Spurious Haloes

One of the main aims of this study is to determine the mass function of subhaloes in WDM simulations. However, as we discussed in Section 5.1, simulations in which the initial power spectrum has a resolved frequency cutoff can undergo spurious fragmentation of filaments. An example is shown in Fig. 4.5, where we compare a region in one

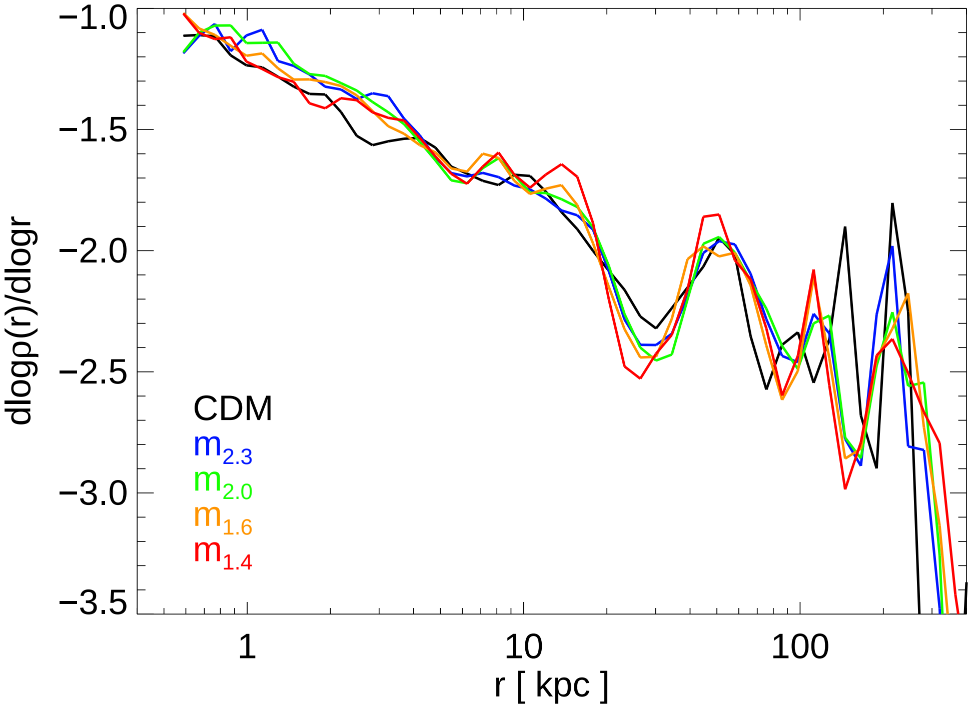

Figure 4.4: Radial variation of the logarithmic slope of the density profiles of the main haloes in the simulations. Line colours and plotting range are as in Fig. 4.3.

of our simulations with the corresponding region of a higher resolution simulation with the same initial conditions by plotting those particles that have collapsed into dark matter haloes. In both simulations there are two large haloes and several smaller ones. The large haloes have very similar sizes and positions in the two simulations, and can be regarded as genuine objects. By contrast, the small haloes have different sizes and positions in the two simulations; there are also more of them in the higher resolution case. As shown by Wang and White (2007), increasing the resolution even by rather large factors is not sufficient to prevent the formation of these artificial haloes. Future N-body codes that use phase space smoothing techniques may be able to alleviate this problem (Hahn et al., 2012; Shandarin et al., 2012; Angulo et al., 2013). At present, however, the only practical measure is to develop a reliable algorithm for identifying and removing these 'spurious' haloes from the halo catalogues.

We now introduce an algorithm for distinguishing between genuine and spurious subhaloes. It exploits three properties of the artifacts – mass, resolution dependence and

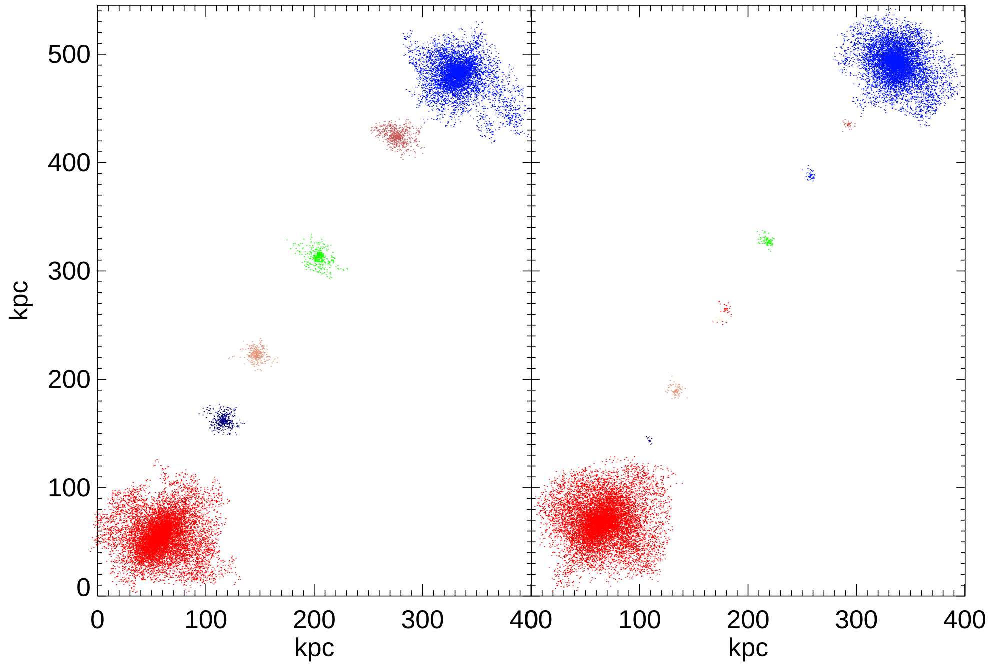

Figure 4.5: A region of a WDM simulation performed at two different resolutions. The particle mass for the high resolution simulation (*right*) is 29 times smaller than that of the low resolution case (*left*). Only particles in bound structures at this snapshot are shown. Particles are coloured according to the halo to which they belong. The number of particles plotted in each panel is equal to the number of bound-structure particles in the low resolution simulation; we have applied random sampling in the high resolution case.

the shape of the initial particle distribution – to define a series of cuts that isolate the artifacts. We present an outline of the method in Section 4.3.1 and provide details in Section 4.3.2. Note that while the results presented here have been derived for subhaloes that have been accreted into another halo, the algorithm is equally valid for independent haloes.

4.3.1 Outline of the methods

Previous simulations have shown that spurious haloes have small masses at formation and outnumber genuine haloes on those mass scales where they are present (Wang and

White, 2007). Thus, in principle, many spurious haloes can be singled out by applying a mass cut. This mass threshold, however, is not well defined because the mass function of genuine haloes overlaps that of the spurious haloes, so it is useful to introduce additional criteria to ensure that, as far as possible, all artificial haloes are identified and no genuine ones are removed.

The resolution dependence of the spurious fragmentation can be used to refine the distinction between genuine and artificial haloes. While genuine haloes in a simulation at a given resolution are expected to be present in the same simulation at higher resolution, this need not be the case for spurious haloes, as illustrated in Fig. 4.5. Springel et al. (2008a) showed that it is possible to match haloes and subhaloes between different resolution simulations by tracing their particles back to the initial conditions and identifying overlapping Lagrangian patches in the two simulations. We refer to the initial Lagrangian region of each halo, or more precisely the unperturbed simulation particle load, as its 'protohalo'. The initial positions of the particles displayed in Fig. 4.5 are shown in Fig. 4.6. The two large objects originate from protohaloes of similar size and location, but there are clear discrepancies in the number, location and mass of the small objects. Thus, attempts to match small haloes in the two simulations will often fail because spurious haloes in the low resolution calculation do not have a counterpart in the high resolution simulation.

A third criterion exploits the most striking feature visible in Fig. 4.6: the shapes of the protohaloes. Genuine protohaloes are spheroidal, whereas spurious protohaloes have much thinner, disc-like geometries. They can therefore be easily flagged as the progenitors of spurious haloes in the initial conditions.

In this study we are interested in objects that become subhaloes at the present day. We will apply these three criteria to them in the following order. Firstly, we identify a cut based on protohalo shape, rejecting from the catalogue all subhaloes flatter than a given threshold. Secondly, we apply a mass cut; finally we refine the mass cut using a matching procedure between simulations at different resolution. In what follows, we restrict attention to subhaloes lying within r_{200b} of the main halo centre at $z = 0$ except where we state otherwise.

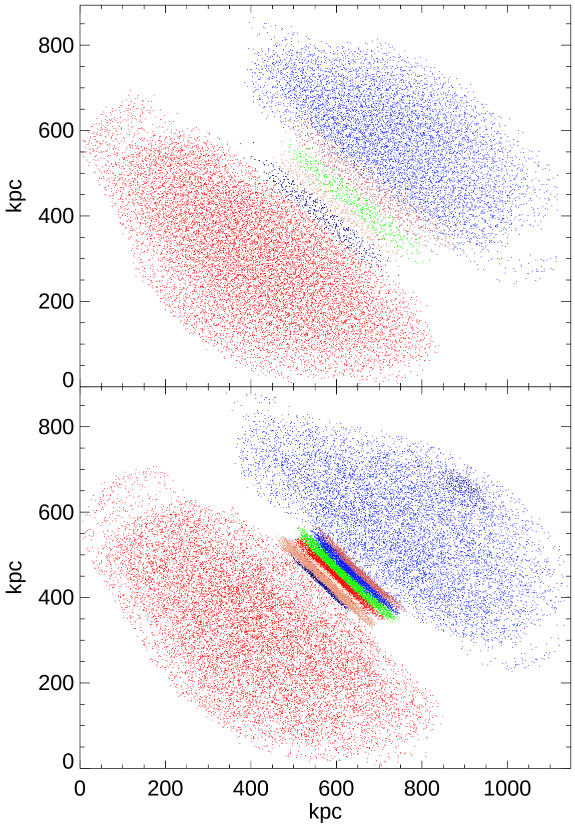

Figure 4.6: The particles of Fig. 4.5 traced back to their positions in the initial conditions. The low resolution simulation is shown in the top panel and the high resolution simulation in the bottom panel. Note the highly flattened configurations of spurious haloes.

4.3.2 Application

Protohalo shapes

To determine the flattening of protohaloes we consider all the particles that make up a subhalo at some epoch (determined below), find their positions in the unperturbed simulation particle load and calculate the inertia tensor of the particle set:

$$I_{ij} = \sum_{\text{all particles}} m(\delta_{ij}|\mathbf{x}|^2 - x_i x_j), \tag{4.4}$$

where δ_{ij} is the Kronecker delta function, m is the particle mass and $\mathbf{x}$ is the particle position relative to the protohalo centre of mass. We take $a \geq b \geq c$ to be the axis lengths of the uniform, triaxial ellipsoid that has the same moment of inertia tensor as the protohalo. We can then calculate $s = c/a$, known as the sphericity. A disc-like

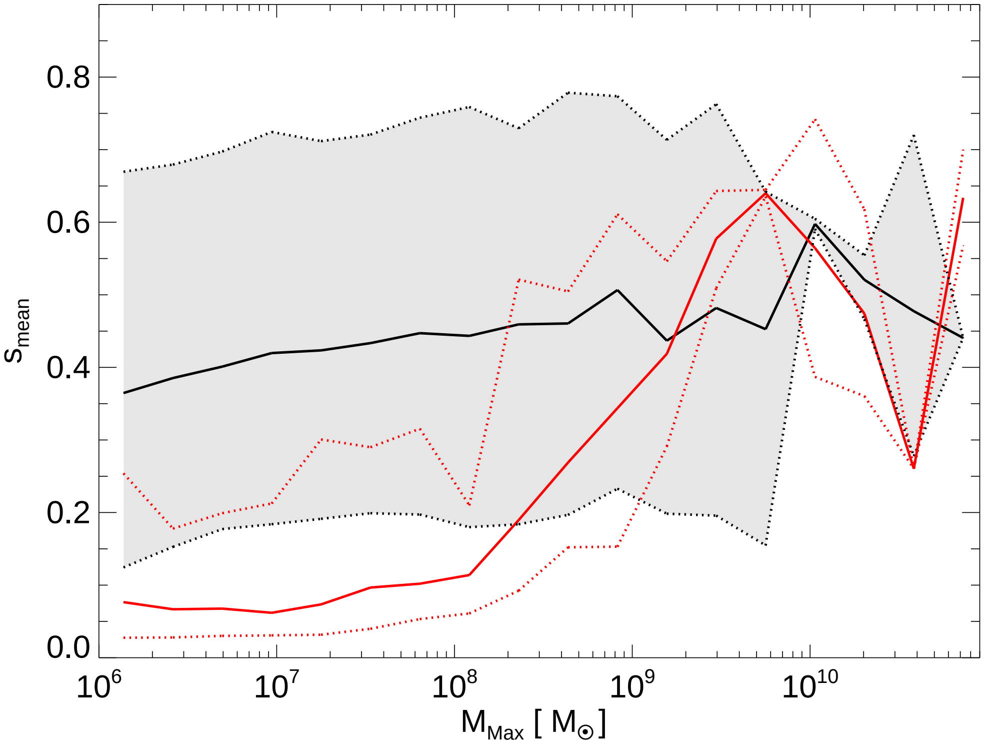

Figure 4.7: Mean subhalo sphericities as a function of $M_{\rm Max}$ for the high resolution CDM-W7 (black) and the $m_{1.4}$ (red) runs. The region between the upper and lower 99 percentiles of the CDM distribution is shown in grey; the same region for the $m_{1.4}$ simulation is delineated by the red dotted lines.

(or, more rarely, needle-like) spurious subhalo will have a major axis (disc diameter, a) much longer than its minor axis (disc thickness, c), and thus a small value of s. Genuine subhaloes, on the other hand, are spheroidal and thus have higher values of s.

We now need to choose an appropriate epoch at which to identify the particles that make up the protohalo. This should be well before the subhalo has fallen into a larger halo, after which its outer particles will be stripped. We select the earliest simulation snapshot below which the halo mass is more than half the maximum mass, the 'half-maximum mass snapshot'. The initial positions of the particles in the object at this time are used to evaluate the protohalo sphericity.

The distributions of s for the subhaloes that survive to $z = 0$ in the CDM-W7 and $m_{1.4}$ simulations are illustrated in Fig. 4.7, as a function of $M_{\rm Max}$. The mean sphericity is shown as a solid line and the 98% range is indicated by the dotted lines in each case. The figure reveals two regimes. For values of $M_{\rm Max} > 10^9{\rm M}_{\odot}$, the sphericity distributions in the two simulations are consistent with each other. For lower masses the protohaloes in the $m_{1.4}$ simulation are much flatter than in CDM-W7. This clear dichotomy suggests that most of the $m_{1.4}$ subhaloes with $M_{\rm Max} > 10^9{\rm M}_{\odot}$ are genuine and most of those with $M_{\rm Max} < 10^8{\rm M}_{\odot}$ are spurious. We can use the CDM subhaloes to define a cut in protohalo sphericity above which WDM subhaloes are likely to be real. We find that 99 per cent of CDM subhaloes containing more than 100 particles at the half-maximum mass snapshot have protohaloes with sphericity greater than ~ 0.16 (depending slightly on simulation resolution), which we denote $s_{\rm cut}$. We exclude from our cleaned subhalo catalogue any WDM subhalo whose protohalo has sphericity less than $s_{\rm cut}$, regardless of mass. This cut rejects between 86 per cent ($m_{2.3}$) and 93 per cent ($m_{1.4}$) of the WDM subhaloes as spurious. We have checked, as we show later, that the subhaloes rejected by this criterion do not have clear counterparts in pairs of simulations of different resolution, where in this case the difference in resolution is a factor of 8.

A first guess of the mass cut

For a first guess of the mass cut below which a majority of subhaloes are spurious, we resort to the results of Wang and White (2007). They showed that the characteristic mass below which spurious subhaloes begin to dominate the subhalo mass function is related to the matter power spectrum cutoff and the simulation resolution. The larger the value of the cutoff frequency and the higher the resolution of the simulation, the smaller is the mass of the largest spurious subhaloes. Wang and White (2007) derived an empirical formula for the mass at which spurious subhaloes begin to dominate:

$$M_{\rm lim} = 10.1\bar{\rho}dk_{\rm peak}^{-2}, \tag{4.5}$$

where $\bar{\rho}$ is the mean density of the Universe, d is the mean interparticle separation (a measure of resolution), and $k_{\rm peak}$ is the wavenumber at which the dimensionless power spectrum, $\Delta^2(k)$, has its greatest amplitude. We can apply this formula to $M_{\rm Max}$ to estimate a cut below which the majority of the subhaloes will be spurious. Some genuine haloes will have $M_{\rm Max}$ below this threshold but the mass limit can be refined using the matching criterion.

Matching subhaloes between simulations

A subhalo that is present in both a low resolution simulation (LRS) and in its high resolution counterpart (HRS) is likely to be genuine. We can use this property to refine the mass cut. We set the cutoff mass to be $M_{\mathrm{min}} = \kappa M_{\mathrm{lim}}$, where κ is a constant such that the number of LRS subhaloes of mass greater than M_{min} is equal to the number of subhaloes with matches in the HRS. We will assume that the value of κ determined for the LRS subhaloes is also applicable to the HRS catalogues.

We now introduce an algorithm for finding high resolution counterparts of the low resolution subhaloes. Genuine haloes should originate from the same Lagrangian region regardless of resolution. Therefore, to match subhaloes we require a quantitative measure to compare these Lagrangian regions in simulations of different resolution and check that they overlap and have the same shape. These shapes are defined by point-like particles. In order to develop a quantitative measure of the overlap we need to smooth these points. We measure the degree to which a pair of objects in different resolution simulations are the 'same' by comparing the entirety of the regions from which they form. We introduce a statistic:

$$R = \frac{U_{\mathrm{AB}}^2}{U_{\mathrm{AA}} U_{\mathrm{BB}}}, \tag{4.6}$$

where $U_{XY} = \int \phi_{\mathrm{X}} \rho_{\mathrm{Y}} dV$, V is volume, and $\rho_{\mathrm{A/B}}$ and $\phi_{\mathrm{A/B}}$ are the density of and gravitational potential due to the matter distributions A/B respectively. It can be shown using Green's Theorem that if the matter distribution of subhalo A is proportional everywhere to that of subhalo B, $R = 1$; for any other configuration $R < 1$. We apply this formula to our candidate LRS-HRS protohalo particle distributions, representing each particle as a spherical shell of radius equal to the LRS mean interparticle separation and with infinitesimal thickness. The best match for the LRS subhalo will then be the HRS halo with which it attained the highest value of R. We retain this value of R for each LRS subhalo as our measure of its matching quality. A genuine LRS subhalo will have a good match at high resolution and therefore have a value of R close to 1, whereas a spurious subhalo will have a poor match and a lower value of R.

To find candidate matches, we first divide the simulation volume into a grid of cells of comoving length $\gtrsim 60\mathrm{kpc}$, and, for a given low resolution protohalo, choose as can-

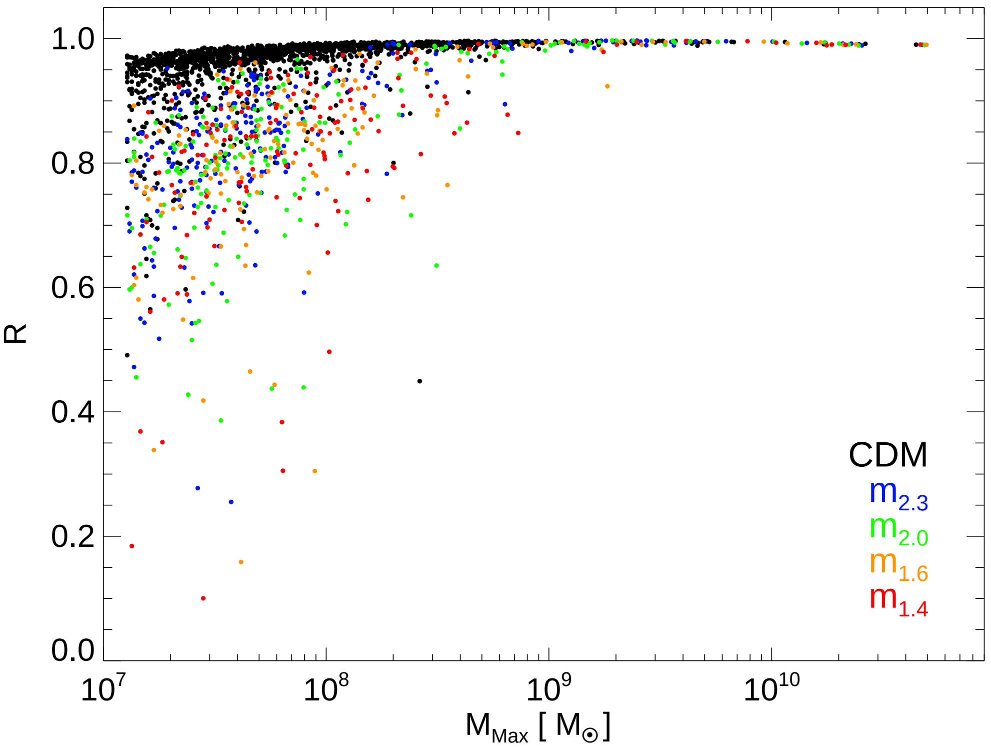

Figure 4.8: R as a function of $M_{\rm Max}$ for CDM and WDM LRS subhaloes matched to HRS counterparts (those that fail the sphericity cut are still included). The black dots denote CDM subhaloes, blue $m_{2.3}$, green $m_{2.0}$, orange $m_{1.6}$, and red $m_{1.4}$ (the same as Fig. 4.1.

didate matches the high resolution protohaloes that occupy the same and neigbouring grid cells. It is computationally expensive to calculate R for the largest subhaloes, but we found that random sampling of each halo with 10000 particles returned values of R that did not vary systematically with $M_{\rm Max}$ for subhaloes of $M_{\rm Max} > 10^9 {\rm M}_\odot$. We therefore adopt a threshold of 10000 particles. When attempting to match subhaloes between simulations, minor differences in which particles are assigned to each subhalo can have an impact on R. We mitigate this problem by performing the calculation for both the maximum-mass and half-maximum mass snapshots, selecting the higher value of the two for each subhalo. The resulting values of R are plotted as a function of $M_{\rm Max}$ in Fig. 4.8.

At high masses, the CDM and WDM protohaloes have R close to 1. As the protohalo mass decreases, R becomes systematically lower and the decline is much steeper for the WDM models, as expected in the presence of poorly matching spurious subhaloes. Unfortunately, a small proportion of CDM subhaloes also attain low values of R and the demarkation between the distributions of R for WDM and CDM is much less clear cut than we found for the sphericity measurement, s. Were we to take the same approach for R as we did for s, we would infer a cut in R of about 0.68. More than half of the WDM subhaloes have a value of R closer to 1 than this, and since the sphericity-based algorithm rejects ~ 90 percent of subhaloes, adopting this cut in R would return a heavily contaminated sample. We circumvent this problem by using our sphericity cut to determine the distribution of R for spurious subhaloes. For each WDM model, we take 10000 subsamples of 100 subhaloes that fail the sphericity cut (with replacement) and take the second highest R of each subsample to be the threshold, $R_{\rm min}$, below which subhaloes are spurious. This result is not sensitive to the size of our subsamples. The mean value of $R_{\rm min}$ across the 10000 subsamples is found to be in the range 0.94-0.96 for each of the four WDM models. For those subhaloes that instead pass the sphericity cut, the mean value of $R_{\rm min}$ is greater than 0.995 for all four models, showing that sphericity is a robust and accurate diagnostic of whether or not an object is spurious. We now couple the matching and sphericity criteria to determine the optimal cut in $M_{\rm Max}$. In Fig. 4.9, we plot s as a function of $M_{\rm Max}$ for the LRS subhaloes in each of our four WDM models, indicating their matching quality by colour. We adopt $R_{\rm min} = 0.94$. We restrict attention to subhaloes that pass the sphericity cut and take a mass limit $M_{\rm min} = \kappa M_{\rm lim}$ such that the number of subhaloes with mass greater than $M_{\rm min}$ is equal to the number of subhaloes with $R > R_{\rm min}$. In Fig. 4.9 this is equivalent to the number of red dots to the right of the mass cut being equal to the number of blue dots to the left. We find that this condition requires values of κ between 0.4 and 0.6, given the uncertainty in $R_{\rm min}$. For simplicity, we will adopt $\kappa = 0.5$; we find that this value provides a good compromise between rejecting low mass genuine objects and including high mass spurious subhaloes in all four models. Varying $R_{\rm min}$ and κ in the range stated here makes a difference of ~ 10 percent to the number of subhaloes returned in the $m_{1.4}$ model and ~ 5 percent in the other cases. The values of $M_{\rm min}$ are then $1.5 \times 10^8 {\rm M}_{\odot}$, $2.2 \times 10^8 {\rm M}_{\odot}$, $3.2 \times 10^8 {\rm M}_{\odot}$, and $4.2 \times 10^8 {\rm M}_{\odot}$ for the $m_{2.3}$, $m_{2.0}$, $m_{1.6}$, and $m_{1.4}$ models respectively in the low resolution simulations. For the high resolution simulations, they decrease to $5.1 \times 10^7 {\rm M}_{\odot}$, $7.0 \times 10^7 {\rm M}_{\odot}$, $1.1 \times 10^8 {\rm M}_{\odot}$, and $1.4 \times 10^8 {\rm M}_{\odot}$.

To summarise, we have used the mass, resolution dependant, and Lagrangian region

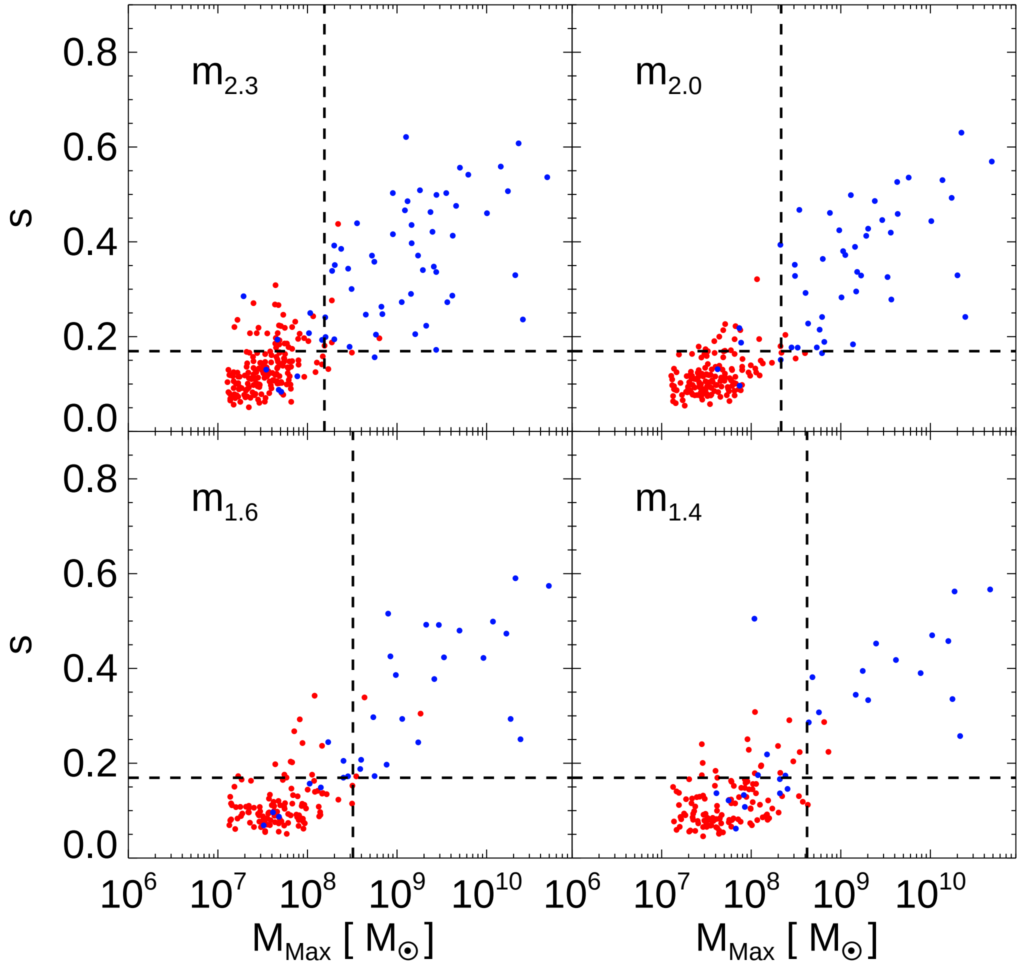

Figure 4.9: Dot plots of s and $M_{\rm Max}$ for subhaloes in the four different WDM models at low resolution. Blue points correspond to $R \geq 0.94$ and red points to $R < 0.94$. The horizontal, dashed line is $s_{\rm cut}$ and the vertical line is $M_{\rm min}$. All subhaloes are within r_{200b} of the main subhalo centre at redshift zero.

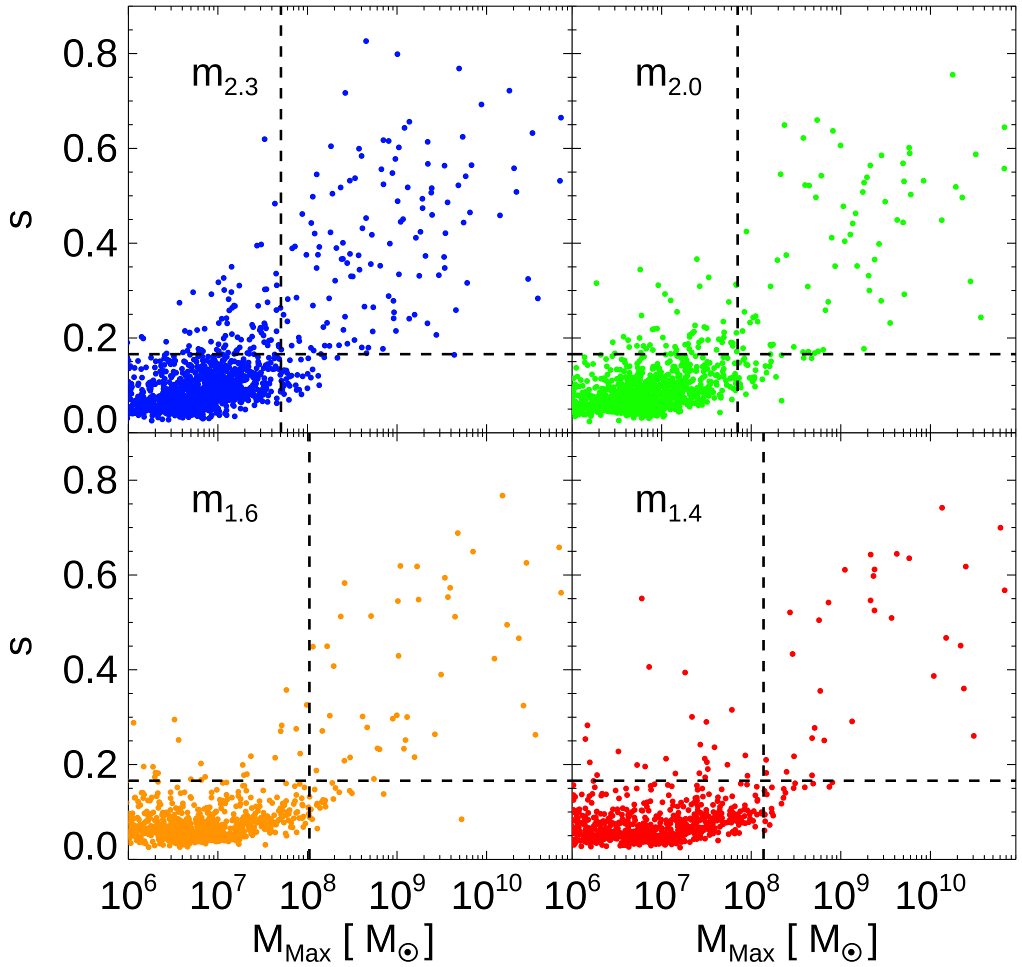

Figure 4.10: Dot plots of s and $M_{\rm Max}$ for subhaloes in the four different WDM models at high resolution. The horizontal, dashed line is $s_{\rm cut}$ and the vertical line is $M_{\rm min}$. All subhaloes are within r_{200b} of the main subhalo centre at redshift zero.

shape properties to identify spurious subhaloes in our subhalo catalogues. Having derived values for $s_{\rm cut}$ and $M_{\rm min}$ – the latter as a function of power spectrum cutoff and resolution – we can apply these cuts to the high resolution simulations. We plot the results in Fig. 4.10. Changing the value of κ in the range 0.4-0.6 produces a variation of < 5 percent in all four HRS models, and this does not affect our conclusions. In what follows we consider only those subhaloes that pass the cuts in each of these panels.

4.4 Results

4.4.1 The subhalo mass and $V_{\rm max}$ functions

In Fig. 4.11 we present the cumulative distributions of subhalo mass, $M_{\rm sub}$, and $V_{\rm max}$ at $z = 0$, where $V_{\rm max}$ is defined as the peak amplitude of the circular velocity profile $V_{\rm circ} = \sqrt{GM(< r)/r}$, with G the gravitational constant and $M(< r)$ the mass enclosed within radius r. This is a useful proxy for mass that is insensitive to the definition of the edge of the subhalo. The figure includes both genuine (solid lines) and spurious (dashed lines) subhaloes. Overall, the spurious subhaloes outnumber the genuine ones by a factor of 10. However, the mass function is dominated by genuine haloes beyond $M_{\rm sub} \sim (1-3)\times 10^7 {\rm M}_\odot$, corresponding to $V_{\rm max} \sim (4-6)$ kms^{-1} , for the different models. The differential mass function (relative to the CDM mass function) for genuine haloes in the $m_{2.3}$ case can be fit with the functional form given by Schneider et al. (2012):

$$n_{\rm WDM}/n_{\rm CDM} = (1 + M_{\rm hm} M^{-1})^{\beta}, \tag{4.7}$$

where $M_{\rm hm}$ is the mass associated with the scale at which the WDM matter power spectrum is suppressed by 50 per cent relative to the CDM power spectrum, M is subhalo mass and β is a free parameter. The best fit value is β of 1.3, slightly higher than the value of 1.16 found by Schneider et al. (2012) for friends-of-friends haloes (rather than SUBFIND subhaloes as in our case). A slightly better fit is obtained by introducing an additional parameter, γ, such that:

$$n_{\rm WDM}/n_{\rm CDM} = (1 + \gamma M_{\rm hm} M^{-1})^{\beta}, \tag{4.8}$$

with $\gamma = 2.7$ and $\beta = 0.99$. However, better statistics are required to probe the subhalo mass function more precisely. In principle, comparison of the abundance of subhaloes shown in Fig. 4.11 with the population of satellite galaxies observed in the Milky Way can set a strong constraint on the mass of viable warm dark matter particle candidates. Assuming that every satellite possesses its own dark matter halo and that the parent halo in our simulations has a mass comparable to that of the Milky Way halo, a minimum requirement is that the number of subhaloes in the simulations above some value of $M_{\rm sub}$ or $V_{\rm max}$ should exceed the number of Milky Way satellite above these values. In practice, the comparison is not straightforward because: *(i)* the values of $M_{\rm sub}$ or $V_{\rm max}$ for the observed population are not well known and *(ii)* the total number of Milky Way satellites is uncertain. Nevertheless, we can obtain a conservative limit on the mass of the particle as follows. There are 22 satellites in the Milky Way for which good quality kinematical data exist (Walker et al., 2009; Wolf et al., 2010). Eleven of these are "classical satellites" and the remainder are SDSS satellites. Of the classical satellites, eight are dwarf spheroidals and the others are the large and small Magellanic clouds (LMC and SMC) and Sagittarius. Wolf et al. (2010) have estimated values of the mass (and line-of-sight velocity dispersion, $\sigma^2_{\rm los}$) within the (deprojected 3D) half-light radius for the eight classical and 11 SDSS dwarf spheroidals. These are essentially insensitive to the velocity anisotropy of the stellar populations. The circular velocity within this radius is then given by:

$$V_{\rm circ}(r_{1/2}) = \sqrt{3\sigma^2_{\rm los}}. \tag{4.9}$$

The values of $V_{\rm circ}$ are lower limits to $V_{\rm max}$ for each satellite. Leo IV has the smallest circular velocity, $V_{\rm circ} = 5.7 \pm 2.9\ \ {\rm kms}^{-1}$, of the 22 studied by Wolf et al. (2010); it lies at a distance of 160 ± 15kpc from the Milky Way. We show in Appendix A.1 that our simulations have converged to better than 8% at this value of $V_{\rm max}$, showing that our conclusions are not affected by resolution issues (c.f. Polisensky and Ricotti, 2011). As shown by Springel et al. (2008b), values of $V_{\rm max}$ for subhaloes in Aquarius level 2 simulations are converged to within ~ 10 percent for $V_{\rm max} \geq 1.5\ \ {\rm kms}^{-1}$. We have examined the convergence in our $m_{2.3}$ model and find that our L3 and L2 resolution $V_{\rm max}$ functions are converged to within 2σ (Poisson) of each other for $V_{\rm max} > 4\ \ {\rm kms}^{-1}$. This is more modest than for the CDM Aquarius simulations, but sufficient to resolve the Leo IV type satellites. This result also gives us confidence that our ability to count satellites is not impaired by the numerical issues (c.f. Polisensky and Ricotti, 2011). The known number of satellites in the Milky Way halo, 22, is a lower limit to the total number within 280 kpc of the galaxy's centre, the distance to which the tip of the red giant branch can be detected in the SDSS. This is because although all the classical satellites (i.e. satellites brighter than $M_V = -11$) have probably been discovered, SDSS surveyed only 20 percent of the sky (DR5). Thus, a conservative lower limit to the WDM particle mass is obtained by requiring that the simulation should produce at least 22 satellites within this radius with $V_{\rm max} > 5.7\ \ {\rm kms}^{-1}$. Our $m_{1.4}$ simulation produced only 25 subhaloes with $V_{\rm max}$ greater than this value within the larger radius, $r_{200b} = 429$ kpc. Furthermore, the mass of the $m_{1.4}$ halo, $M_{200} = 1.80 \times 10^{12}\mathrm{M}_{\odot}$, is towards the higher end of acceptable values for the mass of the Milky halo; simulations of haloes with lower mass would produce even fewer subhaloes. Finally, any residual contamination by spurious subhaloes would artificially inflate the numbers in our subhalo sample. Thus, we can safely set a conservative lower limit to the mass of the WDM particle of $m_{\mathrm{WDM}} = 1.4$ keV. We can set a less conservative but still robust lower limit to m_{WDM} by correcting the observed number of SDSS satellites to take into account the area surveyed. A simple extrapolation multiplying the observed number by a factor of 5 has to be taken with caution because we know that the classical satellites are not distributed isotropically but are concentrated towards a plane, called the "Great pancake" by Libeskind et al. (2005). However, from analysis of the Aquarius simulations, Wang et al. (2012) have argued that such flat configurations occur only for the most massive ~ 10 subhaloes and the anisotropy of the distribution falls off rapidly with increasing sample size so that samples of ~ 50 subhaloes follow quite close the overall shape of the halo. Based on this, we do not make any corrections for anisotropy and conclude that the Milky Way contains at least $11 + 5 \times 11 = 66$ satellites with $V_{\max} > 5.7$ kms^{-1} within 280 kpc. Using the same argument as before, counting out to a radius of 419 kpc in the simulations to be conservative, we find that only the $m_{2.3}$ and CDM models produces enough satellites to satisfy the limit.

To make an estimate of the halo-to-halo scatter, we make use of the result of Boylan-Kolchin et al. (2010) that the intrinsic scatter in the abundance of CDM subhaloes, $\sigma_{\mathrm{scatter}}$, can be fit by the sum of the Poisson, σ_{P}^2, and intrinsic, σ_{I}^2, variances:

$$\sigma_{\mathrm{scatter}}^2 = \sigma_{\mathrm{P}}^2 + \sigma_{\mathrm{I}}^2, \tag{4.10}$$

where $\sigma_{\mathrm{P}}^2 = \langle N \rangle$ and $\sigma_{\mathrm{I}}^2 = s_{\mathrm{I}} \langle N \rangle^2$. Here, s_{I} is a constant, which Boylan-Kolchin et al. (2010) calibrate against their simulation results and thus obtain $s_{\mathrm{I}} = 0.18$. They also found that the probability distribution for the number of subhaloes N, given the mean $\langle N \rangle$ and intrinsic coefficient s_{I}, is well described by the Negative Binomial Distribution:

$$P(N|r,p) = \frac{\Gamma(N+r)}{\Gamma(r)\Gamma(N+1)} p^r (1-p)^N, \tag{4.11}$$

where $p = [1 + s_{\mathrm{I}}^2 \langle N \rangle]^{-1}$ and $r = s_{\mathrm{I}}^{-2}$. We then adopt the number of subhaloes within r_{200b} from each of our models as the distribution mean and compute the probability that a given halo will have at least 66 subhaloes. This probability equals 22% for $m_{2.0}$ and 0.30% for $m_{1.6}$. Therefore, we conclude on this evidence that $m_{\rm WDM} > 1.6$ keV. This is a more conservative limit than found by Polisensky and Ricotti (2011), although our choice of central halo is slightly more massive than theirs. A larger suite of WDM simulations is required to determine more precisely the variation in WDM subhalo abundance at a given host halo mass as well as the systematic variation of abundance with host halo mass.

4.4.2 The radial distribution of subhaloes

The number density of subhaloes of mass $M_{\rm sub} > 10^8 {\rm M}_\odot$ as a function of radius, normalized to the mean number density within r_{200b}, is shown in the top panel of Fig. 4.12. The bottom panel shows the cumulative number fraction of subhaloes per logarithmic radial interval. The number density profiles of subhaloes in the different WDM models are very similar to one another and to the CDM case. This uniformity is suprising since, as we shall see below, the central densities of WDM subhaloes decrease with decreasing WDM particle mass, making them increasingly vulnerable to tidal disruption. This result is reminiscent of that found by Springel et al. (2008a) that the number density profiles of Aquarius subhaloes are essentially independent of subhalo mass. It may be that better statistics might reveal differences in the radial distribution of WDM subhaloes.

The subhalo number density profiles are shallower than that of the halo dark matter. Springel et al. (2008a) found that the subhalo profiles are well described by an Einasto form (see Eqn. 4.13 below), with $r_{-2} = 199{\rm kpc} = 0.81 r_{200}$ and $\alpha_{\rm ein} = 0.678$. The lower panel of Fig. 4.12 shows that, as was the case for CDM, subhaloes lie preferentially in the outer parts of the halo, between 100 kpc and the virial radius, even though the number density is highest in the central regions.

The cumulative mass fraction in subhaloes as a function of radius is depicted in Fig. 4.13. As expected from the mass functions of Fig. 4.11, the subhalo mass fractions in the WDM models are lower than for CDM. At r_{200b}, the mass fractions in WDM subhaloes are approximately 5%, less than half the value in the CDM case. There is a small, but systematic decrease in the mass fraction with decreasing WDM particle mass.

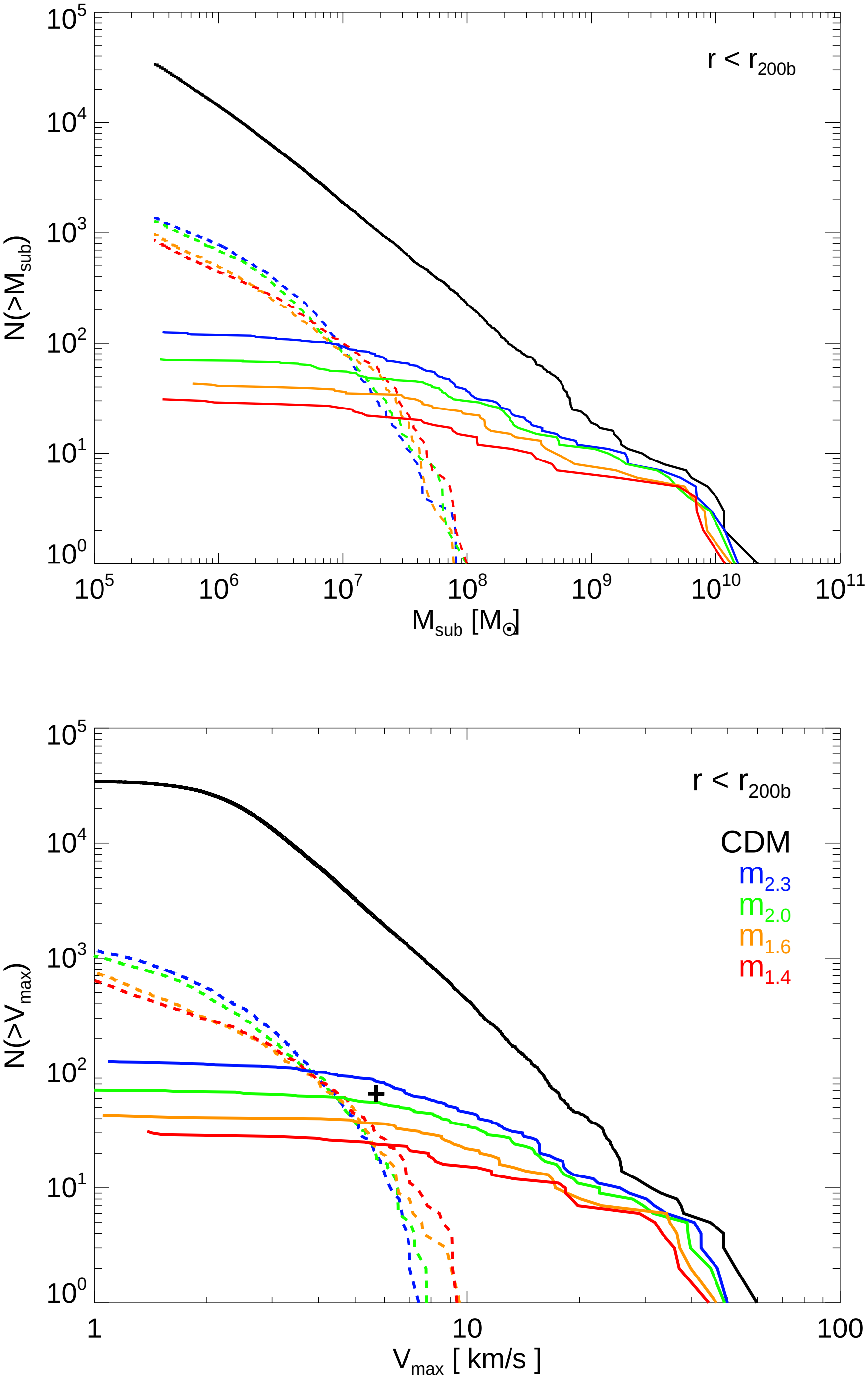

Figure 4.11: Cumulative subhalo mass, $M_{\rm sub}$, (*top panel*) and $V_{\rm max}$ (*bottom panel*) functions of subhaloes within $r < r_{200b}$ of the main halo centre in the high resolution simulations at $z = 0$. Solid lines correspond to genuine subhaloes and dashed lines to spurious subhaloes. The black line shows results for CDM-W7 and the colours lines for the WDM models, as in Fig. 4.1. The black cross in the lower panel indicates the expected number of satellites of $V_{\rm max} > 5.7$ kms^{-1} as derived in the text.

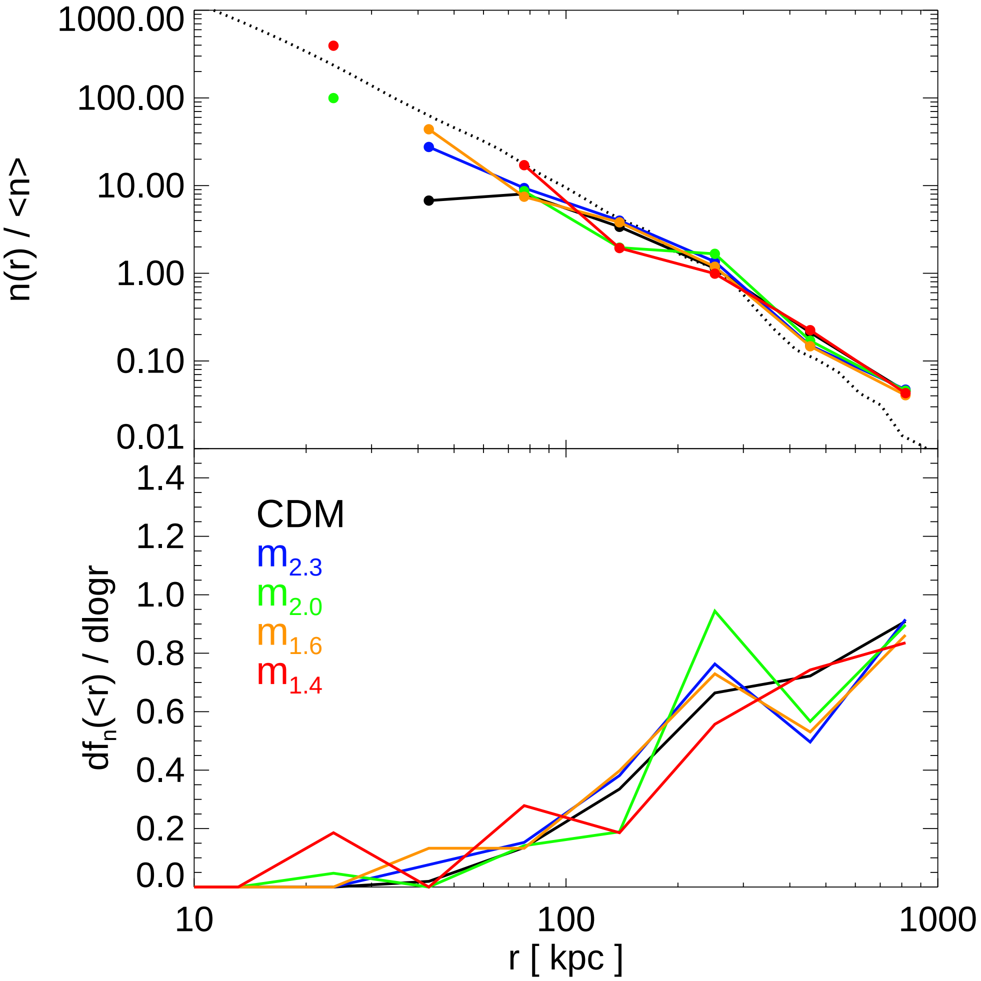

Figure 4.12: The radial distribution of subhaloes. *Top:* the spherically averaged number density of $M_{\rm sub} > 10^8 \rm M_\odot$ subhaloes normalised to the mean overdensity at r_{200b} for our four WDM and one CDM models. The dotted line indicates the CDM main halo density profile from Fig. 4.3, renormalised to pass through the locus of radial distribution points at 250kpc. *Bottom:* the number fraction of subhaloes per logarithmic interval in radius, on a linear-log plot. The area under the curves is proportional to subhalo number, so this plot shows that subhaloes are preferentially found in the outer parts of the halo. The black line corresponds to the CDM model, CDM-W7, while the blue, green, orange and red lines correspond to the $m_{2.3}$, $m_{2.0}$, $m_{1.6}$, and $m_{1.4}$ WDM models respectively.

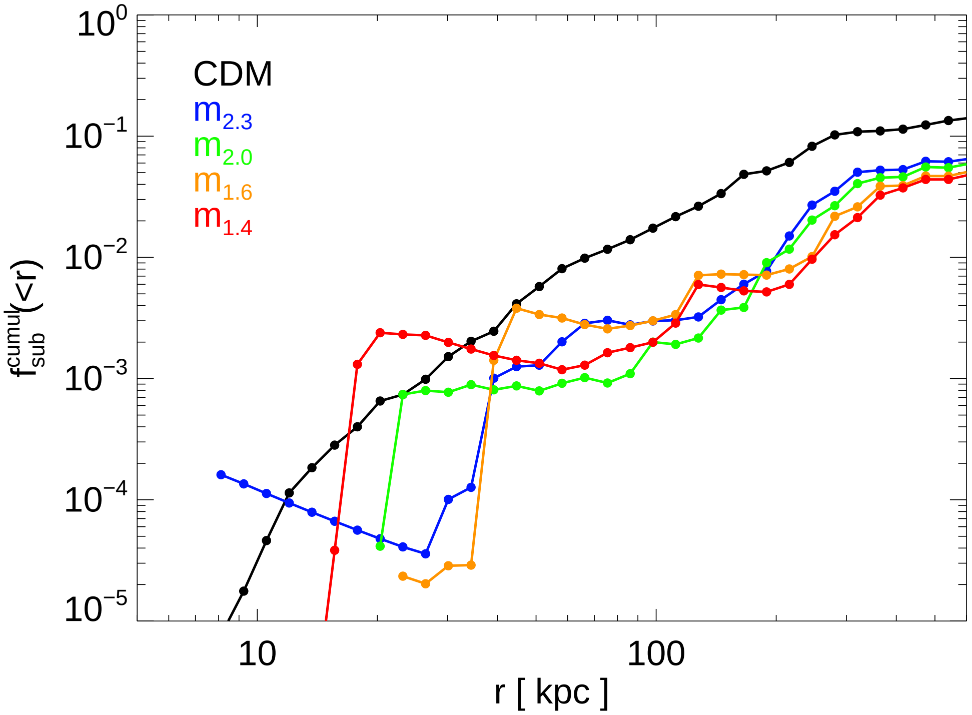

Figure 4.13: Cumulative mass fraction in substructures as a function of radius. The black line corresponds to the CDM model, CDM-W7, while the blue, green, orange and red lines correspond to the $m_{2.3}$, $m_{2.0}$, $m_{1.6}$, and $m_{1.4}$ WDM models respectively.

4.4.3 The internal structure of WDM subhaloes

We now consider the internal structure of WDM haloes, particularly their radial density profiles. We begin by performing a convergence test of the profiles.

Convergence of the density profiles

Springel et al. (2008a) carried out a careful study of the convergence properties of the CDM Aquarius haloes upon which our set of WDM halo simulations is patterned. Here we carry out an analogous study of the WDM subhaloes. We focus on the most extreme case, $m_{1.4}$, since this differs most from CDM. Fig. 4.14 shows the density profiles of the nine most massive subhaloes lying within 500 kpc in the $m_{1.4}$ simulation at three different resolutions (levels 2, 3 and 4). For the subhaloes of mass $> 1 \times 10^9 \mathrm{M}_\odot$, we find that the three realisations agree extremely well at all radii satisfying the convergence criterion of Power et al. (2003). For those of lower mass, the low resolution (level 4) examples have fewer that 10000 particles and although this limits the range where the convergence test is applicable, the convergence is still very good.

To emphasise the differences between subhaloes simulated at different resolution, we plot, in Fig. 4.15, the ratios of the intermediate and low resolution density profiles to that of their high resolution counterparts. At the smallest radius that satisfies the Power et al. (2003) criterion, the level 3 simulations are converged to better than 10%; in most cases the same is true of the level 4 simulations. There are large excursions, however, in the outer parts, beyond ~ 10 kpc. These are particularly noticeable for those subhaloes that are closer than 100 kpc from the main halo centre, and reflect the slightly different positions within the main halo of each of the matched subhaloes.

We can determine the mass range where the density profiles are converged by considering the ratio of circular velocities at the convergence radius of Power et al. (2003) between matched subhaloes at different resolution. Demanding that deviations from the level-2 simulation should not exceed 10%, we find that the structure of level-3 subhaloes is well converged for subhalo masses $> 10^8 \mathrm{M}_\odot$ whereas for level-4 subhaloes convergence is only achieved for masses $> 10^9 \mathrm{M}_\odot$.

The density profiles of subhaloes

We now consider the spherically averaged radial density profiles of subhaloes in all four different WDM models. For the CDM case Springel et al. (2008a) found that the profiles of subhaloes are well fit by either an NFW (Navarro et al., 1996c, 1997) or an Einasto (Einasto, 1965; Navarro et al., 2004) functional form. The NFW profile is given by:

$$\rho(r) = \frac{\delta_c \, \rho_{\mathrm{crit}}}{(r/r_s)(r/r_s+1)^2}, \tag{4.12}$$

where δ_c is a characteristic overdensity (usually expressed in units of the critical density) and r_s is a spatial scale that marks the transition between the asymptotic slopes of -1 and -3. The Einasto profile is given by:

$$\rho(r) = \rho_{-2} \exp\left(-\frac{2}{\alpha_{\mathrm{ein}}}\left[\left(\frac{r}{r_{-2}}\right)^{\alpha_{\mathrm{ein}}} - 1\right]\right), \tag{4.13}$$

where r_{-2} is the scale (analogous to r_s) where the profile attains a slope of -2, ρ_{-2} is the density at r_{-2} and α_{ein} is a shape parameter. Springel et al. find that Einasto fits

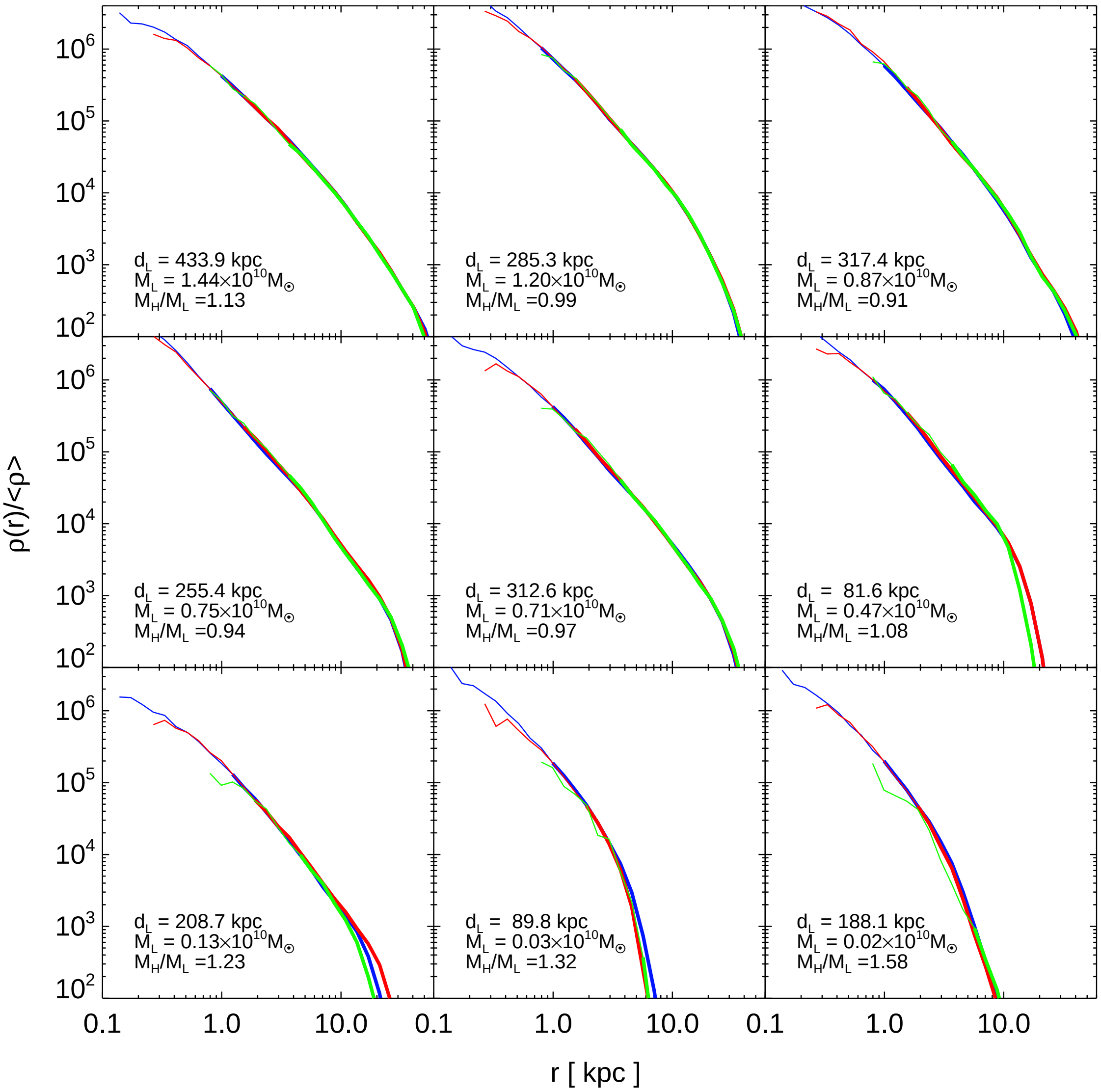

Figure 4.14: Spherically averaged radial density profiles for subhaloes matched between the high (level 2), intermediate (level 3), and low (level 4) resolution versions of the $m_{1.4}$ simulation. Blue corresponds to high, red to intermediate, and green to low resolution. The density profiles are shown by thick lines down to the smallest radius at which they satisfy the convergence criterion of Power et al. (2003), and are continued by thin lines down to a radius equal to twice the softening length. In the legend, d_L is the distance of the low resolution subhalo from the main halo centre, M_L is the subhalo mass, and M_L/M_H is the ratio between the masses of the low and high resolution counterparts.

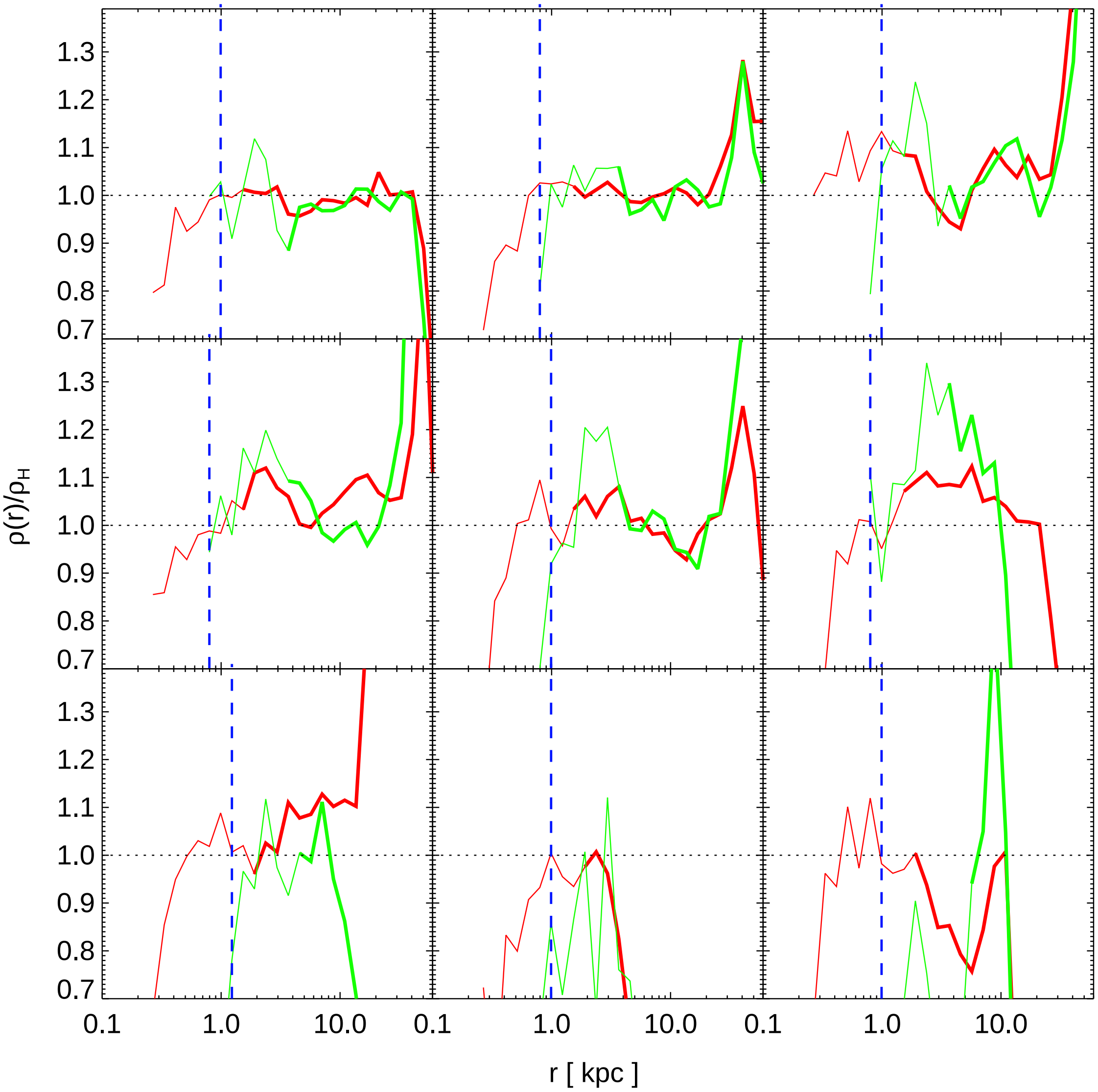

Figure 4.15: Ratio of the intermediate (level 3; red) and low (level 4; green) resolution density profiles of the $m_{1.4}$ subhaloes shown in Fig. 4.14 to the density profile of their high resolution (level 2) counterparts. The blue dashed line indicates the convergence radius for the high resolution subhaloes.

(which have an additional free parameter) are marginally better than NFW fits for CDM subhaloes even when $\alpha_{\rm ein}$ is fixed to a constant.

Following Springel et al. (2008a) we define a goodness of fit statistic for the functional fits to the subhalo profiles as:

$$Q^2 = \frac{1}{N_{\rm bins}} \sum_i [\ln \rho_i - \ln \rho^{\rm model}(r_i)]^2, \tag{4.14}$$

where ρ_i is the density measured at radius r_i, and ρ^{model} is the model density evaluated at that same radius. In Fig. 4.16 we show how well our subhaloes can be fit by NFW and Einasto profiles, in the latter case with fixed shape parameter ($\alpha_{\rm ein} = 0.18$, following Springel et al. 2008a), by plotting the median value of Q for each of the different models as a function of the thermal equivalent WDM particle mass. As for CDM, we find that the Einasto profile is a marginally better fit to WDM subhaloes than the NFW profile. There is little variation in the quality of the Einasto fits for the different values of the particle mass, but the NFW fits seem to become slightly worse with increasing mass.

The density profiles of subhaloes vary systematically with the WDM particle mass. Before performing a statistical comparison, we illustrate this variation with a few examples of subhaloes that we have been able to match across simulations with different WDM particle masses. Such matches are not trivial because the subhaloes have masses close to the cutoff in the intial power spectrum and thus their formation histories can vary substantially from one case to another. In Fig. 4.17 we show nine examples of subhaloes where, based on their positions and masses, we have been able to identify likely matches. In Fig. 4.18 we show the ratio of the profiles to that of their CDM counterpart.

The differences amongst the profiles tend, in most cases, to be larger at smaller radii. As the WDM particle mass decreases, the subhalo profiles tend to become shallower. At the innermost converged point, the density of the subhalo with the smallest value of $m_{\rm WDM}$ is generally a factor of several smaller than its CDM counterpart. For example, the $m_{1.4}$ keV subhalo in the central panel of the Figs. 4.17 and 4.18 is a factor of ~ 3 less dense at the innermost converged point than its CDM counterpart and a factor of ~ 2 less dense than the subhalo with $m_{2.3}$keV.

The trends seen in Figs 4.17 and 4.18 reflect the fact that, for fixed cosmological parameters, haloes of a given mass form later in WDM models than in CDM (Avila-Reese et al., 2001; Lovell et al., 2012). We can quantify the difference by comparing, for ex-

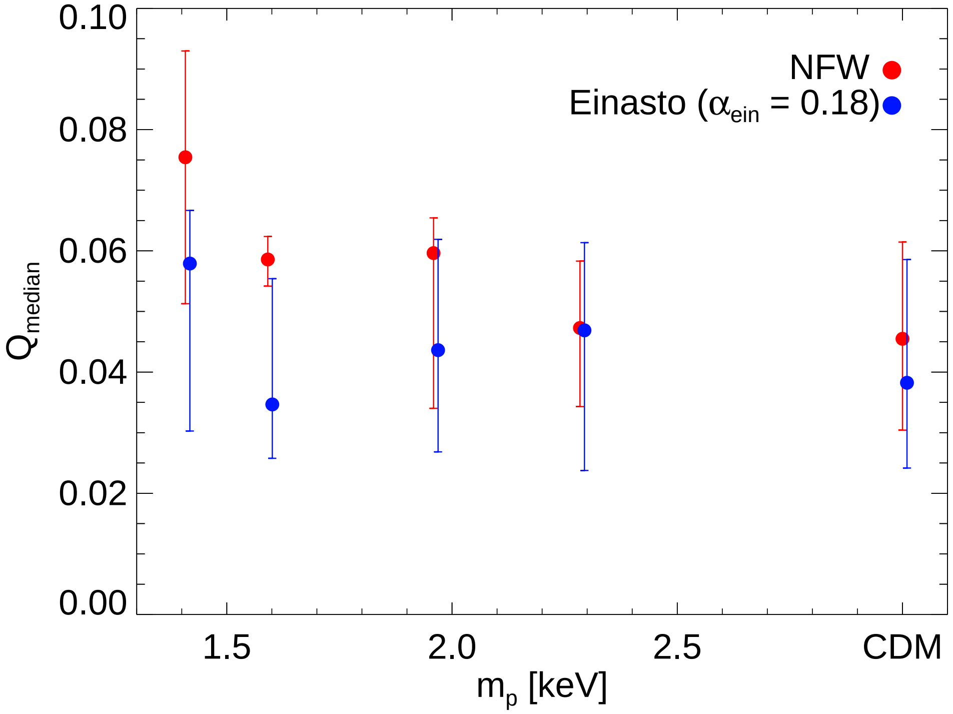

Figure 4.16: Median value of the goodness of fit statistic, Q, for Einasto (blue dots) and NFW (red dots) fits to all subhaloes of $M_{\rm sub} > 10^9 {\rm M}_{\odot}$, as a function of the WDM particle mass, $m_{\rm WDM}$. In the Einasto fits, we have fixed $\alpha_{\rm ein} = 0.18$. The error bars indicate the upper and lower quartiles of the distribution. The Einasto data points are slightly offset in $m_{\rm WDM}$ for clarity.

ample, the central masses of haloes in our various models. The masses enclosed within 300 pc and 2 kpc of the centre in field haloes and subhaloes in our simulations are plotted in Fig. 4.19 as a function of halo mass. For field haloes (left panel) there is a clear separation at both radii amongst the different models: at fixed mass, the WDM haloes have lower central masses than their CDM-W7 counterparts and the enclosed mass decreases with the WDM particle mass. For (field) haloes of mass less than $5 \times 10^9 {\rm M}_{\odot}$, the masses enclosed within 300pc are lower relative to the CDM case by factors of ~ 4 and $\sim$ 3 in the $m_{1.6}$ model and $m_{2.3}$ models respectively. At higher masses the differences are smaller (by factors of 2 and 3 for the $m_{2.3}$ and $m_{1.6}$ cases respectively), thus the main halo density profiles varies very little for this range of $m_{\rm WDM}$. The situation is somewhat different for subhaloes (right panel), largely because tidal stripping removes

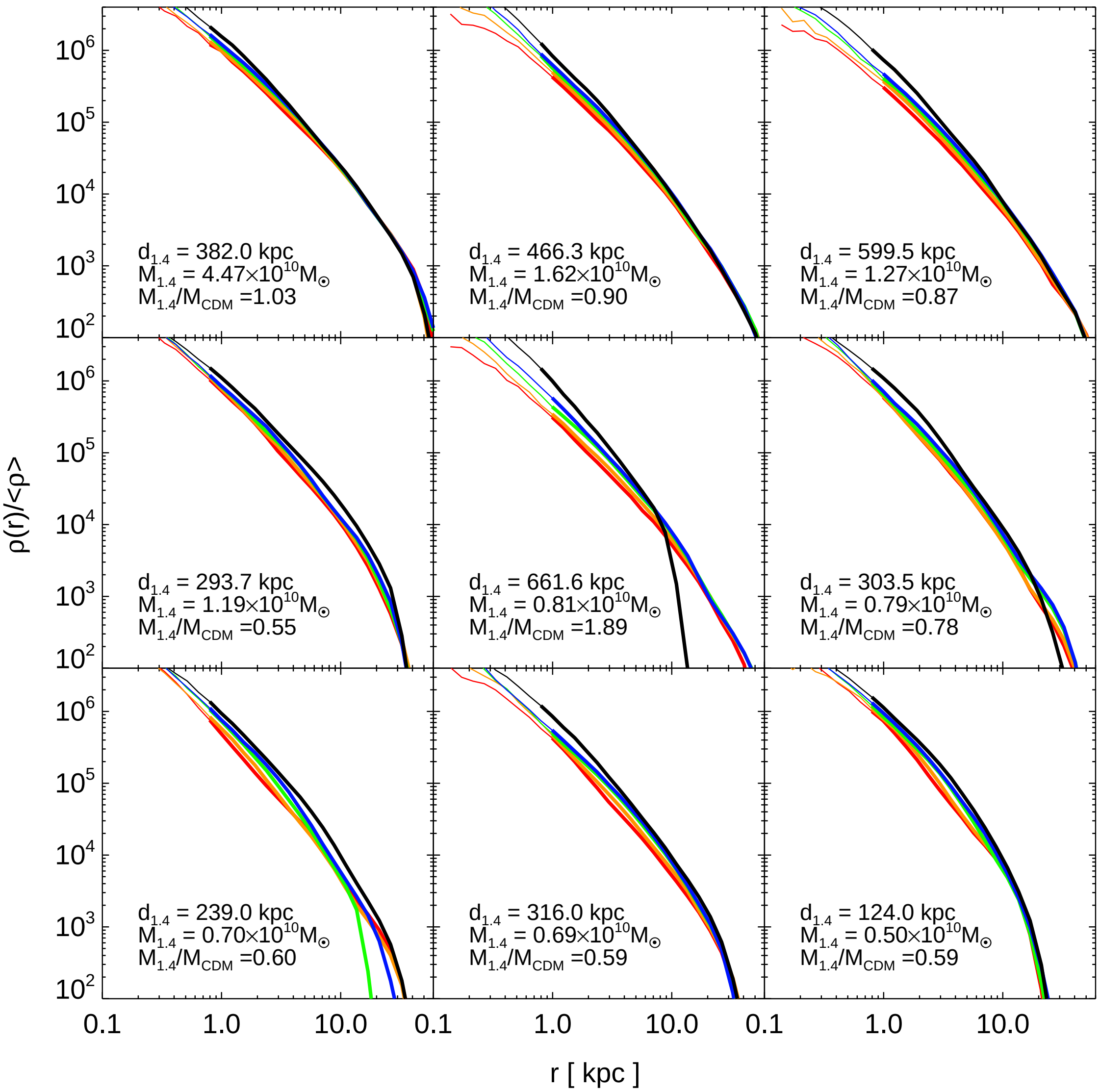

Figure 4.17: Spherically averaged radial density profiles of subhaloes in simulations of different WDM particle mass. The subhaloes have been matched across simulations on the basis of their position and mass. However, it should be noted that in some cases the matches are uncertain. The different colours correspond to different WDM particle masses: red, orange, green and blue to 1.4, 1.6, 2 and 2.3 keV respectively, while black corresponds to the CDM case. In the legend, $d_{1.4}$ is the distance of the subhalo from the main halo centre in the $m_{\rm WDM} = 1.4$keV, $M_{1.4}$ is the mass of the subhalo also in this case, and $M_{1,4}/M_{\rm CDM}$ is the ratio of this mass to that of the CDM counterpart. As in Fig. 4.14 the density profiles are shown by thick lines down to the smallest radius at which they satisfy the convergence criterion of Power et al. (2003), and are continued by thin lines down to a radius equal to twice the softening length

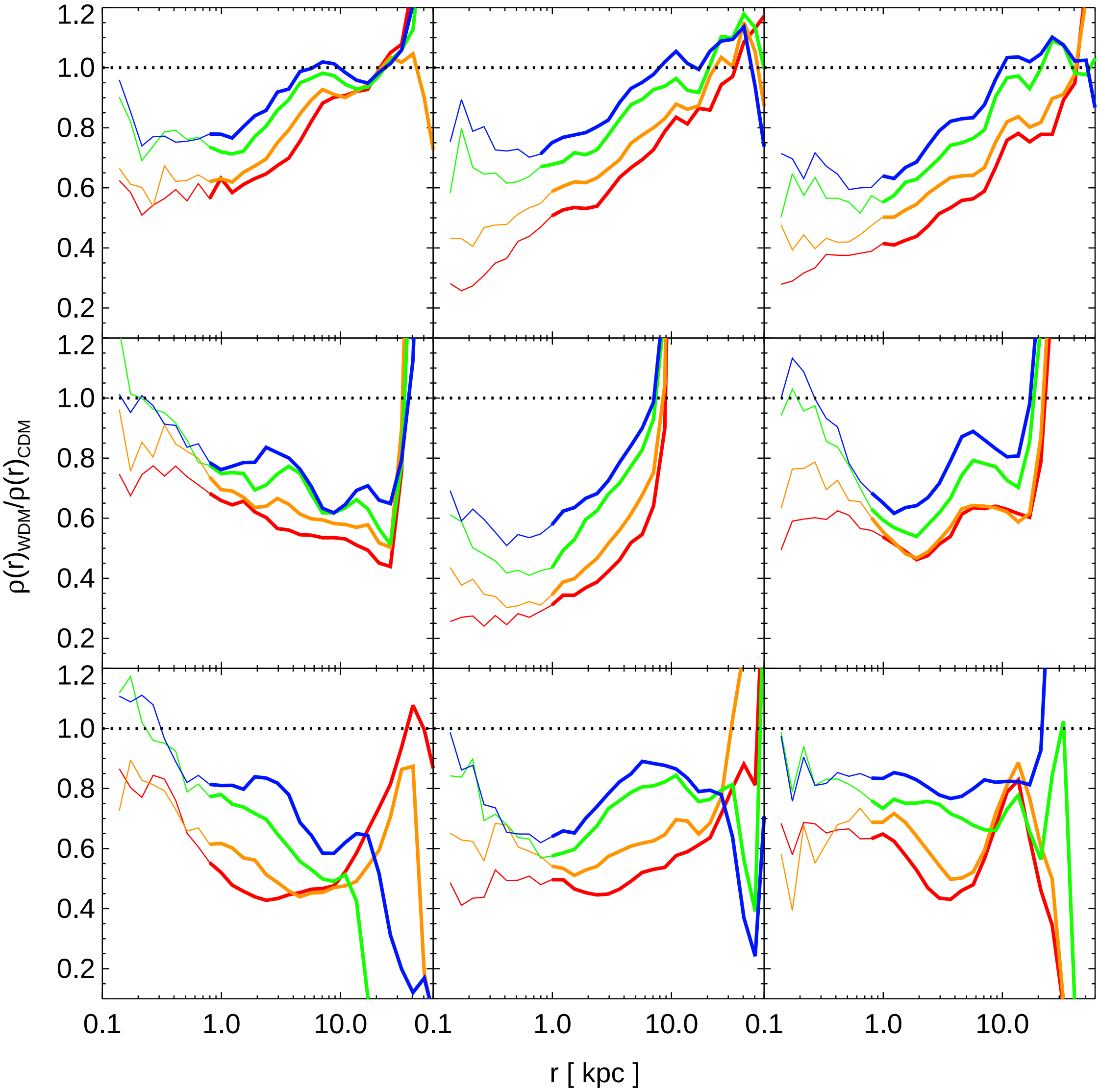

Figure 4.18: Ratio of the density profiles of matched subhaloes in simulations of different WDM particle mass relative to the mass of the CDM counterpart. The colours are as in Fig. 4.17 as is the use of thick and thin lines.

material from the outer regions, leaving the central density largely unaffected. As a result, after falling into their host halo, objects move primarily to the left in Fig. 4.19 but the change is comparatively greater for the less concentrated WDM subhaloes than for the CDM subhaloes. Nevertheless, an offset amongst the WDM subhaloes and amongst these and the CDM subhaloes remains, particularly at large masses.

Another measure of central mass is provided by the value of $V_{\rm max}$ which we plot as a function of mass for field haloes in Fig. 4.20. There is a marked difference between the CDM-W7 and the WDM haloes which, at a given mass, have a lower $V_{\rm max}$. As expected, these differences decrease with increasing halo mass. At $10^9{\rm M}_\odot$ the mean value of $V_{\rm max}$ for the $m_{2.3}$ case is a factor of 1.33 smaller than for CDM-W7.

The differences in the internal structure of haloes in the WDM and CDM cases can be further quantified by comparing the relation between $V_{\rm max}$ and $r_{\rm max}$, the radius at which $V_{\rm max}$ is attained. We plot these relations separately for independent haloes and subhaloes in Fig. 4.21. Tidal stripping of CDM subhaloes causes their value of $V_{\rm max}$ to drop less rapidly than their value of $r_{\rm max}$, leading to an increase in the concentration of the subhalo (Peñarrubia et al., 2008; Springel et al., 2008a). As may be seen by comparing the top and bottom panels of Fig. 4.21, the values of $r_{\rm max}$ for CDM subhaloes at fixed $V_{\rm max}$ are typically 70 per cent of the values for field haloes [1]. Since WDM subhaloes are less concentrated than their CDM counterparts to begin with, they are more susceptible to stripping once they become subhaloes (see also Knebe et al., 2002). Thus, at fixed $V_{\rm max}$, the values of $r_{\rm max}$ in the $m_{2.3}$ case are now typically only 40 per cent of the values for field haloes. Even so, since the typical values of $r_{\rm max}$ for subhaloes with $V_{\rm max} > 10$ km/s are greater than $1{\rm kpc}$ (even in the models with the smallest WDM particle mass), the majority of any dSphs residing in subhaloes like these would not show clear signs of tidal disruption.

4.4.4 The abundance of the most massive subhaloes

Boylan-Kolchin et al. (2011, 2012) showed that the most massive subhaloes in the Aquarius halo simulations are much too massive and concentrated to host the brightest dSph satellites of the Milky Way. Parry et al. (2012) reached the same conclusion using gasdynamic simulations of the Aquarius haloes. This discrepancy was called the "too big to fail problem" by Boylan-Kolchin et al. Subsequently Wang et al. (2012) showed that the extent of the discrepancy depends strongly on the mass of the Galactic halo and all but disappears if the Milky Way's halo has a mass of $1 \times 10^{12}\mathrm{M}_{\odot}$,. Alternatively, Lovell et al. (2012) showed the the problem is naturally solved in a WDM model even if the mass of the Galactic halo is $2 \times 10^{12}\mathrm{M}_{\odot}$. Their WDM model, chosen to have a particle mass only just compatible with the Lyman-α constraints of Boyarsky et al. (2009a,b) (but not with the more recent constraint quoted by Viel et al. 2013b) is the $m_{1.4}$ model of the current study.

---

[1] This number depends on the choice of cosmological parameters. For the Aquarius simulations (which assumed WMAP1 cosmological parameters), this number decreases to 62 per cent (Springel et al., 2008a), as can be seen by comparing the dotted lines in the two panels of Fig. 4.20. This difference is driven primarily by the higher value of σ_8 in the WMAP1 cosmology which causes haloes of a given mass to collapse earlier and thus be more concentrated than their WMAP7 counterparts.

The Milky Way contains three satellites, the LMC, SMC and Sagittarius, that are brighter than the brightest dSph, Fornax. The "too big to fail problem" consists of having substantially more than three massive subhaloes within 300 kpc in the simulations whose properties are incompatible with the measured kinematics of the nine brightest dSphs, specifically with the measured masses within their half-light radii (where masses can be robustly measured from the data; Walker et al. 2009; Wolf et al. 2010). In our WDM simulations we thus count the number of subhaloes within 300 kpc of the main halo centre that have circular velocity profiles of amplitude greater than the measured half-light circular velocities of the 9 brightest dSphs plus their 3σ errors (Walker et al., 2009; Wolf et al., 2010; Lovell et al., 2012). We find 1, 1, 3 and 4 subhaloes in the $m_{1.4}$, $m_{1.6}$, $m_{2.0}$ and $m_{2.3}$ WDM models respectively and 6 in CDM-W7. Thus, all our WDM simulations are free of the "too big to fail problem" even in a $2 \times 10^{12}\mathrm{M}_{\odot}$ Galactic halo. Note that if we knew the mass of the Milky Way halo precisely, this argument could, in principle, be used to set an *upper limit* on the (thermal) WDM particle mass.

4.5 Discussion and conclusions

Although the existence of dark matter was inferred in the 1930s, its identity remains one of the most fundamental unsolved questions in physics. The evidence points towards dark matter being made of as yet undiscovered elementary particles. Over the past thirty years attention has focused on cold dark matter (Peebles, 1982; Davis et al., 1985; Bardeen

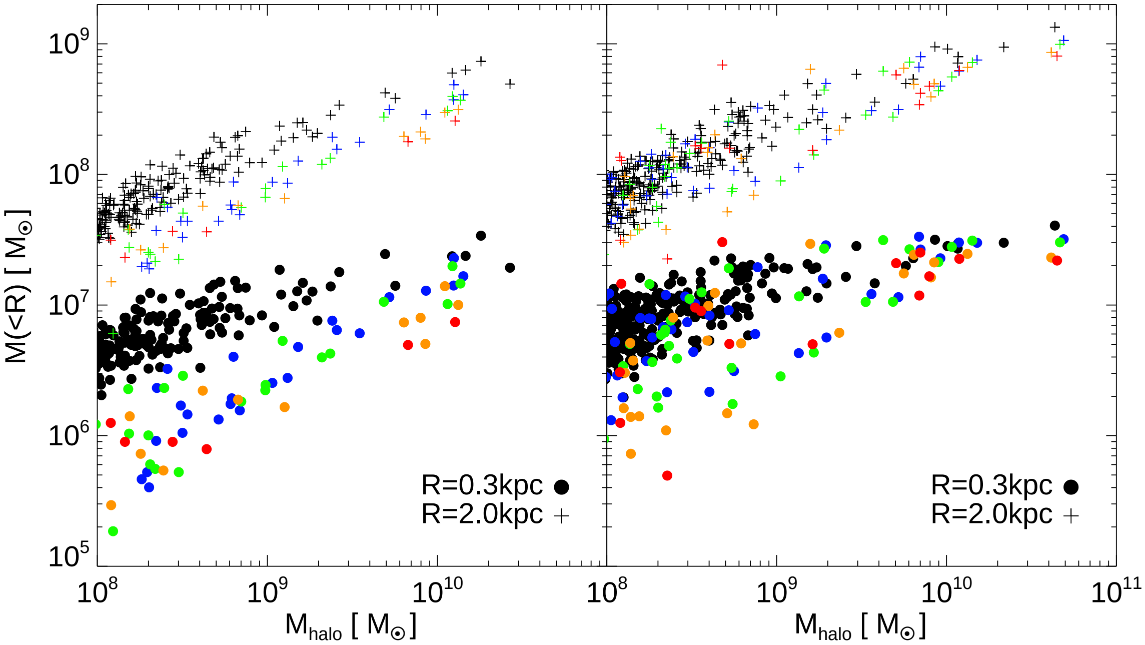

Figure 4.19: Central masses of field haloes (left) and subhaloes within r_{200b} (right), evaluated within radii of 2 kpc (crosses) and 300pc (circles) as a function of total mass. Different colours correspond to different simulations: black for CDM-W7, blue, green, orange and red for models $m_{2.3}$, $m_{2.0}$, $m_{1.6}$, and $m_{1.4}$ respectively.

et al., 1986) but this is not the only possibility. For example, the lightest sterile neutrino in the νMSM model (Asaka and Shaposhnikov, 2005) would behave as warm dark matter, generating very similar structures to CDM on scales larger than bright galaxies but very different structures on smaller scales (Lovell et al., 2012; Macciò et al., 2012; Schneider et al., 2012).

In this study we have carried out a series of high resolution N-body simulations of galactic haloes in universes dominated by WDM, taking as the starting point one of the haloes from the Aquarius project of simulations of CDM galactic haloes carried out by the Virgo Consortium (“Aq-A” in Springel et al., 2008a). As a prelude we resimulated this CDM halo replacing the cosmological parameters from the WMAP year-1 values assumed by Springel et al. to the WMAP year-7 values (Komatsu et al., 2011). For CDM this change has the effect of lowering the central densities of galactic subhaloes, alleviating (but not eliminating) the tension between the structure of CDM subhaloes orbiting in haloes of mass $\sim 2 \times 10^{12}\mathrm{M}_{\odot}$ and the kinematical data for Milky Way satellites (Boylan-

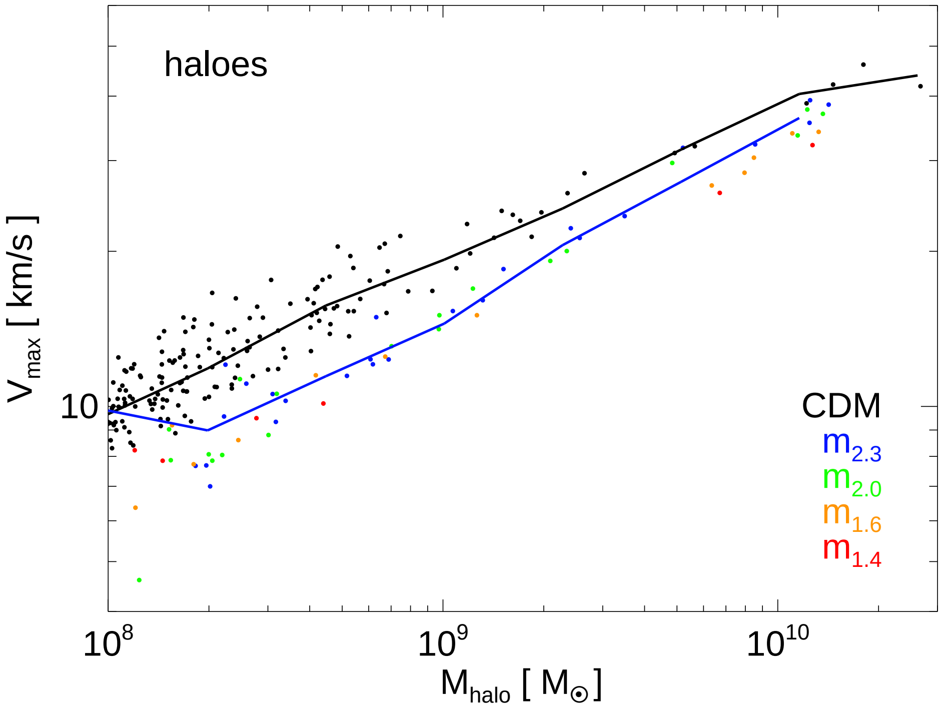

Figure 4.20: $M_{\rm halo}$ vs. $V_{\rm max}$ for field haloes. The black dots show the data for the CDM-W7 simulation and the black line represents the mean relation. The colour dots show data for the WDM simulations: blue, green, orange and red for models $m_{2.3}$, $m_{2.0}$, $m_{1.6}$, and $m_{1.4}$ respectively. The mean relation is shown only for the $m_{2.3}$ WDM model in which the number of subhaloes is largest and thus the least noisy.

Kolchin et al., 2012; Wang et al., 2012). We then performed a series of simulations of WDM haloes, using as initial conditions the same fluctuation phases and linear power spectrum of Aq-A, suitably truncated to represent WDM with (thermal equivalent) particle masses in the range 1.4 keV to 2.3 keV. Our main simulations correspond to level-2 resolution in the notation of Springel et al. (2008a), but we also ran simulations at lower resolution to establish convergence.

N-Body simulations with a resolved cutoff in the initial power spectrum undergo artificial fragmentation in filaments (Bode et al., 2001; Wang and White, 2007). The resulting spurious structures need to be identified before the simulations can be analyzed. This is best done in the initial conditions: we found that the spurious fragments evolve from disc-like structures that are much flatter than the progenitors of genuine haloes.

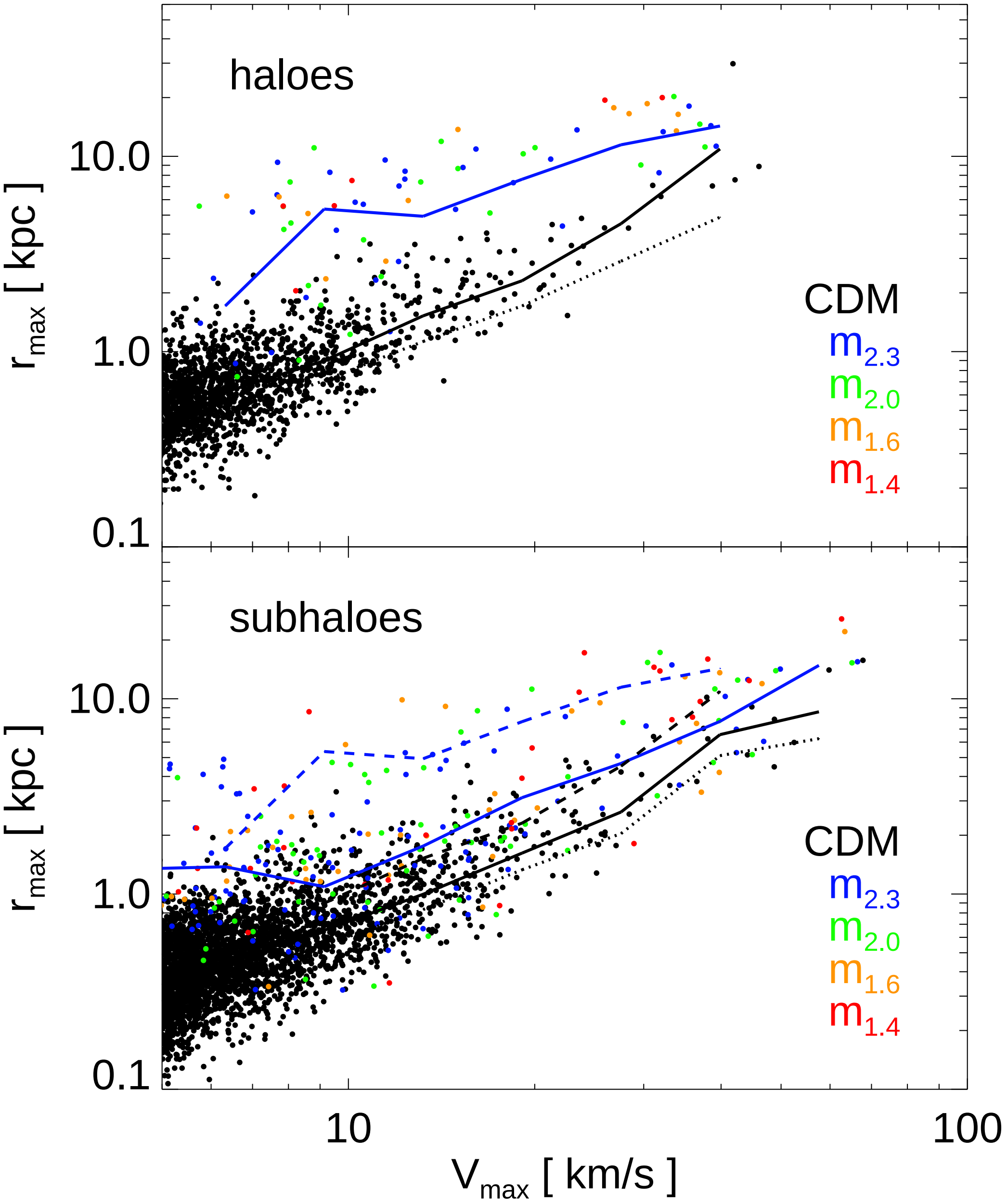

Figure 4.21: $V_{\rm max}$ vs. $r_{\rm max}$ for independent haloes (top) and subhaloes (bottom). The black dots show the data for the CDM-W7 simulation and the black line represents the mean relation in the case. The dotted line corresponds to a ΛCDM simulation using the WMAP1 cosmological parameters. The colour dots show data for the WDM simulations: blue, green, orange and red for models $m_{2.3}$, $m_{2.0}$, $m_{1.6}$, and $m_{1.4}$ respectively. The mean relation is shown only for the $m_{2.3}$ WDM model in which the number of subhaloes is largest and thus the least noisy. The solid lines of the top panel are reproduced in the bottom panel as dashed lines.

The sphericity of structures in the initial conditions therefore provides a robust flag for spurious objects which we supplement with a mass cut, $M_{\rm min}$, derived from the limiting mass for genuine haloes, $M_{\rm lim}$, inferred by Wang and White (2007) from simulations of hot dark matter models. We find that a cut of $M_{\rm min} = \kappa M_{\rm lim}$, with $\kappa = 0.5$, captures the results from a comparison of matched haloes in simulations of different resolution. The combined sphericity and mass cut criteria result in clean catalogues of genuine haloes and subhaloes.

The spherically averaged density profile of the main halo is virtually indistinguishable in the CDM and all our WDM simulations but there are large differences in the abundance and structure of their subhaloes. For WDM, the subhalo mass functions begin to diverge from the CDM case at masses between $\sim 2 \times 10^9 {\rm M}_\odot$ for the $m_{2.3}$ (least extreme) and $\sim 7 \times 10^9 {\rm M}_\odot$ for the $m_{1.4}$ (most extreme) models. The cumulative mass functions are well fit by fitting functions given in §4.4.1: they become essentially flat for subhaloes masses below $\sim 7 \times 10^9 {\rm M}_\odot$. The mass fraction in substructures within r_{200b} is lower than in the CDM case by factors between 2.4 (for $m_{1.4}$) and 2 ($m_{2.3}$). The radial distributions of subhaloes are very similar to the CDM case.

WDM haloes and subhaloes are cuspy (except in the very inner regions - see Macciò et al. (2012) and Shao et al. (2013)) and are well fit by NFW profiles, and even better by Einasto profiles. However, the central density of WDM haloes depends on the WDM particle mass: in those cases where it is possible to identify the same subhalo in CDM and different WDM simulations, the density profiles have systematically shallower slopes in the latter which become flatter for smaller particle masses. This change of slope is reflected in the main halo mass, $M_{\rm host} - M_{\rm sub}$, $M_{\rm sub}{-}V_{\rm max}$, and $V_{\rm max}$ $-r_{\rm max}$ relations, such that, for a given mass, subhaloes in warmer dark matter models have progressively lower central densities, lower values of $V_{\rm max}$ and higher values of $r_{\rm max}$ relative to CDM subhaloes. These differences affect the evolution of subhaloes once they fall into the main halo since less concentrated haloes are more easily stripped.

Both the abundance and the structure of WDM subhaloes can be compared to observational data. The requirement that the models should produce at least as many subhaloes as there are observed satellites in the Milky Way sets a lower limit to the WDM particle mass. This is a very conservative limit since feedback processes, arising from the reionization of gas in the early universe and supernova energy, would prevent the formation of galaxies in small mass haloes just as they do in CDM models (e.g. Benson et al., 2002). However, the number of subhaloes above a given mass or $V_{\rm max}$ depends, of course, on the host halo mass (Gao et al., 2004; Wang et al., 2012). For the case we have considered, in which $M_{\rm host} \sim 10^{12}{\rm M}_{\odot}$, we find that the WDM particle mass must be greater than 1.4 keV or 1.6 keV depending on whether we simply consider the observed number of satellites or apply a correction for the limited area surveyed by the SDSS. This limit is less stringent than that limit of 3.3 keV (2σ) inferred by Viel et al. (2013b) from the clumpiness of the Lyman-α forest of a sample of quasars at redshift $z > 4$, although the two results are not directly comparable because Viel et al. (2013b) use a slightly different transfer function. In principle it might also be possible to set an upper limit on the WDM particle mass by comparing the subhalo central densities with those inferred for the brightest satellites of galaxies like the Milky Way. Current kinematical data are insufficient for this test but they are compatible with the properties of the most massive subhaloes in the four WDM models we have considered none of which suffers from the 'too big to fail' problem highlighted by Boylan-Kolchin et al. (2012).

WDM remains a viable alternative to CDM, along with other possibilities such as self-interacting dark matter (Vogelsberger et al., 2012) and cold-plus-warm mixtures (Anderhalden et al., 2013). Further theoretical work, including simulations and semi-analytical calculations (Kennedy et al, in prep., Benson et al., 2013) combined with better data for dwarf galaxies offer the prospect of ruling out or validating these models.

Chapter 5

The epoch of reionisation in warm dark matter

5.1 Introduction

In Chapters 3 and 4, we have shown that the suppression of small scale power prevents the smallest subhaloes from forming and also delays the formation of those structures that do form. These factors in unison will affect the number of stars present in the early Universe, and so we can seek to constrain our WDM models with applications of this fact. One such constraint is provided by the epoch of reionisation (EoR). The recent Planck results (Planck Collaboration et al., 2013b) have offered excellent constraints on precisely when the Universe became ionised by examining the effect that Thomson scattering from the newly-released electrons had on the CMB. For a combination of Planck and WMAP polarisation data, plus the assumption that the transition between a fully neutral and a fully ionized IGM may be modelled as a step function in time, they determine that the EoR occured at $z_{\rm re} = 11.1 \pm 1.1$: any model of cosmology and galaxy formation will be required to match this constraint.

In the standard reionisation paradigm, sufficiently energetic UV photons generated by young stars in the earliest galaxies enter the inter-galactic medium (IGM) and dissociate the electrons from the protons in neutral hydrogen atoms, thus converting atomic hydrogen to the ionised variety. For a given temperature and density, the now-free protons and electrons have a finite opportunity to recombine, thus on the macro scale there is a recombination rate working against the UV photons. To be considered an accurate description of the Universe, any astrophysical model must be able to generate enough UV photons to at least reionise each IGM hydrogen atom once, and quite possibly more so given the recombination effect. This constraint is a direct test of WDM: if the WDM particle mass for a given WDM model is too low, the number of structures present in the early Universe will be too few and also form too late to effect reionisation within the required time frame. This problem has been examined analytically by Barkana et al. (2001) and Yue and Chen (2012), who used the extended Press-Schechter formulism (Press and Schechter, 1974; Bond et al., 1991) and reionisation bubbles to set lower limits to the WDM particle mass of 0.5keV and 1.3keV respectively.

In this Chapter we examine the effect of WDM on reionisation using hydrodynamic simulations of a Milky Way-analogue halo using both CDM and an extreme WDM model. Simulations that make use of cooling and star-formation alone produce galaxies that are far more luminous than those observed, and so introduce mechanisms such as supernova to regulate star-formation in small galaxies and AGN feedback in larger systems (e.g. Springel and Hernquist, 2003; Bower et al., 2006). If we wish to place conservative limits on the WDM particle mass, however, we may use one of these otherwise unfeasible models to set an upper limit on the number of ionising photons generated within the simulation volume in a given model.

A full reionisation calculation along the lines of e.g. Benson et al. (2001); Iliev et al. (2011) is beyond the scope of this Chapter; we instead take a simpler approach. We study the likely impact of WDM on the local group by comparing full hydrodynamic gas runs of the CDM and WDM haloes used in Chapters 3 and 4, and compare the number of ionising photons generated to the number of hydrogen atoms to be ionised. This Chapter is arranged as follows. In section 5.2 we describe our simulations and the gas hydrodynamics model, in section 5.3 we present our results, and draw conclusions in section 5.4.

5.2 The simulations

The analysis was performed on a suite of four gas-hydrodynamic simulations that were run with the P-GADGET3 SPH code (Springel et al., 2008a). Each was run using the set of WMAP 1 year cosmological parameters: $\Omega_\Lambda = 0.75$, $\Omega_0 = 0.25$, $\Omega_b = 0.045$, $h = 0.73$, $n_s = 0.99$, and $\sigma_8 = 0.9$. The particle load is taken from the zoomed-simulation Aq-A halo of the Aquarius project (Springel et al., 2008a), a suite of dark matter only simulations. The box as a whole is $100h^{-1}\mathrm{Mpc}$ on a side, and the high resolution region is approximately $8h^{-1}\mathrm{Mpc}$ across. We generate our initial conditions by splitting each Aq-A dark matter particle into a pair of dark matter and gas particles. The dark matter particles each have a mass of $3.22 \times 10^{5}\mathrm{M}_{\odot}$ and the gas particles an initial mass of $7.07 \times 10^{4}\mathrm{M}_{\odot}$. All four utilised the hybrid-SPH particle model of (Springel and Hernquist, 2003), in which each SPH gas particle is considered to represent locally cold clouds and the ambient hot phase. Gas particles are able to form two generations of star particles and are then removed from the simulation. We use a Salpeter IMF (Salpeter, 1955) to determine the thermal heating of the ISM due to supernova, and extract luminosities/UV fluxes for our star particles from the SSP models of Bruzual and Charlot (2003). This simple model does not track the metallicities of the stars, we therefore make the assumption that every star particle formed is 'Population II' SSP with a metallicity of [Fe/H]=-2.25. This is the lowest metallicity option available in the Bruzual & Charlot tables, and will therefore return the maximum ionising photon counts and thus the most conservative constraints.

Two of our four simulations also feature the supernova winds model of Springel and Hernquist (2003). Gas particles found in the vicinity of a newly-created star particle have a finite probability of entering the supernova wind. Should it be selected, it is given an additional velocity component in the direction of its velocity-acceleration cross product (positive or negative at random) as an approximation to the local stellar system minor axis, and designated as a wind particle for a period of time determined by the efficiency of supernova feedback and other parameters (see Springel and Hernquist, 2003). During this period the particle is prohibited artificially from interacting hydrodynamically with neighbouring gas particles (thus they are known as 'decoupled-winds'), however it is permitted to cool.

The four simulations differ in their application of supernova feedback and dark matter physics. We have two cold dark matter runs, one of which has the supernova winds model switched on and the second not: these are labelled as 'CW' and 'CN'. A corresponding pair of winds and no-winds runs was performed using a warm dark matter power spectrum, thus 'WW' and 'WN'. The WDM model used is the same as that in Lovell et al. (2012), a 1.4keV thermal relic particle with the same WDM transfer function used in Chapter 3. This model is the most extreme permitted at 2σ by the Lyman-α forest analysis of Boyarsky et al. (2009a,b). It has since been ruled out by the subsequent study

Name	M_{200} [$\mathrm{M}_\odot$]	r_{200} [kpc]	M_{stellar} [$\mathrm{M}_\odot$]
CD	1.84×10^{12}	245.7	N/A
WD	1.78×10^{12}	243.0	N/A
CN	1.71×10^{12}	239.8	1.19×10^{11}
WN	1.68×10^{12}	238.4	1.33×10^{11}
CW	1.59×10^{12}	234.1	8.16×10^{10}
WW	1.53×10^{12}	231.4	9.33×10^{10}

Table 5.1: Parameters of the central galaxies and their haloes generated in each simulation. r_{200} is defined as the radius enclosing the spherical overdensity 200 times the critical density of the Universe, M_{200} is the mass within that radius, and M_{stellar} the stellar mass of the galaxy as defined in the text.

of Viel et al. (2013a), but is still informative on the likely effect of WDM on galaxy formation. At present no convergence studies for any of the calculations we perform in this Chapter using these simulations, and this sort of an analysis will be required in future.

This halo was originally chosen for resimulation as its mass and environment made it a good candidate to host a Milky Way-like galaxy. In Table 5.1 we state the properties of each of our galaxies and their host friends-of-friends dark matter haloes (Davis et al., 1985). We define our host halo virial radius r_{200} as the radius containing a spherical overdensity 200 times that of the critical density, and virial mass M_{200} that within r_{200}. In assigning stellar masses, M_{stellar} to the a Milky Way-like L_* galaxies we follow the definition of Scannapieco et al. (2012): this is the total mass in star particles within $0.1 \times r_{200}$ of the halo's baryonic centre-of-potential. We also show the values of M_{200} and r_{200} for the original dark matter-only versions of these runs (CD for CDM, WD for WDM).

The inclusion of cooling, star-formation and winds alters the halo masses by 15 per cent and radii by 5 per cent in both CDM and WDM, such that the baryonic physics is dominant over the dark matter type. The stellar mass and halo virial mass for the preferred winds models are higher than those inferred for the Milky Way by (McMillan, 2011) – $M_{200} = 1.26 \pm 0.24 \times 10^{12} \mathrm{M}_\odot$, $M_{\mathrm{stellar}} = 6.43 \pm 0.63 \times 10^{10} \mathrm{M}_\odot$ – and discrepant from the abundance matching relation of Guo et al. (2010), however with these mass values our galaxies are not dissimilar to those of the Aquila Project (Scannapieco et al., 2012), and we therefore have confidence that this simulation volume is a a viable candidate for

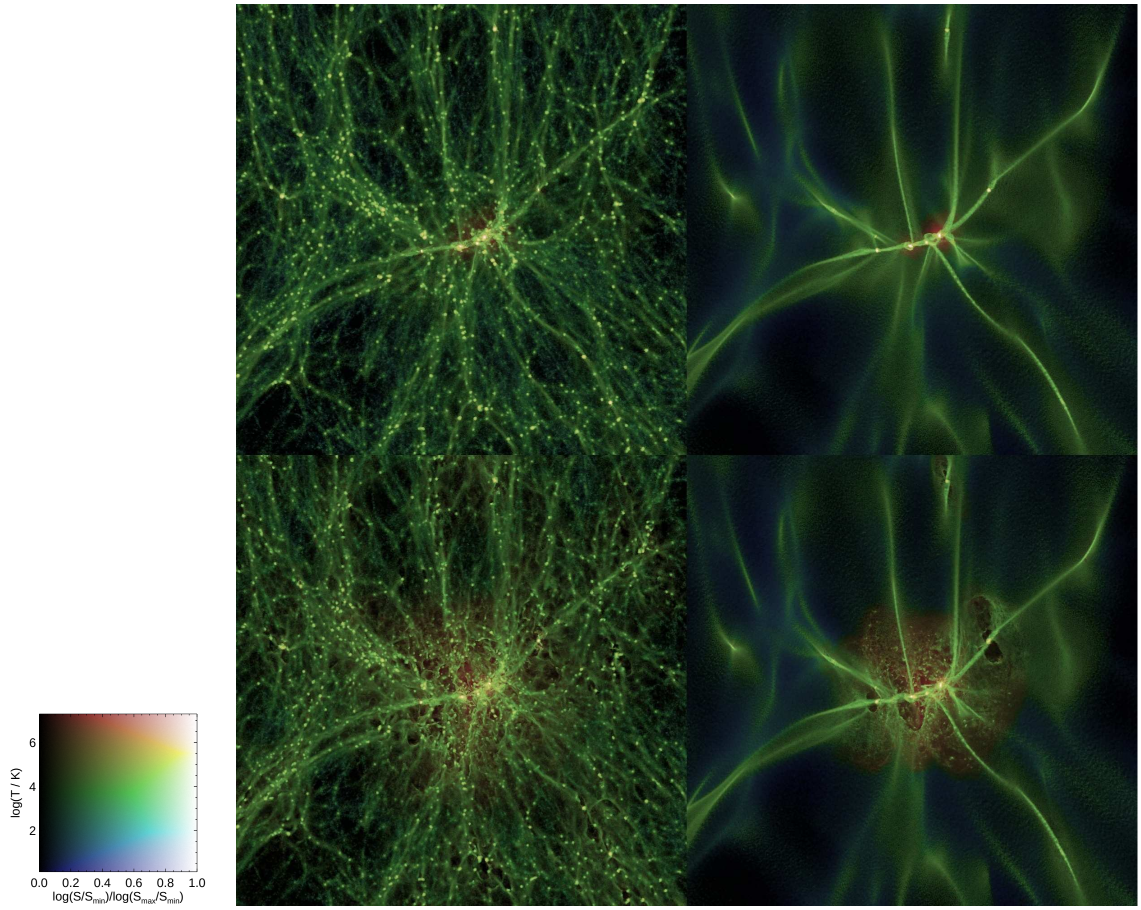

Figure 5.1: Gas temperature maps of the IGM at redshift 6 for the four simulations (*left to right, top to bottom:* CN, WN, CW, WW). Intensity indicates squared gas density projected along the line of sight (S) and hue gas temperature: blue through green to red corresponds to cold through to hot gas on a logarithmic scale as shown inthe two-dimensional colour table. Each panel is 3Mpc (comoving) on each side, and is centred on the centre-of-mass of the high resolution region.

the formation region of a Milky Way-like galaxy.

We now turn to the properties of our simulations at higher redshift. We illustrate qualitatively the differences between the four models in Fig. 5.1, in which we show the gas density and temperature in the formation region of the central galaxy at redshift 6. There is a striking difference between the CDM and WDM models in the distribution of gas: the absence of small structures in WDM vastly decreases the number of small filaments. A more subtle difference is apparent in the temperature. Some patches of IGM in WDM have temperatures below 1000K, indicated by the blue colours, that are

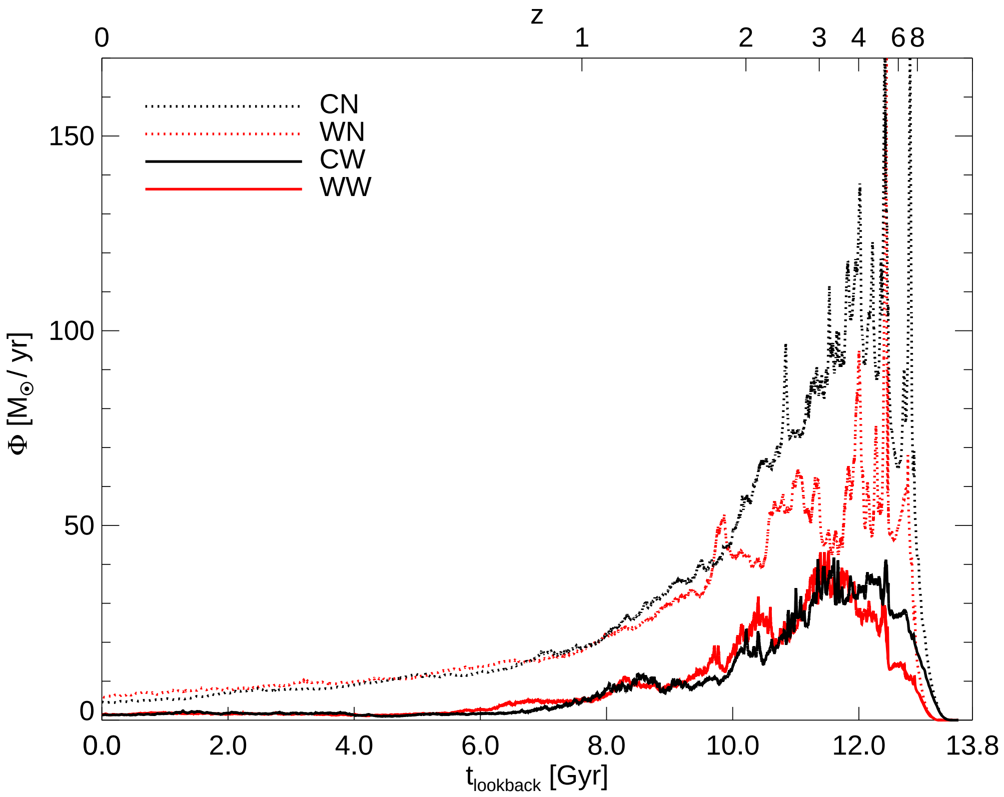

Figure 5.2: Star-Formation rate in the high resolution region as a function of lookback time for the four different models. CDM models are indicated in black and WDM in red; no-winds models in dotted lines and winds models in solid lines. Redshift is indicated along the top x-axis.

absent in CDM. The later formation times allow very cold yet diffuse gas to still exist at these redshifts in WDM where in CDM such gas would have been heated long ago. The introduction of winds has a very noticeable effect, particularly in the WDM models where there is a smaller amount of obscuring filamentary material. Winds blow holes in the IGM and increase its temperature out to larger radii. These properties of the gas will, once fully taken into account, have an impact on the progresss of reionisation in the different models.

5.3 Results

In Fig. 5.2 we show the star-formation rate of each of our models as a function of lookback time. The chief model property that determines star-formation amplitude varies from the dark matter type at very high redshift and SPH model at low redshift, with the crossover occuring at $z = 6$. At this redshift the WW star-formation rate is suppressed by a factor of 3 relative to CW, therefore the number of ionising photons generated in the two models will differ substantially, and thus also the ability of each model to reionise the Universe.

To determine whether it is possible for our proto-galaxy and its satellites to reionise its local volume, we perform the following calculation. For a given simulation snapshot, we determine each star particle to be created at the snapshot *before* it is present in the snapshot data, and thus find its age. We then, by means of the Bruzual & Charlot tables, find the total number of ionising photons emitted by that star particle over its existence. We then take the sum of all photons emitted by all sources, which we denote N_γ, and compare this figure to the number of hydrogen atoms in the box as determined from the total mass in gas particles, $N_{\rm H}$ and the hydrogen fraction. We then determine $z_{\rm re}$ for a given model to be the redshift at which $f_{\rm esc}N_\gamma/N_{\rm H} = 1$, where $f_{\rm esc}$ is the fraction of photons that can escape into the IGM. If $z_{\rm re}$ of the model is lower than the range allowed by the Planck+WP data, we may set limits on $f_{\rm esc}$ or even rule out the model should it require $f_{\rm esc} > 1$.

We show the results in Fig. 5.3. Here we show $\log(\mathrm{N}_\gamma/\mathrm{N}_\mathrm{H})$ in the high-res region as a function of redshift when assigning luminosities to particles using the Salpeter (top) and Chabrier (bottom) IMFs (Salpeter, 1955; Chabrier, 2003). Note that the simulations themselves assume a Salpeter IMF, so the Chabrier-derived calculation is not self-consistent. At redshifts above 10, the winds and no-winds model pairs $\log(\mathrm{N}_\gamma/\mathrm{N}_\mathrm{H})$ differ by less than half a decade, a remarkable result that suggests these findings are insensitive to the application of feedback. The CDM models in all cases attain at least $\log(\mathrm{N}_\gamma/\mathrm{N}_\mathrm{H}) = 1.5$ by $z = 10$, and thus satisfy the Planck+WP constraints for $f_{\rm esc} > 0.03$. The situation for the WDM models is very different. When we apply a Salpeter IMF, both the WN and WW models fail to generate enough ionizing photons even for $f_{\rm esc} = 1$. The Chabrier IMF allows for $f_{\rm esc} > 0.63$, however this value is very much in the upper range of what has been used in the literature (Griffen et al., 2013).

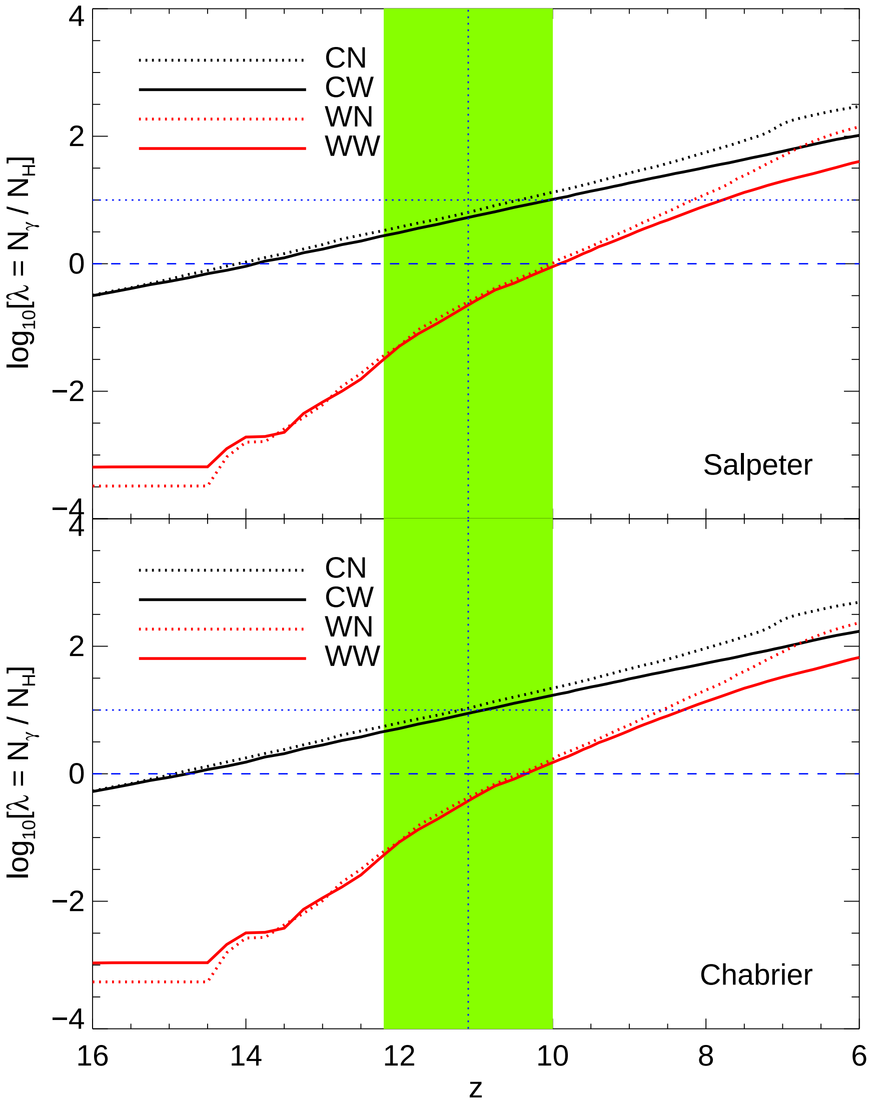

Figure 5.3: The ratio of the cumulative number of Lyman-α photons to gas produced as a function of redshift. CDM models are indicated in black and WDM in red; no-winds models in dotted lines and winds models in solid lines. Redshift is indicated along the top x-axis. The vertical dashed blue line indicates the Planck+WMAP polarisation preferred value of $z_{\rm re} = 11.1$ and the shaded green region the 1σ errors on that measurement (Planck Collaboration et al., 2013a). The horizontal blue dashed line marks the threshold for reionisation if $f_{\rm esc} = 1$ and the dotted line the same quantity for $f_{\rm esc} = 0.1$. The top panel assumes a Salpeter IMF, and the bottom a Chabrier.

5.4 Discussion and conclusions

In this brief Chapter we have utilised a set of hydrodynamical simulations to ascertain the impact of warm dark matter on reionisation, and have found that a WDM model in which $m_{\rm p} = 1.4$keV model is unable to generate enough ionizing photons for an L_* galaxy to reionise its local volume. This technique has the potential to set new limits on the dark matter particle mass $m_{\rm p}$ in conjunction with limits on $f_{\rm esc}$.

This very simple calculation ignores many important effects, however many of these would have the result of requiring that still more photons be produced rather than fewer. Questions remain over the correct way to implement feedback, but any such model would most likely suppress star-formation at high redshift rather than enhance it. Secondly, the simulations we have used were run with the WMAP1 cosmological parameters that feature $\sigma_8 = 0.90$. For Planck+WP this reduces to a best fit value of $\sigma_8 = 0.835$: a smaller value of σ_8 leads to a delay in formation times, thus the WDM model explored here would be in even greater tension with the Planck $z_{\rm re}$ constraints. Our model does not yet account for the presence of recombinations in the IGM, a full implementation of which will also require a model to produce more, rather than fewer, ionizing photons.

Several further effects could instead decrease the tension between our WDM model and the Planck measurement. It has been proposed that the decay into X-rays of sterile neutrino WDM could cool the baryons and so effect the formation of stars earlier in WDM than one would expect. The limited resolution of our simulations may also prevent us from resolving all of the gas sites dense enough to form stars, although the WDM power spectrum cutoff makes this less of a problem for WDM than it is for CDM. One caveat to this point is the possible formation of stars in WDM filaments (Gao and Theuns, 2007), which the star formation equation of state in our model may not be able to take account of.

Perhaps the biggest question left unanswered by this model is whether it is reasonable for an L_* galaxy and its satellites to reionise the local volume on their own, or whether instead they would require an influx of photons from more overdense regions, therefore it is imperative to run these models on cosmological boxes to find the N_γ/N_H ratios in regions of different overdensity.

Once the concerns and complications have been addressed, it will be possible to set limits on the WDM particle mass in a way that is relatively independent of the galaxy formation model. This routine will provide a very useful additional probe to the local Universe measurements detailed in the previous chapters.

Chapter 6

Conclusions

In this thesis we have used simulations of Milky Way-analogue dark matter haloes to test different dark matter models against observations of the Milky Way satellite galaxies and even the CMB measurements of reionisation. In this concluding Chapter we summarise our findings and discuss future prospects for these areas of research.

6.1 Satellite orbits

There is considerable evidence that some of the Milky Way satellite galaxies orbit in a coherent structure (Metz et al., 2008; Pawlowski et al., 2012), and it had been suggested that this configuration is incompatible with the more isotropic distributions found in simulated dark matter haloes. In Chapter 2 we examined the orbits of dark matter subhaloes in the Aquarius simulations and found the distribution of orbital directions was in fact correlated for many substructures. This phenomenon was seen to vary between different central haloes, suggesting that the stochastic nature of halo formation in ΛCDMallows many different configurations of satellite orbits to be realised. We tracked the correlation of orbits back to the simulation initial conditions, and found that the filamentary accretion of matter was responsible for this effect.

6.1.1 Future prospects

Since the work for Chapter 2 was completed in 2011, the PAndAs survey has discovered a large correlation in the orbits of some satellites around M31 (Ibata et al., 2013). As the kinematic data for this and other systems improve, it should be possible to examine further how typical the Milky Way's satellite configuration is, and so whether the variety of satellite system orbits realised in the CDM N-Body simulations such as the Aquarius haloes is replicated in the Universe. Another important step will be the inclusion of baryons in the models, to see if hydrodynamical processes may influence satellite orbits.

6.2 Satellite galaxy structure and abundance in warm dark matter

Early work on satellite galaxies showed they had multiple discrepancies from what N-Body simulations predicted. In the late 1990s it became apparent that the abundance of Milky Way satellite galaxies was much smaller than the number of dark matter subhaloes orbiting $\sim 10^{12}\mathrm{M}_{\odot}$ haloes in CDM simulations (Klypin et al., 1999; Moore et al., 1999), and just over a decade later Boylan-Kolchin et al. (2011, 2012) showed that the central densities of the largest simulated subhaloes were higher than those observed in the Milky Way dSphs, an insight independent of the cusp vs. core debate (Gilmore et al., 2007; Strigari et al., 2010). In Chapters 3 and 4 we examined how the satellite properties would change if the dark matter were not cold but warm. To perform this analysis we developed a technique to identify simulation subhaloes formed by spurious numerical fragmentation: this enabled us to count accurately the number of subhaloes formed around the central halo in each model. We found that, in order for the WDM model to generate enough subhaloes to match the expected number of Milky Way satellies, the dark matter particle thermal-equivalent mass would have to be greater than 1.6keV. The suppression of substructure was found to have an impact on the structure of subhaloes as well as their abundance: the absence of small scale power delays the collapse of structures, thus the centres of subhaloes form at times when the Universe is less dense. These lower central densities are more in keeping with the densities of the satellite galaxies.

6.2.1 Future prospects

WDM as a solution to the 'too big to fail' problem is competitive with other processes that involve baryonic physics (Benson et al., 2002; Pontzen and Governato, 2012; Zolotov et al., 2012) and velocity-dependant self-interacting dark matter (Vogelsberger et al., 2012). The major uncertainty affecting this measurement at present, as shown by Wang et al. (2012), is the Milky Way halo mass: a smaller host halo will decrease the number of subhalos of a given mass, thus the 'too big to fail' problem of CDM is ameliorated and the abundance constraint on WDM becomes more demanding. At present, estimates of the Milky Way halo virial mass vary from $0.5\times10^{12}\mathrm{M}_{\odot}$ to $3\times10^{12}\mathrm{M}_{\odot}$ (see Deason et al., 2012, and references therin), the former prefers CDM and the latter WDM. Once this

Milky Way property has been measured with sufficient accuracy and precision, suites of simulations will be required to measure the stochastic spread in satellite abundances and densities for the likely Milky Way satellites.

6.3 Reionisation

High redshift QSOs have enabled us to analyse the epoch at which the Universe is partially neutral, and the CMB measurements of WMAP and Planck provide a constraint on when free electrons became important after the dark ages. The requirement to effect reionisation by a given redshift is a very powerful extra constraint on any combination of cosmology and galaxy formation models. In the case of WDM, it is possible to rule out particle masses for which the combination of too few galaxies and delayed structure formation makes it impossible to generate enough ionising photons by the required redshift. We showed in Chapter 5 that our chosen Milky Way-analogue halo, now resimulated with a gas hydrodynamics model, was indeed able to produce enough photons to satisfy the Planck constraints if CDM were assumed, but this is not the case for our extreme 1.4keV model WDM, even in the unrealistic case of turning off supernova feedback.

6.3.1 Future prospects

The study carried out here used a single Milky Way-analogue dark matter halo at just one simulation resolution. Both higher and lower resolution simulations will be required to check that our result does not depend on resolution issues. It will also be necessary to examine other haloes of different masses, environments, and formation histories to improve our constraint. Once these and the other important considerations such as cosmological parameters, recombination and other factors have been taken in to account, we will have a very useful probe of dark matter temperature that is independent of the Local Universe measurements. Future studies of the 21-cm atomic hydrogen line with facilities such as SKA will enable us to track the progress of reionisation, and thus the collapse of dark matter structures, to still higher redshifts (Pritchard and Loeb, 2012).

Appendix A

$V_{\rm max}$ *Convergence Study*

A.1 Convergence study

For several dwarf spheroidal satellites of the Milky Way it is possible to measure the circular velocity at the radius encompassing half the light in a relatively model-independent way Walker et al. (2009); Wolf et al. (2010). The smallest measured value is 5.7 $\rm kms^{-1}$ for Leo IV. The circular velocity at the half-light radius is a lower bound on $V_{\rm max}$. Therefore, to compare with Milky Way data, we need the number of subhaloes in the simulations with $V_{\rm max}$ greater than 5.7 $\rm kms^{-1}$. It is important to check that the simulations resolve all these subhaloes.

We have performed a convergence study using the level 4, level 3, and level 2 simulations for two of the WDM models. For the $m_{2.3}$ model, the subhalo $V_{\rm max}$ function at level 4 deviates by 10 per cent from that in the corresponding level 2 simulation at a value of $V_{\rm max} = 11$ $\rm kms^{-1}$; the level 3 subhalo $V_{\rm max}$ function deviates by the same amount at a value of $V_{\rm max} = 6$ $\rm kms^{-1}$. The particle masses in the level 4 and level 3 simulations differ by a factor of 8. If we write $(m_4/m_3)^n$ $=V_{\rm max}$ $(4)/V_{\rm max}$ (3) (where the numbers denote the resolution level) we find $n = 0.29$. The high resolution, level 2, simulation has a particle mass 3.6 times smaller than that of level 3. Therefore we expect this simulation to be complete to 10 per cent at $V_{\rm max} = 4.2$ $\rm kms^{-1}$. A similar analysis for the $m_{1.4}$ simulation shows that this is already complete at level 3 for $V_{\rm max}$ =5.7 $\rm kms^{-1}$.

We have checked the validity of this approach by analysing the original Aquarius Aq-A2 and Aq-A1 simulations. The Aq-A1 simulation has a particle mass of $1.7 \times 10^3 \rm M_\odot$, a factor of ~ 8 smaller than the level 2 simulations. We find that at $V_{\rm max}$ =5.7 $\rm kms^{-1}$ the Aq-A2 subhalo $V_{\rm max}$ function deviates by 8 per cent from the Aq-A1 result. The suppression of small subhaloes in WDM models should result in better subhalo completeness in this case compared to CDM in this mass range (c.f. convergence between levels 3 and 2 for $m_{1.4}$). We therefore conclude that we have lost no more than 8 per cent of the 'true' number of subhaloes in the $m_{2.3}$ simulation and even fewer in the warmer models.

Bibliography

Abazajian, K., Fuller, G. M., and Tucker, W. H.: 2001, ApJ **562**, 593

Alcock, C., Allsman, R. A., Alves, D. R., Axelrod, T. S., Becker, A. C., Bennett, D. P., Cook, K. H., Dalal, N., Drake, A. J., Freeman, K. C., Geha, M., Griest, K., Lehner, M. J., Marshall, S. L., Minniti, D., Nelson, C. A., Peterson, B. A., Popowski, P., Pratt, M. R., Quinn, P. J., Stubbs, C. W., Sutherland, W., Tomaney, A. B., Vandehei, T., and Welch, D.: 2000, ApJ **542**, 281

Allgood, B., Flores, R. A., Primack, J. R., Kravtsov, A. V., Wechsler, R. H., Faltenbacher, A., and Bullock, J. S.: 2006, MNRAS **367**, 1781

Anderhalden, D., Schneider, A., Macciò, A. V., Diemand, J., and Bertone, G.: 2013, JCAP **3**, 14

Angulo, R. E., Hahn, O., and Abel, T.: 2013, *ArXiv e-prints*

Asaka, T. and Shaposhnikov, M.: 2005, *Physics Letters B* **620**, 17

Avila-Reese, V., Colín, P., Valenzuela, O., D'Onghia, E., and Firmani, C.: 2001, ApJ **559**, 516

Bailin, J., Kawata, D., Gibson, B. K., Steinmetz, M., Navarro, J. F., Brook, C. B., Gill, S. P. D., Ibata, R. A., Knebe, A., Lewis, G. F., and Okamoto, T.: 2005, ApJ **627**, L17

Bailin, J. and Steinmetz, M.: 2005, ApJ **627**, 647

Bardeen, J. M., Bond, J. R., Kaiser, N., and Szalay, A. S.: 1986, ApJ **304**, 15

Barkana, R., Haiman, Z., and Ostriker, J. P.: 2001, ApJ **558**, 482

Bell, E. F., Slater, C. T., and Martin, N. F.: 2011, ApJ **742**, L15

Belokurov, V., Walker, M. G., Evans, N. W., Faria, D. C., Gilmore, G., Irwin, M. J., Koposov, S., Mateo, M., Olszewski, E., and Zucker, D. B.: 2008, ApJ **686**, L83

Benson, A. J., Farahi, A., Cole, S., Moustakas, L. A., Jenkins, A., Lovell, M., Kennedy, R., Helly, J., and Frenk, C.: 2013, MNRAS **428**, 1774

Benson, A. J., Frenk, C. S., Lacey, C. G., Baugh, C. M., and Cole, S.: 2002, *MNRAS* **333**, 177

Benson, A. J., Nusser, A., Sugiyama, N., and Lacey, C. G.: 2001, MNRAS **320**, 153

Bett, P., Eke, V., Frenk, C. S., Jenkins, A., Helly, J., and Navarro, J.: 2007, MNRAS **376**, 215

Bett, P., Eke, V., Frenk, C. S., Jenkins, A., and Okamoto, T.: 2010, MNRAS **404**, 1137

Bode, P., Ostriker, J. P., and Turok, N.: 2001, ApJ **556**, 93

Bond, J. R., Cole, S., Efstathiou, G., and Kaiser, N.: 1991, ApJ **379**, 440

Bosma, A.: 1978, *Ph.D. thesis*, PhD Thesis, Groningen Univ., (1978)

Bower, R. G., Benson, A. J., Malbon, R., Helly, J. C., Frenk, C. S., Baugh, C. M., Cole, S., and Lacey, C. G.: 2006, MNRAS **370**, 645

Boyarsky, A., Lesgourgues, J., Ruchayskiy, O., and Viel, M.: 2009a, JCAP **5**, 12

Boyarsky, A., Lesgourgues, J., Ruchayskiy, O., and Viel, M.: 2009b, *Physical Review Letters* **102(20)**, 201304

Boyarsky, A., Ruchayskiy, O., and Shaposhnikov, M.: 2009c, *Annual Review of Nuclear and Particle Science* **59**, 191

Boylan-Kolchin, M., Bullock, J. S., and Kaplinghat, M.: 2011, MNRAS **415**, L40

Boylan-Kolchin, M., Bullock, J. S., and Kaplinghat, M.: 2012, MNRAS **422**, 1203

Boylan-Kolchin, M., Springel, V., White, S. D. M., and Jenkins, A.: 2010, MNRAS **406**, 896

Briel, U. G., Henry, J. P., and Boehringer, H.: 1992, A&A **259**, L31

Brooks, A. M. and Zolotov, A.: 2012, *ArXiv e-prints*

Bruzual, G. and Charlot, S.: 2003, MNRAS **344**, 1000

Bullock, J. S., Kravtsov, A. V., and Weinberg, D. H.: 2000, ApJ **539**, 517

Busha, M. T., Alvarez, M. A., Wechsler, R. H., Abel, T., and Strigari, L. E.: 2010a, ApJ **710**, 408

Busha, M. T., Wechsler, R. H., Behroozi, P. S., Gerke, B. F., Klypin, A. A., and Primack, J. R.: 2010b, *ArXiv e-prints*

Carignan, C., Cote, S., Freeman, K. C., and Quinn, P. J.: 1997, AJ **113**, 1585

Chabrier, G.: 2003, PASP **115**, 763

Clocchiatti, A., Schmidt, B. P., Filippenko, A. V., Challis, P., Coil, A. L., Covarrubias, R., Diercks, A., Garnavich, P., Germany, L., Gilliland, R., Hogan, C., Jha, S., Kirshner, R. P., Leibundgut, B., Leonard, D., Li, W., Matheson, T., Phillips, M. M., Prieto, J. L., Reiss, D., Riess, A. G., Schommer, R., Smith, R. C., Soderberg, A., Spyromilio, J., Stubbs, C., Suntzeff, N. B., Tonry, J. L., and Woudt, P.: 2006, ApJ **642**, 1

Cole, S., Percival, W. J., Peacock, J. A., Norberg, P., Baugh, C. M., Frenk, C. S., Baldry, I., Bland-Hawthorn, J., and and 23 others: 2005, *MNRAS* **362**, 505

Colín, P., Avila-Reese, V., and Valenzuela, O.: 2000, ApJ **542**, 622

Colín, P., Valenzuela, O., and Avila-Reese, V.: 2008, ApJ **673**, 203

Colombi, S., Dodelson, S., and Widrow, L. M.: 1996, ApJ **458**, 1

Cooper, A. P., Cole, S., Frenk, C. S., White, S. D. M., Helly, J., Benson, A. J., De Lucia, G., Helmi, A., Jenkins, A., Navarro, J. F., Springel, V., and Wang, J.: 2010, MNRAS **406**, 744

Davis, M., Efstathiou, G., Frenk, C. S., and White, S. D. M.: 1985, ApJ **292**, 371

de Vega, H. J. and Sanchez, N. G.: 2010, MNRAS **404**, 885

Deason, A. J., Belokurov, V., Evans, N. W., and An, J.: 2012, MNRAS p. L469

Dekel, A. and Silk, J.: 1986, ApJ **303**, 39

di Cintio, A., Knebe, A., Libeskind, N. I., Yepes, G., Gottlöber, S., and Hoffman, Y.: 2011, MNRAS **417**, L74

Diemand, J., Moore, B., and Stadel, J.: 2005, Nature **433**, 389

Dodelson, S. and Widrow, L. M.: 1994, *Physical Review Letters* **72**, 17

Efstathiou, G., Sutherland, W. J., and Maddox, S. J.: 1990, Nature **348**, 705

Einasto, J.: 1965, *Trudy Astrofizicheskogo Instituta Alma-Ata* **5**, 87

Eke, V. R., Navarro, J. F., and Steinmetz, M.: 2001, ApJ **554**, 114

Ellis, J., Hagelin, J. S., Nanopoulos, D. V., Olive, K., and Srednicki, M.: 1984, *Nuclear Physics B* **238**, 453

Font, A. S. and et al.: 2011, MNRAS **417**, 1260

Frenk, C. S. and White, S. D. M.: 2012, *Annalen der Physik* **524**, 507

Gao, L. and Theuns, T.: 2007, *Science* **317**, 1527

Gao, L., White, S. D. M., Jenkins, A., Stoehr, F., and Springel, V.: 2004, MNRAS **355**, 819

Garrison-Kimmel, S., Rocha, M., Boylan-Kolchin, M., Bullock, J., and Lally, J.: 2013, *ArXiv e-prints*

Gilmore, G., Wilkinson, M. I., Wyse, R. F. G., Kleyna, J. T., Koch, A., Evans, N. W., and Grebel, E. K.: 2007, ApJ **663**, 948

Gnedin, O. Y., Brown, W. R., Geller, M. J., and Kenyon, S. J.: 2010, ApJ **720**, L108

Gonzalez-Garcia, M. C. and Maltoni, M.: 2008, Phys. Rep. **460**, 1

Górski, K. M., Hivon, E., Banday, A. J., Wandelt, B. D., Hansen, F. K., Reinecke, M., and Bartelmann, M.: 2005, ApJ **622**, 759

Governato, F., Brook, C., Mayer, L., Brooks, A., Rhee, G., Wadsley, J., Jonsson, P., Willman, B., Stinson, G., Quinn, T., and Madau, P.: 2010, Nature **463**, 203

Griffen, B. F., Drinkwater, M. J., Iliev, I. T., Thomas, P. A., and Mellema, G.: 2013, MNRAS **431**, 3087

Guo, Q., Cole, S., Eke, V., and Frenk, C.: 2011, MNRAS **417**, 370

Guo, Q., White, S., Li, C., and Boylan-Kolchin, M.: 2010, MNRAS **404**, 1111

Guth, A. H.: 1981, Phys. Rev. D **23**, 347

Guy, J., Sullivan, M., Conley, A., Regnault, N., Astier, P., Balland, C., Basa, S., Carlberg, R. G., Fouchez, D., Hardin, D., Hook, I. M., Howell, D. A., Pain, R., Palanque-Delabrouille, N., Perrett, K. M., Pritchet, C. J., Rich, J., Ruhlmann-Kleider, V., Balam, D., Baumont, S., Ellis, R. S., Fabbro, S., Fakhouri, H. K., Fourmanoit, N., González-Gaitán, S., Graham, M. L., Hsiao, E., Kronborg, T., Lidman, C., Mourao, A. M., Perlmutter, S., Ripoche, P., Suzuki, N., and Walker, E. S.: 2010, A&A **523**, A7

Hahn, O., Abel, T., and Kaehler, R.: 2012, *ArXiv e-prints*

Hogan, C. J. and Dalcanton, J. J.: 2000, Phys. Rev. D **62(6)**, 063511

Hoyle, F.: 1951, in *Problems of Cosmical Aerodynamics*, pp 195–+

Hwang, H. S. and Park, C.: 2010, *ArXiv e-prints*

Ibata, R., Martin, N. F., Irwin, M., Chapman, S., Ferguson, A. M. N., Lewis, G. F., and McConnachie, A. W.: 2007, ApJ **671**, 1591

Ibata, R. A., Lewis, G. F., Conn, A. R., Irwin, M. J., McConnachie, A. W., Chapman, S. C., Collins, M. L., Fardal, M., Ferguson, A. M. N., Ibata, N. G., Mackey, A. D., Martin, N. F., Navarro, J., Rich, R. M., Valls-Gabaud, D., and Widrow, L. M.: 2013, Nature **493**, 62

Iliev, I. T., Moore, B., Gottlöber, S., Yepes, G., Hoffman, Y., and Mellema, G.: 2011, MNRAS **413**, 2093

Irwin, M. J., Belokurov, V., Evans, N. W., Ryan-Weber, E. V., de Jong, J. T. A., Koposov, S., Zucker, D. B., Hodgkin, S. T., Gilmore, G., Prema, P., Hebb, L., Begum, A., Fellhauer, M., Hewett, P. C., Kennicutt, Jr., R. C., Wilkinson, M. I., Bramich, D. M., Vidrih, S., Rix, H., Beers, T. C., Barentine, J. C., Brewington, H., Harvanek, M., Krzesinski, J., Long, D., Nitta, A., and Snedden, S. A.: 2007, ApJ **656**, L13

Kaiser, N., Burgett, W., Chambers, K., Denneau, L., Heasley, J., Jedicke, R., Magnier, E., Morgan, J., Onaka, P., and Tonry, J.: 2010, in *Society of Photo-Optical Instrumentation Engineers (SPIE) Conference Series*, Vol. 7733 of *Society of Photo-Optical Instrumentation Engineers (SPIE) Conference Series*

Kamada, A., Yoshida, N., Kohri, K., and Takahashi, T.: 2013, JCAP **3**, 8

Kang, X., Mao, S., Gao, L., and Jing, Y. P.: 2005, A&A **437**, 383

Kauffmann, G., White, S. D. M., and Guiderdoni, B.: 1993, *MNRAS* **264**, 201

Kauffmann, G., White, S. D. M., and Guiderdoni, B.: 1993, MNRAS **264**, 201

Klypin, A., Kravtsov, A. V., Valenzuela, O., and Prada, F.: 1999, ApJ **522**, 82

Knebe, A., Devriendt, J. E. G., Mahmood, A., and Silk, J.: 2002, MNRAS **329**, 813

Kogut, A., Spergel, D. N., Barnes, C., Bennett, C. L., Halpern, M., Hinshaw, G., Jarosik, N., Limon, M., Meyer, S. S., Page, L., Tucker, G. S., Wollack, E., and Wright, E. L.: 2003, ApJS **148**, 161

Komatsu, E., Smith, K. M., Dunkley, J., Bennett, C. L., Gold, B., Hinshaw, G., Jarosik, N., Larson, D., and and 13 others: 2011, ApJS **192**, 18

Koposov, S., Belokurov, V., Evans, N. W., Hewett, P. C., Irwin, M. J., Gilmore, G., Zucker, D. B., Rix, H., Fellhauer, M., Bell, E. F., and Glushkova, E. V.: 2008, ApJ **686**, 279

Koposov, S. E., Yoo, J., Rix, H., Weinberg, D. H., Macciò, A. V., and Escudé, J. M.: 2009, ApJ **696**, 2179

Lares, M., Lambas, D. G., and Domínguez, M. J.: 2011, AJ **142**, 13

Larson, D., Dunkley, J., Hinshaw, G., Komatsu, E., Nolta, M. R., Bennett, C. L., Gold, B., Halpern, M., and and 13 others: 2011, ApJS **192**, 16

Li, Y., De Lucia, G., and Helmi, A.: 2010, MNRAS **401**, 2036

Li, Y. and White, S. D. M.: 2008, MNRAS **384**, 1459

Libeskind, N. I., Cole, S., Frenk, C. S., Okamoto, T., and Jenkins, A.: 2007, MNRAS **374**, 16

Libeskind, N. I., Frenk, C. S., Cole, S., Helly, J. C., Jenkins, A., Navarro, J. F., and Power, C.: 2005, MNRAS **363**, 146

Libeskind, N. I., Frenk, C. S., Cole, S., Jenkins, A., and Helly, J. C.: 2009, MNRAS **399**, 550

Liu, L., Gerke, B. F., Wechsler, R. H., Behroozi, P. S., and Busha, M. T.: 2011, ApJ **733**, 62

Lovell, M. R., Eke, V., Frenk, C. S., Gao, L., Jenkins, A., Theuns, T., Wang, J., White, S. D. M., Boyarsky, A., and Ruchayskiy, O.: 2012, MNRAS **420**, 2318

Lux, H., Read, J. I., and Lake, G.: 2010, *ArXiv e-prints*

Lynden-Bell, D.: 1976, MNRAS **174**, 695

Macciò, A. V., Kang, X., Fontanot, F., Somerville, R. S., Koposov, S., and Monaco, P.: 2010, MNRAS **402**, 1995

Macciò, A. V., Paduroiu, S., Anderhalden, D., Schneider, A., and Moore, B.: 2012, MNRAS p. 3204

Macciò, A. V., Paduroiu, S., Anderhalden, D., Schneider, A., and Moore, B.: 2013, MNRAS **428**, 3715

Madau, P., Diemand, J., and Kuhlen, M.: 2008, ApJ **679**, 1260

Martin, N. F., McConnachie, A. W., Irwin, M., Widrow, L. M., Ferguson, A. M. N., Ibata, R. A., Dubinski, J., Babul, A., Chapman, S., Fardal, M., Lewis, G. F., Navarro, J., and Rich, R. M.: 2009, ApJ **705**, 758

Martin, N. F., Slater, C. T., Schlafly, E. F., Morganson, E., Rix, H.-W., Bell, E. F., Laevens, B. P. M., Bernard, E. J., Ferguson, A. M. N., Finkbeiner, D. P., Burgett, W. S., Chambers, K. C., Hodapp, K. W., Kaiser, N., Kudritzki, R.-P., Magnier, E. A., Morgan, J. S., Price, P. A., Tonry, J. L., and Wainscoat, R. J.: 2013, *ArXiv e-prints*

Mashchenko, S., Wadsley, J., and Couchman, H. M. P.: 2008, *Science* **319**, 174

McMillan, P. J.: 2011, MNRAS **414**, 2446

Metz, M., Kroupa, P., and Jerjen, H.: 2009, MNRAS **394**, 2223

Metz, M., Kroupa, P., and Libeskind, N. I.: 2008, ApJ **680**, 287

Moore, B., Ghigna, S., Governato, F., Lake, G., Quinn, T., Stadel, J., and Tozzi, P.: 1999, ApJ **524**, L19

Muñoz, J. A., Madau, P., Loeb, A., and Diemand, J.: 2009, MNRAS **400**, 1593

Navarro, J. F., Eke, V. R., and Frenk, C. S.: 1996a, MNRAS **283**, L72

Navarro, J. F., Eke, V. R., and Frenk, C. S.: 1996b, MNRAS **283**, L72

Navarro, J. F., Frenk, C. S., and White, S. D. M.: 1996c, ApJ **462**, 563

Navarro, J. F., Frenk, C. S., and White, S. D. M.: 1997, ApJ **490**, 493

Navarro, J. F., Hayashi, E., Power, C., Jenkins, A. R., Frenk, C. S., White, S. D. M., Springel, V., Stadel, J., and Quinn, T. R.: 2004, MNRAS **349**, 1039

Navarro, J. F., Ludlow, A., Springel, V., Wang, J., Vogelsberger, M., White, S. D. M., Jenkins, A., Frenk, C. S., and Helmi, A.: 2010, MNRAS **402**, 21

Okamoto, T., Frenk, C. S., Jenkins, A., and Theuns, T.: 2010, MNRAS **406**, 208

Papastergis, E., Martin, A. M., Giovanelli, R., and Haynes, M. P.: 2011, ApJ **739**, 38

Parry, O. H., Eke, V. R., Frenk, C. S., and Okamoto, T.: 2012, MNRAS **419**, 3304

Pawlowski, M. S., Pflamm-Altenburg, J., and Kroupa, P.: 2012, MNRAS **423**, 1109

Peñarrubia, J., McConnachie, A. W., and Navarro, J. F.: 2008, ApJ **672**, 904

Peebles, P. J. E.: 1982, ApJ **263**, L1

Perlmutter, S., Aldering, G., Goldhaber, G., Knop, R. A., Nugent, P., Castro, P. G., Deustua, S., Fabbro, S., Goobar, A., Groom, D. E., Hook, I. M., Kim, A. G., Kim, M. Y., Lee, J. C., Nunes, N. J., Pain, R., Pennypacker, C. R., Quimby, R., Lidman, C., Ellis, R. S., Irwin, M., McMahon, R. G., Ruiz-Lapuente, P., Walton, N., Schaefer, B., Boyle, B. J., Filippenko, A. V., Matheson, T., Fruchter, A. S., Panagia, N., Newberg, H. J. M., Couch, W. J., and Supernova Cosmology Project: 1999, ApJ **517**, 565

Planck Collaboration, Ade, P. A. R., Aghanim, N., Armitage-Caplan, C., Arnaud, M., Ashdown, M., Atrio-Barandela, F., Aumont, J., Baccigalupi, C., Banday, A. J., and et al.: 2013a, *ArXiv e-prints*

Planck Collaboration, Ade, P. A. R., Aghanim, N., Armitage-Caplan, C., Arnaud, M., Ashdown, M., Atrio-Barandela, F., Aumont, J., Baccigalupi, C., Banday, A. J., and et al.: 2013b, *ArXiv e-prints*

Polisensky, E. and Ricotti, M.: 2011, Phys. Rev. D **83(4)**, 043506

Pontzen, A. and Governato, F.: 2012, MNRAS **421**, 3464

Power, C., Navarro, J. F., Jenkins, A., Frenk, C. S., White, S. D. M., Springel, V., Stadel, J., and Quinn, T.: 2003, MNRAS **338**, 14

Preskill, J., Wise, M. B., and Wilczek, F.: 1983, *Physics Letters B* **120**, 127

Press, W. H. and Schechter, P.: 1974, ApJ **187**, 425

Pritchard, J. R. and Loeb, A.: 2012, *Reports on Progress in Physics* **75(8)**, 086901

Read, J. I. and Gilmore, G.: 2005, MNRAS **356**, 107

Riess, A. G., Filippenko, A. V., Challis, P., Clocchiatti, A., Diercks, A., Garnavich, P. M., Gilliland, R. L., Hogan, C. J., Jha, S., Kirshner, R. P., Leibundgut, B., Phillips, M. M., Reiss, D., Schmidt, B. P., Schommer, R. A., Smith, R. C., Spyromilio, J., Stubbs, C., Suntzeff, N. B., and Tonry, J.: 1998, AJ **116**, 1009

Sakamoto, T. and Hasegawa, T.: 2006, ApJ **653**, L29

Salpeter, E. E.: 1955, ApJ **121**, 161

Saunders, W., Frenk, C., Rowan-Robinson, M., Lawrence, A., and Efstathiou, G.: 1991, Nature **349**, 32

Sawala, T., Frenk, C. S., Crain, R. A., Jenkins, A., Schaye, J., Theuns, T., and Zavala, J.: 2012, *ArXiv e-prints*

Scannapieco, C., Wadepuhl, M., Parry, O. H., Navarro, J. F., Jenkins, A., Springel, V., Teyssier, R., Carlson, E., Couchman, H. M. P., Crain, R. A., Dalla Vecchia, C., Frenk,

C. S., Kobayashi, C., Monaco, P., Murante, G., Okamoto, T., Quinn, T., Schaye, J., Stinson, G. S., Theuns, T., Wadsley, J., White, S. D. M., and Woods, R.: 2012, MNRAS **423**, 1726

Schneider, A., Smith, R. E., Macciò, A. V., and Moore, B.: 2012, MNRAS **424**, 684

Seljak, U., Makarov, A., McDonald, P., and Trac, H.: 2006, *Physical Review Letters* **97(19)**, 191303

Seljak, U. and Zaldarriaga, M.: 1996, ApJ **469**, 437

Shandarin, S., Habib, S., and Heitmann, K.: 2012, Phys. Rev. D **85(8)**, 083005

Shao, S., Gao, L., Theuns, T., and Frenk, C. S.: 2013, MNRAS **430**, 2346

Shaw, L. D., Weller, J., Ostriker, J. P., and Bode, P.: 2006, ApJ **646**, 815

Somerville, R. S.: 2002, ApJ **572**, L23

Spergel, D. N., Verde, L., Peiris, H. V., Komatsu, E., Nolta, M. R., Bennett, C. L., Halpern, M., Hinshaw, G., Jarosik, N., Kogut, A., Limon, M., Meyer, S. S., Page, L., Tucker, G. S., Weiland, J. L., Wollack, E., and Wright, E. L.: 2003, ApJS **148**, 175

Springel, V. and Hernquist, L.: 2003, MNRAS **339**, 289

Springel, V., Wang, J., Vogelsberger, M., Ludlow, A., Jenkins, A., Helmi, A., Navarro, J. F., Frenk, C. S., and White, S. D. M.: 2008a, MNRAS **391**, 1685

Springel, V., White, S. D. M., Frenk, C. S., Navarro, J. F., Jenkins, A., Vogelsberger, M., Wang, J., Ludlow, A., and Helmi, A.: 2008b, Nature **456**, 73

Springel, V., White, S. D. M., Jenkins, A., Frenk, C. S., Yoshida, N., Gao, L., Navarro, J., Thacker, R., Croton, D., Helly, J., Peacock, J. A., Cole, S., Thomas, P., Couchman, H., Evrard, A., Colberg, J., and Pearce, F.: 2005, Nature **435**, 629

Springel, V., White, S. D. M., Tormen, G., and Kauffmann, G.: 2001a, MNRAS **328**, 726

Springel, V., White, S. D. M., Tormen, G., and Kauffmann, G.: 2001b, MNRAS **328**, 726

Stoehr, F., White, S. D. M., Tormen, G., and Springel, V.: 2002, MNRAS **335**, L84

Strigari, L. E., Frenk, C. S., and White, S. D. M.: 2010, MNRAS **408**, 2364

Strigari, L. E., Kaplinghat, M., and Bullock, J. S.: 2007, Phys. Rev. D **75(6)**, 061303

Szalay, A. S. and Marx, G.: 1976, A&A **49**, 437

Tikhonov, A. V., Gottlöber, S., Yepes, G., and Hoffman, Y.: 2009, MNRAS **399**, 1611

Tollerud, E. J., Beaton, R. L., Geha, M. C., Bullock, J. S., Guhathakurta, P., Kalirai, J. S., Majewski, S. R., Kirby, E. N., Gilbert, K. M., Yniguez, B., Patterson, R. J., Ostheimer, J. C., Cooke, J., Dorman, C. E., Choudhury, A., and Cooper, M. C.: 2012, ApJ **752**, 45

Tollerud, E. J., Bullock, J. S., Strigari, L. E., and Willman, B.: 2008, ApJ **688**, 277

Tyson, J. A., Wenk, R. A., and Valdes, F.: 1990, ApJ **349**, L1

Vera-Ciro, C. A., Helmi, A., Starkenburg, E., and Breddels, M. A.: 2012, *ArXiv e-prints*

Viel, M., Becker, G. D., Bolton, J. S., and Haehnelt, M. G.: 2013a, *ArXiv e-prints*

Viel, M., Becker, G. D., Bolton, J. S., and Haehnelt, M. G.: 2013b, *ArXiv e-prints*

Viel, M., Becker, G. D., Bolton, J. S., Haehnelt, M. G., Rauch, M., and Sargent, W. L. W.: 2008, *Physical Review Letters* **100(4)**, 041304

Viel, M., Lesgourgues, J., Haehnelt, M. G., Matarrese, S., and Riotto, A.: 2005, Phys. Rev. D **71(6)**, 063534

Viel, M., Lesgourgues, J., Haehnelt, M. G., Matarrese, S., and Riotto, A.: 2006, *Physical Review Letters* **97(7)**, 071301

Vogelsberger, M., Helmi, A., Springel, V., White, S. D. M., Wang, J., Frenk, C. S., Jenkins, A., Ludlow, A., and Navarro, J. F.: 2009, *MNRAS* **395**, 797

Vogelsberger, M., Zavala, J., and Loeb, A.: 2012, MNRAS p. 3127

Wadepuhl, M. and Springel, V.: 2010, *ArXiv e-prints*

Wadepuhl, M. and Springel, V.: 2011, MNRAS **410**, 1975

Walker, M. G., Mateo, M., Olszewski, E. W., Peñarrubia, J., Wyn Evans, N., and Gilmore, G.: 2009, ApJ **704**, 1274

Walker, M. G., Mateo, M., Olszewski, E. W., Peñarrubia, J., Wyn Evans, N., and Gilmore, G.: 2010, ApJ **710**, 886

Walsh, S. M., Jerjen, H., and Willman, B.: 2007, ApJ **662**, L83

Wang, J., Frenk, C. S., Navarro, J. F., Gao, L., and Sawala, T.: 2012, *ArXiv e-prints*

Wang, J. and White, S. D. M.: 2007, MNRAS **380**, 93

Warnick, K. and Knebe, A.: 2006, MNRAS **369**, 1253

White, S. D. M.: 1984, ApJ **286**, 38

White, S. D. M., Frenk, C. S., and Davis, M.: 1983, ApJ **274**, L1

White, S. D. M., Navarro, J. F., Evrard, A. E., and Frenk, C. S.: 1993, Nature **366**, 429

Willman, B., Blanton, M. R., West, A. A., Dalcanton, J. J., Hogg, D. W., Schneider, D. P., Wherry, N., Yanny, B., and Brinkmann, J.: 2005a, AJ **129**, 2692

Willman, B., Dalcanton, J. J., Martinez-Delgado, D., West, A. A., Blanton, M. R., Hogg, D. W., Barentine, J. C., Brewington, H. J., Harvanek, M., Kleinman, S. J., Krzesinski, J., Long, D., Neilsen, Jr., E. H., Nitta, A., and Snedden, S. A.: 2005b, ApJ **626**, L85

Wolf, J., Martinez, G. D., Bullock, J. S., Kaplinghat, M., Geha, M., Muñoz, R. R., Simon, J. D., and Avedo, F. F.: 2010, MNRAS **406**, 1220

Xue, X. X., Rix, H. W., Zhao, G., Re Fiorentin, P., Naab, T., Steinmetz, M., van den Bosch, F. C., Beers, T. C., Lee, Y. S., Bell, E. F., Rockosi, C., Yanny, B., Newberg, H., Wilhelm, R., Kang, X., Smith, M. C., and Schneider, D. P.: 2008, ApJ **684**, 1143

York, D. G.: 2000, AJ **120**, 1579

Yue, B. and Chen, X.: 2012, ApJ **747**, 127

Zavala, J., Okamoto, T., and Frenk, C. S.: 2008, MNRAS **387**, 364

Zentner, A. R., Kravtsov, A. V., Gnedin, O. Y., and Klypin, A. A.: 2005, ApJ **629**, 219

Zolotov, A., Brooks, A. M., Willman, B., Governato, F., Pontzen, A., Christensen, C., Dekel, A., Quinn, T., Shen, S., and Wadsley, J.: 2012, *ArXiv e-prints*

Zucker, D. B., Belokurov, V., Evans, N. W., Kleyna, J. T., Irwin, M. J., Wilkinson, M. I., Fellhauer, M., Bramich, D. M., Gilmore, G., Newberg, H. J., Yanny, B., Smith, J. A., Hewett, P. C., Bell, E. F., Rix, H., Gnedin, O. Y., Vidrih, S., Wyse, R. F. G., Willman, B., Grebel, E. K., Schneider, D. P., Beers, T. C., Kniazev, A. Y., Barentine, J. C., Brewington, H., Brinkmann, J., Harvanek, M., Kleinman, S. J., Krzesinski, J., Long, D., Nitta, A., and Snedden, S. A.: 2006a, ApJ **650**, L41

Zucker, D. B., Belokurov, V., Evans, N. W., Wilkinson, M. I., Irwin, M. J., Sivarani, T., Hodgkin, S., Bramich, D. M., Irwin, J. M., Gilmore, G., Willman, B., Vidrih, S., Fellhauer, M., Hewett, P. C., Beers, T. C., Bell, E. F., Grebel, E. K., Schneider, D. P., Newberg, H. J., Wyse, R. F. G., Rockosi, C. M., Yanny, B., Lupton, R., Smith, J. A., Barentine, J. C., Brewington, H., Brinkmann, J., Harvanek, M., Kleinman, S. J., Krzesinski, J., Long, D., Nitta, A., and Snedden, S. A.: 2006b, ApJ **643**, L103

Zwicky, F.: 1933, *Helvetica Physica Acta* **6**, 110